

Multimetric Fixel-based Analysis of Tract  
Profiles Using Multi-Tensor Based Diffusion  
MRI Tractometry, With Application to  
Multiple Sclerosis

Erick Hernández Gutiérrez

Thesis Proposal

# Contents

<b>1</b>	<b>Introduction</b>	<b>1</b>
1.1	Diffusion MRI Background . . . . .	1
1.2	Diffusion Tensor Imaging . . . . .	3
1.3	HARDI . . . . .	7
1.4	Local Modeling . . . . .	8
1.4.1	Diffusion Spectrum Imaging . . . . .	10
1.4.2	Q-Ball Imaging . . . . .	10
1.4.3	Spherical Deconvolution Methods . . . . .	11
1.4.4	Multi-Tensor Methods . . . . .	14
1.4.4.1	Diffusion Bases Functions . . . . .	14
1.4.4.2	Multi-Resolution Discrete-Search . . . . .	15
1.4.4.3	DIAMOND . . . . .	17
1.5	Tractography . . . . .	18
1.6	Tractometry . . . . .	21
1.7	Phantoms . . . . .	23
1.7.1	Physical Phantoms . . . . .	23
1.7.2	Digital Phantoms . . . . .	23
1.8	Multiple Sclerosis . . . . .	25
1.9	Motivation . . . . .	26
<b>2</b>	<b>Problem Statement</b>	<b>28</b>
2.1	Objective . . . . .	29
<b>3</b>	<b>Methods</b>	<b>31</b>
3.1	Pipeline . . . . .	31
3.1.1	Preprocessing and Tractography . . . . .	31
3.1.2	Bundle Extraction . . . . .	33
3.1.3	Local Modeling . . . . .	34
3.1.4	Tractometry . . . . .	36
3.2	Data . . . . .	36
3.2.1	Synthetic Dataset . . . . .	36
3.2.2	Myelo Inferno Dataset . . . . .	39

CONTENTS	2
----------	---

<b>4 Results</b>	<b>41</b>
4.1 Previous Results . . . . .	41
4.1.1 Robust Estimation of Fixed-FA on Fiber Crossing . . . . .	41
4.1.2 Tractography from Gaussian Multi-Fascicle ODFs . . . . .	45
4.1.3 Real-Time Rendering of Massive Multi-Tensor Fields Using Modern OpenGL . . . . .	47
4.2 Preliminary Results . . . . .	50
4.2.1 Tractometry Pipeline Experiments . . . . .	50
4.2.1.1 Experiments on Synthetic Phantoms . . . . .	50
4.2.1.2 Experiments on Control In-Vivo Subjects . . . . .	54
4.2.1.3 Expected Results . . . . .	55
4.2.2 Improvements of MRDS . . . . .	57
4.2.2.1 Parallelization of MRDS . . . . .	57
4.2.2.2 Model Selector of MRDS . . . . .	59
4.2.2.3 Expected Results . . . . .	59
<b>5 Research Activities</b>	<b>60</b>
5.1 Expected Schedule . . . . .	60
5.2 Conference Abstracts & Journal Publications . . . . .	60
5.3 Collaborations . . . . .	61
<b>6 Conclusions</b>	<b>62</b>
<b>A Appendix</b>	<b>63</b>
A.1 Spherical Harmonics . . . . .	63
A.2 Proof that Multi-Shell HARDI Acquisitions are Required to Fit Multi-Tensor Models . . . . .	65

# List of Figures

- 1.1 Diagram shows the pulsed gradient SE sequence used for diffusion MR imaging. Two diffusion-encoding gradient ( $G_{diff}$  or also denoted as  $\mathbf{g}$ ) pulses are added to the standard SE MR imaging sequence to introduce a phase shift proportional to molecular displacement along the gradient direction.  $\delta$  = duration of the diffusion-encoding gradient,  $\Delta$  = diffusion time interval,  $G_{phase}$  = phase-encoding gradient,  $G_{read}$  = readout gradient,  $G_{slice}$  = section-selective gradient, RF=radio frequency pulse,  $t$  = acquisition time. The diffusion-encoding gradient often is symbolized by the vector  $\mathbf{q}$ , which is equal to the product of  $\gamma\delta\mathbf{g}$ , where  $\gamma$  is the gyro-magnetic ratio; thus, it represents the effective diffusion gradient. Image taken from [2]. . . . .

1.2 (right) Diffusion-weighted image (DWI) from signal sampling at a single point in (left) 3D q-space. Brain areas where diffusion is intense in the direction of the applied gradient  $\mathbf{q}$  appear darker because of a decrease in the measured signal that results from dephasing. Image taken from [2]. . . . .

1.3 DTI ellipsoids, prolate, oblate, and spherical tensors. Water molecules diffusion along fibers. The diffusion tensor model captures this orientated diffusion process with the diffusion ellipsoid. Here, the FA of the illustrated tensor is approximately 0.7. The tensor can also be oblate if the first two eigenvalues are equal or spherical if all three are equal. Figure taken from [51]. . . . .

1.4 Graphic Illustration of DTI. (a) Example of the obtained diffusion tensor image resulted to fit DTI at every voxel to real human brain dMRI. Tensors are colored with the PDD using the color code  $(x, y, z) \rightarrow (r, g, b)$ . (b) The left image is the FA map obtained from computing the FA value of the diffusion tensor at each voxel of (a). Dark areas represent voxels with low FA while high intensity voxels represent high FA. The right image is the MD map computed from the tensor field showed in (a). Bright areas indicate areas high mean diffusivity. Some studies like [133, 134] has shown that reduction in RD is associated with demyelination of the axons in the brain. . . . .

1.5	Different HARDI schemes for sampling the q-space. (a) Cartesian sampling designed for DSI, see seccion . (b) Single-shell spherical sampling. (c) Multi-shell spherical sampling. . . . .	7
1.6	An example of an overlaid DWI in a coronal slice and a fixel grid. Both voxels and fixels have a position in the regular lattice structure of the image. But fixels position is tied to the white matter anatomy itself while the voxel position is related to spatial domain. Note that there could be more than 1 fixel per voxel. Typically, there is nor more than 3 fixels per voxel [61]. Each fixel orientation is aligned with the orientation of one of the underlying white matter fascicles. Image taken from [60]. . . . .	9
1.7	Illustration of the FRT that QBI uses to reconstruct the dODF using the diffusion MRI measured signal. Image taken from [51]. . . . .	11
1.8	Convolution assumption in q-space between the fiber response function $R$ and the fODF $F$ . Image taken from [51]. . . . .	12
1.9	Spherical deconvolution intuition to improve angular resolution of ODF reconstruction. Assuming a particular response function, the deconvolution will remove the “blurry” part of the diffusion ODF to obtain a sharp fiber ODF that better captures the underlying fiber populations. Hence, a better angular resolution can be obtained, as illustrated in $45^\circ$ and $60^\circ$ crossing in the bottom of the figure. Image taken from [3]. . . . .	13
1.10	2D schema of DBFs. The blue lines correspond to a dictinoary with $J = 5$ basis functions. (a) Continuous-blue line shows the DBFs generated by an uniformly distributed tensor basis with $J = 5$ . The doted-red line represents the normalized diffusion signal $S(\mathbf{q})$ generated by an arbitrary diffusion tensor. In this case, the solution for $\alpha$ is expected to be $\alpha = (0, 0, 1, 0, 0)$ . (b) Schema for two fiber case, the dotted-red lines represent the signals for two arbitrary tensors, which their half-addition of both signals are shown in the cross-marked black line. For this case, the solution is expected to be $\alpha = (0, 0, 0.5, 0, 0.5)$ . Image taken from [13]. . . . .	15
1.11	Quantitative comparison on simulated data. Reconstructions of the ODFs are shown for the Ground Truth (a), CSD (b) and MRDS (c)..	17

- 1.12 (left) Hypothetical multi-compartment model, in which an isotropic (red) and two anisotropic (blue and green) compartments are mixed. For illustration purpose we represent here a 2D multi-compartment model. (middle) Under the hypothesis of purely homogeneous compartments with no exchange, a multi-tensor model is typically used to describe the signal arising from the multi-compartments. The corresponding probability density of diffusivities is composed of a mixture of delta functions. (right) DIAMOND captures the multidimensional diffusivity and heterogeneity of each compartment using peak-shaped distributions of multidimensional diffusivities. The expectation of each matrix-variate distribution captures the compartment overall diffusivity while the distribution concentration captures its microstructural heterogeneity. Specifically, a distribution with a broad peak indicates a highly heterogeneous compartment.  
Imagen taken from [15]. . . . . 18
- 1.13 Graphic illustration of tractography. (a) Example of fODFs that can be followed to reconstruct (b) an individual streamline computed after performing tractography. (c) An example whole-brain tractogram that consists of streamlines covering the entire white matter.  
Image taken from [65]. . . . . 19
- 1.14 Illustration of the main diffusion directions (black arrows) forming a vector field. (a) A streamline  $s = \{p_i\}_{i=1}^8$  (red arrow) is shown following the vector field. It can be seen how the streamline is composed of points in the space (red points). (b) A tractogram  $\mathcal{T} = \{s_i\}_{i=1}^5$  consisting of 5 different streamlines obtained by pursuing the maximum diffusivity direction. (c) Illustration of how the diffusion tensor can be used to represent the dominant diffusion direction. 20
- 1.15 Example of the steps performed in the Gibbs tracking technique to simultaneously fit a whole tractogram to the dMRI data. Image taken from [106]. . . . . 21
- 1.16 Illustration of how the dMRI metrics and the tracks are combined using tractometry to get the tract profile. (left) FA map. (middle) tracks along the bundle. (right) tract profile obtained from the tractometry. Rainbow colors mark the locations along the streamlines. Tract profiles can be plotted using the values along the streamlines (20 locations for this example). . . . . 21
- 1.17 Important steps of the tractometry\_flow pipeline illustrated on the corticospinal tract (CST) using the FA metric. (a) Outliers are removed. (b) Centroids are extracted. (c) The bundle is subsampled.  
Image taken from [128]. . . . . 22
- 1.18 Example of physical phantoms used for tractography validation. . . . . 23

- 1.19 Illustration of the Phantomas phantom used for 2nd HARDI Reconstruction Challenge5, organized at ISBI 2013. It consists of 27 fiber bundles, on a  $70 \times 70 \times 70$  grid, with 3 spherical CSF regions abstractly mimicking a human brain. Image taken from [38]. . . . . 24
- 1.20 Illustration the 71 tracts used for the 99 brains Fiberfox simulation (a), exemplary axial slices of one simulated subject of the 99 brains dataset with various artifacts (b), and an exemplary phantom with randomized bundle configuration generated using Fiberfox (c). Image taken from [38]. . . . . 24
- 1.21 Different imaging features in MS. (A, B) Axial fluid-attenuated inversion recovery (FLAIR) shows typical appearance of deep WM plaques like multiple hyperintense lesions in subcortical and cerebral deep WM, mostly ovoid in shape. (C, D) Sagittal FLAIR shows demyelinating plaques along the margin of lateral ventricles and the corpus callosum, with the typical radial arrangement, called Dawson fingers. Axial T1-weighted images before (E) and after (F) gadolinium administration show a single plaque in the right frontal lobe, which shows enhancement after contrast injection, consistent acute inflammatory demyelination. (G) Diffusion-weighted imaging reveals a high signal lesion, which may be related to the acute phase of the disease. Images taken from <https://radiologykey.com/diffusion-magnetic-resonance-imaging-in-multiple-sclerosis>. 26
- 1.22 Limitations of DTI and potential of advanced diffusion MRI modeling for improved brain connectivity mapping and track-specific white matter tissue assessment. . . . . 27
- 3.1 Processes of the TractoFlow pipeline with the additional Rician bias correction process. The input files (blue square) required to run the pipeline. They can be either in BIDS format or separated files. The DWI processes (green square) that take the DWI, the b-values/b-vectors files and the reversed phase encoded  $b = 0$  image. The T1 processes (red square) that take the T1 weighted image in input. The fiber tracking process (light blue) and all processes or images that are optional (orange diamond). . . . . 33
- 3.2 Illustration of a whole brain tractogram obtained with tractography and separated into the principal bundles with ReconBundlesX. Some of the obtained bundles are shown. For example, the frontal aslant tract (FAT), frontopontine (FPT), corpus callosum frontal (CC\_fr), pyramidal tract (PYT), inferior fronto-occipital fascicle (IFOF), superior longitudinal fasciculus (SLF), superior cerebellar peduncle (SCP), cingulum (CG), middle cerebellar peduncle (MCP), optic radiation (OR), inferior longitudinal fasciculus (ILF) and parieto-occipital pontine (POPT). . . . . 34

3.3	Axial view of a tensor image and a multi-tensor image fitted with DTI and MRDS, respectively. Comparison between the DTI and MRDS methods illustrate the capability of MRDS to recover different fiber crossing regions. This also illustrate how, in some voxels, MRDS is overfitting the number of tensors. . . . .	35
3.4	Processes of the proposed pipeline. Input DWI, bval/bvec and T1 files (blue square). The tractoflow preprocessing and tractography step (light blue square). The Resampled DWI from tractoflow is used as input for the local modeling step (violet square) with MRDS. On the other hand, the RecoBundlesX step (yellow square) takes the output tractogram from tractoflow and splits it into separated bundles. Finally, the fixel-based metrics from MRDS and the separated bundles from ReconBundlesX are combined using tractometry_flow to compute the tract profile for every metric and bundle combination (pink square). . . . .	36
3.5	The structured field of the digital phantom showing the 3 fiber bundles configuration. The directions of the fiber populations are colred depending on their orientation using the color code $(x, y, z) \rightarrow (r, g, b)$ . . . . .	37
3.6	Histogram of lambda values estimated by fitting the DTI implementation included in MRtrix [58] to the myelo_inferno dataset. Here $\lambda^{\parallel} = \lambda_1$ and $\lambda^{\perp} = \lambda_{2,3} = (\lambda_2 + \lambda_3) / 2$ . . . . .	38
3.7	From phantom structure and Gaussian mixture to diffusion-Weighted signal with noise. . . . .	38
3.8	(a) Nifti image with control values (white) for the diffusivities of the Bundle 1. Values are constant along the bundle. (b) Nifti image for Bundle 1 with damage (yellow) values. . . . .	39
4.1	Proposed pipeline to estimate fixel-FA for each bundle. . . . .	41
4.2	(up) Segmentation obtained after the segmentation stage of the pipeline. Each recovered fiber bundle is colored with a different color to identify each bundle. The color of each fiber bundle is consistent with the colors shown in all the other figures. (down) Ground-truth fiber bundles. . . . .	43
4.3	FA values along each bundle results (a) for synthetic data and (b) for the centrum semiovale in the in-vivo data. Each row represents the FA values for a different bundle. Each column represents, respectively, FA values in voxels with 1, 2 and 3 tensors (i.e., FA values in each bundle are shown separated depending on the number of tensors per voxel). For comparison, the ground-truth FA value for each bundle was added as a black horizontal line. . . . .	44
4.4	Proposed pipeline for the DiSCo challenge. . . . .	45

4.5	Visualization of the GT and reconstructed dODFs of the training dataset of the DiSCo challenge. $N_{max}$ represents the maximum number of pixels in each voxel, which is determined by the selector model BIC [11]. Both CSD and MRDS are able to recover most of the orientations. However, MRDS can recover orientations presented in the GT that are not recovered by CSD as it is highlighted with a dashed orange square. . . . .	46
4.6	Visual comparison of the streamlines connecting 2 ROIs (grey colored). The leftmost tractogram represents the GT strands trajectories (white colored). The one in the middle is the overlapped GT and CSD tractograms. The rightmost represents the overlapped GT and MRDS tractograms. This experiment shows the higher account of false positive connections in the MRDS tractogram as well as the better overlapping with the GT. . . . .	47
4.7	Multi-tensor field fitted to the synthetic phantom [25, 26] is showed in different coloring modes. (a) Single tensor glyphs colored using the PDD of the tensor similar to the MRtrix viewer. (b) Same as (a) but using multi-tensor glyphs. (c,d,e) Multi-tensor glyphs colored using the AD, RD, and FA values of the tensor with the Viridis, Plasma and Cool Smooth Warm color maps, respectively. . . . .	48
4.8	The multi-tensor field fitted to a control healthy subject of the myelo_inferno dataset. (a) 3D render of the multi-tensor field colored by the PDD. (b) The viewer is interactive, so it allows rotating, translating, zooming in and out. . . . .	49
4.9	In addition to 3D slide rendering, it is shown how the viewer is able to render slides in 2D mode for Sagittal, Axial and Coronal views. (a) Axial view of the 3D render illustrated in Fig. 2. (b) Zoom-in of the slide to easily explore details. . . . .	49
4.10	Pipeline adapted from 4.1 to process the phantom and validate the pipeline in Figure 3.4. . . . .	50
4.11	Tract profiles obtained from the control phantom applying the tractometry pipeline of Figure 4.10, which combines the GT bundles with the pixel-based metrics estimated by MRDS. Each row represents the tract profiles of each pixel-based metric (pixel-RD, pixel-AD, pixel-FA and pixel-MD). Each column represents the tract profiles for a different bundle. Note that the location 1 and location 13 of the bundle 3 are the same as the bundle is a circle. . . . .	52

- 4.12 Tract profiles obtained with the tractometry pipeline of Figure 4.10, which combines the GT bundles with the fixel-based metrics estimated by MRDS. Each row represents the tract profiles of each fixel-based metric (fixel-RD, fixel-AD, fixel-FA and fixel-MD). Each column represents the tract profiles for a different bundle. The simulated damaged in bundle 2 is highlighted in yellow. Note that the location 1 and location 13 of the bundle 3 are the same as the bundle is a circle. . . . . 53
- 4.13 Comparison of the different tracts selected to test the pipeline. The DWI was added as anatomical reference of for the tracts. All tracts are composed of two left and right sub-tracts; except for the CC\_fr, which is composed of CC\_fr\_1 and CC\_fr\_2. In (a,c,d,e) the sub-tracts are not visible to keep a good view of the general tract, in (b) it is possible to see the two parts of the tract. . . . . 54
- 4.14 Tract RD profiles for 24 subjects of the myelo\_inferno dataset in 5 tracts. In the first two columns, images show the tract fixel-RD profile obtained from the estimated fixel-RD of MRDS, while in the third and fourth columns images show the tract RD profile obtained with typical the RD metric of DTI. . . . . 56
- 4.15 Tract FA profiles for 24 subjects of the myelo\_inferno dataset in 5 tracts. In the first two columns, images show the tract fixel-FA profile obtained from the estimated fixel-FA of MRDS, while in the third and fourth columns images show the tract FA profile obtained with typical the FA metric of DTI. . . . . 57
- 4.16 Illustration of how the threads are structured in a Nvidia GPU. CUDA threads are grouped in CUDA blocks that are executed in parallel. A CUDA block finishes its computation when all threads belonging to that same CUDA block finish every instruction. . . . . 59

# Chapter 1

## Introduction

### 1.1 Diffusion MRI Background

During the last years, Magnetic Resonance Imaging (MRI) has established itself in clinical imaging and research because it is capable of imaging different physical properties of living tissue in a non-invasive and non-ionizing way. There is a modality of MRI called diffusion-weighted MRI (DW-MRI), or also called diffusion MRI (dMRI), that exploits the natural motion of water molecules undergoing Brownian motion in living biological tissues. Applied to human brain, it allows to infer the microscopic structure of the brain.

Back in time, in [1] was proposed the first a pulsed gradient spin-echo (SE) sequence. To study the displacement of the water molecules inside the brain, diffusion have to be linked to the signal intensity measured in MRI. Thus, two additional diffusion gradient pulses were added to the original SE sequence. The first of the two gradient pulses in this sequence introduces a phase shift that is dependent on the strength of the gradient at the position of the spin at  $t = 0$ . After that a  $180^\circ$  RF pulse is applied to reverse the phase shift induced by the first gradient pulse. Ultimately, a second gradient pulse is applied to induce a phase shift dependent on the spin position at  $t = \Delta$ . The first diffusion-encoding gradient causes the phase shift to vary with position. After the second diffusion-encoding gradient is applied, all spins that did not move will return to their initial state. Therefore, if we measure the signal after the second gradient, we will get a high intensity signal because spins are “in-phase”, resulting in a bright pixel. On the other hand, if the spins have moved, they will subjected to a different field strength during the second pulse and therefore will not return to the initial state, causing a decreased intensity of the measured signal. The longer the displacement along a gradient direction, the lower the signal intensity.

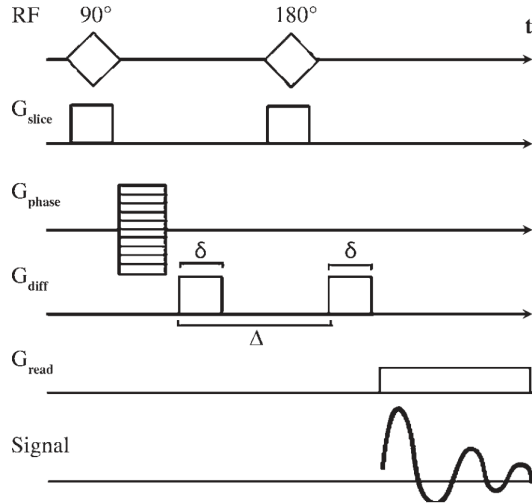


**Figure 1.1:** Diagram shows the pulsed gradient SE sequence used for diffusion MR imaging. Two diffusion-encoding gradient ( $G_{diff}$  or also denoted as  $\mathbf{g}$ ) pulses are added to the standard SE MR imaging sequence to introduce a phase shift proportional to molecular displacement along the gradient direction.  $\delta$  = duration of the diffusion-encoding gradient,  $\Delta$  = diffusion time interval,  $G_{phase}$  = phase-encoding gradient,  $G_{read}$  = readout gradient,  $G_{slice}$  = section-selective gradient, RF=radio frequency pulse,  $t$  = acquisition time. The diffusion-encoding gradient often is symbolized by the vector  $\mathbf{q}$ , which is equal to the product of  $\gamma\delta\mathbf{g}$ , where  $\gamma$  is the gyro-magnetic ratio; thus, it represents the effective diffusion gradient. Image take from [2].

It is possible to represent a diffusion gradient, or also called Diffusion Encoding Orientation (DEO),  $\mathbf{g}$  as a 3D vector  $\mathbf{q} = \gamma\delta\mathbf{g}/2\pi$  whose orientation is in the direction of diffusion and its length is proportional to the gradient strength. The vector  $\mathbf{q}$  allows to navigate in the 3D diffusion space called **q-space** and denoted as  $\mathbb{Q}^3$ , which the coordinates are defined by the frequency wave vector  $\mathbf{q}$  with norm  $q = \|\mathbf{q}\|$  in  $mm^{-1}$ . The gradient strength, also called diffusion weighting, is usually expressed in term of the **b-value**, which is responsible of tuning the diffusion attenuation. It is commonly denoted with  $b$ , given by  $b = t \|\mathbf{q}\|^2$  (proportional to the gradient strength and the diffusion time interval) and measured in  $s/mm^2$ . Hence, the measured diffusion signal  $S$  can be expressed in terms of  $\mathbf{q}$  and  $t$ , or in terms of  $\mathbf{g}$  and  $b$ . The application of a single pulsed gradient SE sequence as described in Figure 1.1 produces one diffusion weighted signal  $S$  that corresponds to one position in q-space, see Figure 1.2. Applying sequences by varying the strength and direction of  $\mathbf{q}$  allows data sampling of the q-space. In most cases, a reference image  $S_0$  is taken. This  $S_0$  image does not have any diffusion sensitization, i.e. the strength of the diffusion gradient is zero ( $q = 0$  and  $b = 0$ ). In other words,  $S_0$  is a standard SE image.

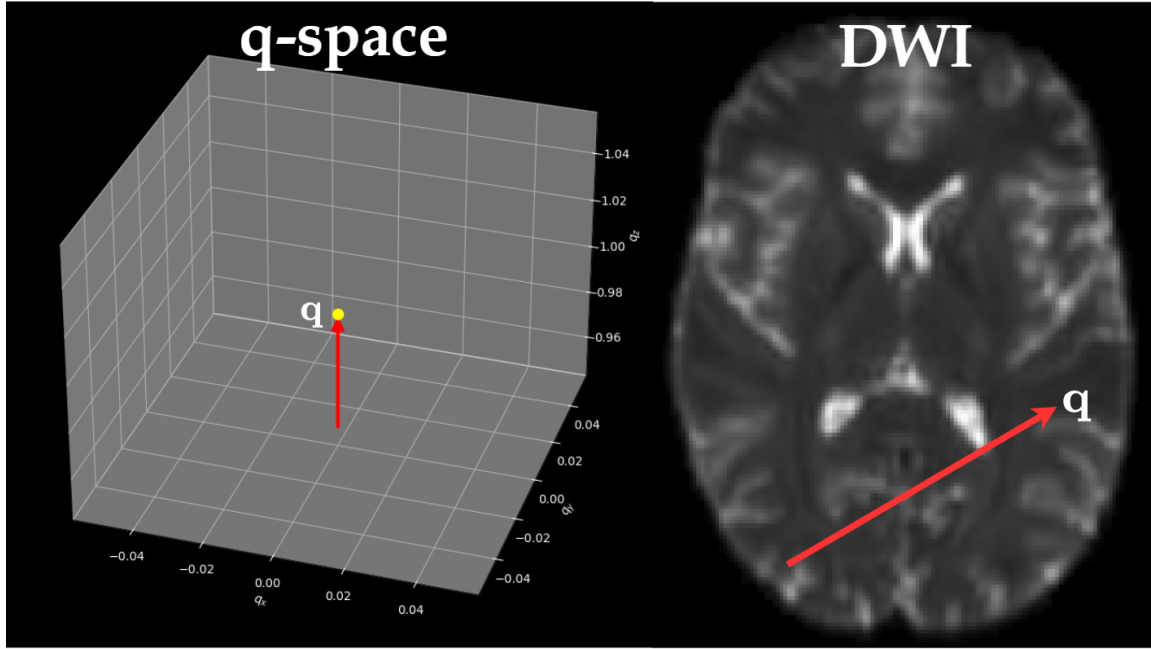


**Figure 1.2:** (right) Diffusion-weighted image (DWI) from signal sampling at a single point in (left) 3D q-space. Brain areas where diffusion is intense in the direction of the applied gradient  $\mathbf{q}$  appear darker because of a decrease in the measured signal that results from dephasing. Image taken from [2].

Finally and in general, the signal  $S$  is normalized by using the  $S_0$  signal to get the signal attenuation  $E(\mathbf{q}, t) = S(\mathbf{q}, t) / S_0$ . It was shown that there is a Fourier relationship between the signal attenuation  $E$  and the diffusion propagator  $p(\mathbf{r}, t)$ , which gives the probability of any displacement  $\mathbf{r}$  during the diffusion time  $t$  such that:

$$E(\mathbf{q}, t) = \int_{\mathbb{R}^3} p(\mathbf{r}, t) \exp(-2\pi i \mathbf{q}^T \mathbf{r}) d\mathbf{r} \quad (1.1)$$

## 1.2 Diffusion Tensor Imaging

The principal direction of diffusion in the tissue can be represented with a method called **Diffusion Tensor Imaging** (DTI). It was rigorously formalized for the first time in [19, 20, 21], which were pioneer works in the field. Assuming Gaussian diffusion, DTI builds the apparent water self-diffusion tensor at each voxel. The structure of the tensor allows to infer the orientation of the diffusion compartments within the voxel. For example, the major eigenvector of the tensor is parallel to the principal fiber orientation, see Figure 1.3.

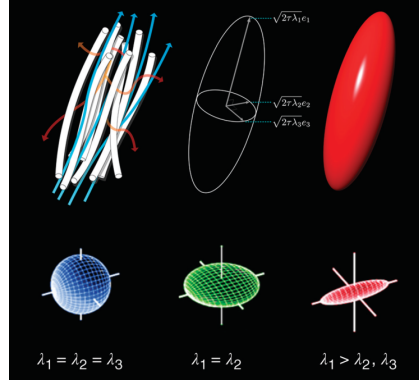


**Figure 1.3:** DTI ellipsoids, prolate, oblate, and spherical tensors. Water molecules diffusion along fibers. The diffusion tensor model captures this orientated diffusion process with the diffusion ellipsoid. Here, the FA of the illustrated tensor is approximately 0.7. The tensor can also be oblate if the first two eigenvalues are equal or spherical if all three are equal. Figure taken from [51].

Considering we sample the q-space using  $n$  DEOs  $\{\mathbf{g}_i\}_{i=1}^n$ . The diffusion signal from a single Gaussian diffusion compartment within a voxel is given by

$$E(\mathbf{g}_i, b) = \exp(-b\mathbf{g}_i^T \mathbf{D}\mathbf{g}_i), \quad 1 \leq i \leq n, \quad (1.2)$$

where  $E_i$  is the normalized diffusion signal magnitude for the DEO  $g_i$ , and  $\mathbf{D}$  is the apparent diffusion tensor mathematically written as a  $3 \times 3$  symmetric and positive definite matrix

$$\mathbf{D} = \begin{pmatrix} D_{xx} & D_{xy} & D_{xz} \\ D_{xy} & D_{yy} & D_{yz} \\ D_{xz} & D_{yz} & D_{zz} \end{pmatrix}.$$

The diffusion tensor can be decomposed into its eigenvectors  $\mathbf{e}_1$ ,  $\mathbf{e}_2$  and  $\mathbf{e}_3$  and eigenvalues  $\lambda_1$ ,  $\lambda_2$  and  $\lambda_3$  using traditional matrix diagonalization methods or they can be obtained directly from the tensor values as it was documented in [22, 23, 24]. The largest eigenvector  $\mathbf{e}_1$  gives the Principal Diffusion Direction (PDD) of the tensor. The rest of the eigenvectors determine the orthogonal planes to it, see Figure 1.3. These eigenvectors and eigenvalues not only determine the shape of the tensor, but they are closely related to brain tissue properties. For example, the largest eigenvalue  $\lambda_1$  is equal to the Axial Diffusivity (AD), while  $\frac{\lambda_2 + \lambda_3}{2}$  give information about the Radial Diffusivity (RD). Besides, from the diffusion tensor eigenvalues, several spherical measures can be extracted such as the Mean Diffusivity (MD) or the Fractional Anisotropy (FA), among others. Both are given by

$$MD = \frac{\lambda_1 + \lambda_2 + \lambda_3}{3}, \quad FA = \frac{3}{2} \sqrt{\frac{(\lambda_1 - \lambda_2)^2 + (\lambda_1 - \lambda_3)^2 + (\lambda_2 - \lambda_3)^2}{\lambda_1^2 + \lambda_2^2 + \lambda_3^2}}.$$

Regardless of these measures have been widely used in publications within the field, it is important to note that the Gaussian diffusion assumption implies that there can only be a single fascicle per voxel. Thus, metrics maps resulting from DTI have one single value per voxel. An extension of these metrics to handle multiple fascicles will be discussed later in Chapter 2, and they constitute an essential component of this work.

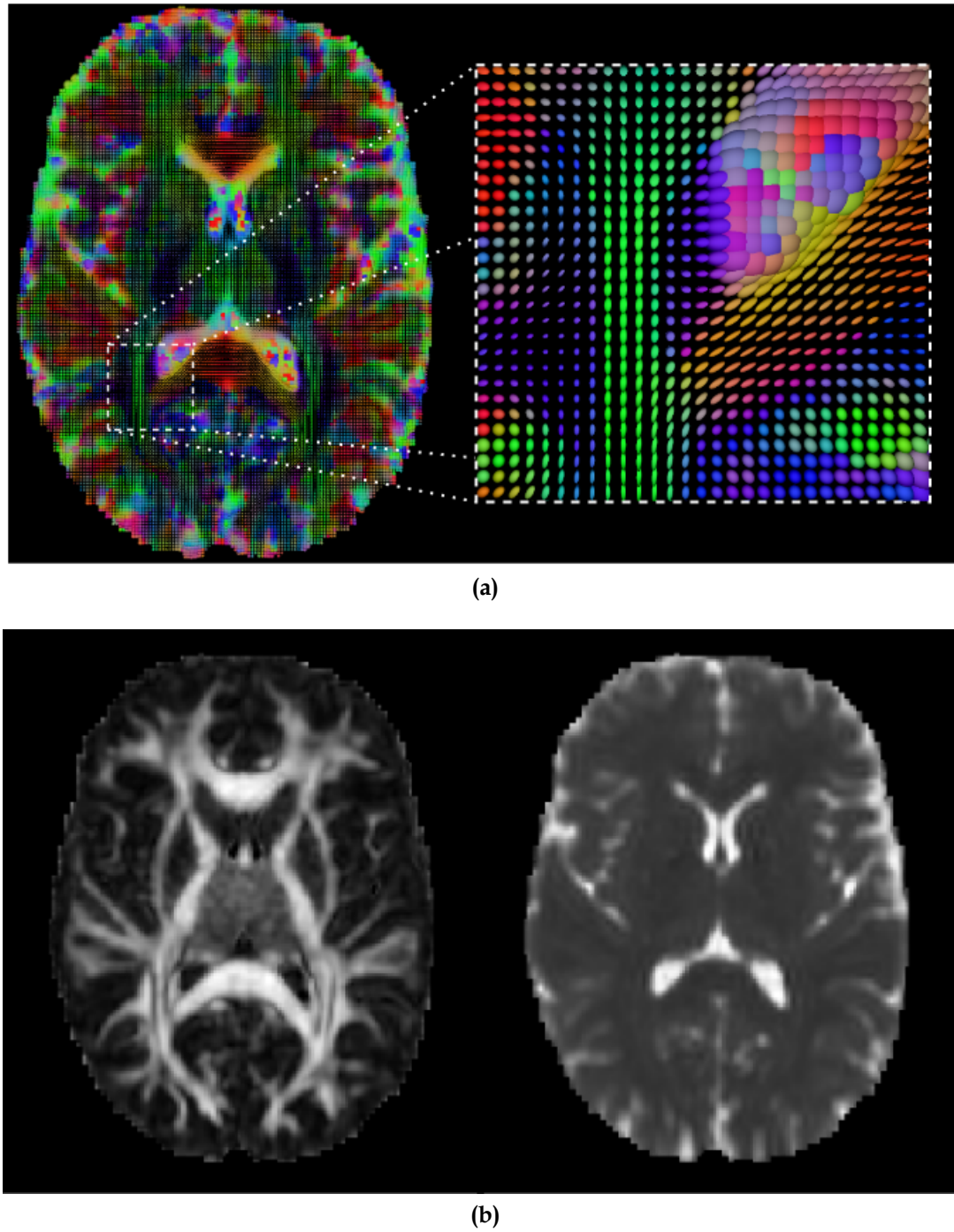


**Figure 1.4:** Graphic Illustration of DTI. (a) Example of the obtained diffusion tensor image resulted to fit DTI at every voxel to real human brain dMRI. Tensors are colored with the PDD using the color code  $(x, y, z) \rightarrow (r, g, b)$ . (b) The left image is the FA map obtained from computing the FA value of the diffusion tensor at each voxel of (a). Dark areas represent voxels with low FA while high intensity voxels represent high FA. The right image is the MD map computed from the tensor field showed in (a). Bright areas indicate areas high mean diffusivity. Some studies like [133, 134] has shown that reduction in RD is associated with demyelination of the axons in the brain.

## 1.3 HARDI

In [51] was used a strategy for dense sampling on the sphere using a single b-value. The term **High Angular Resolution Imaging** (HARDI) was coined for this particular sampling strategy. HARDI is very similar in nature to the standard sampling for DTI. However, HARDI involves a larger number of unique diffusion-weighting gradient directions. Moreover, HARDI is not always a spherical sampling, but there also exists more sampling schemes of the 3D diffusion space, see Figure . For example,

- Cartesian HARDI: Sampling of the whole q-space on a dense 3D cartesian grid. This is usually associated with the DSI method, see Section .
- Single-shell HARDI: This sampling is a spherical sampling of the q-space for a single b-value.
- Multi-shell HARDI: Same as single-shell but using multiple different b-values.

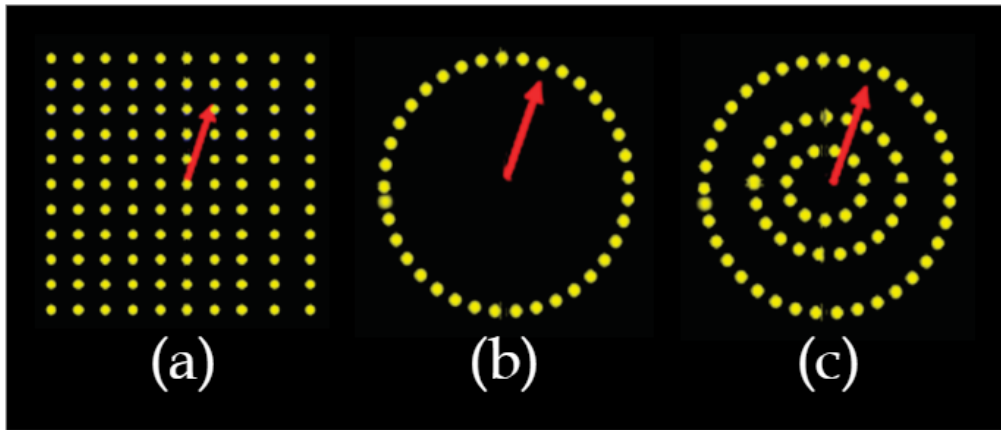


**Figure 1.5:** Different HARDI schemes for sampling the q-space. (a) Cartesian sampling designed for DSI, see seccion . (b) Single-shell spherical sampling. (c) Multi-shell spherical sampling.

HARDI was originally proposed to address the limitation of DTI for solving crossing fiber configurations. It is frequently accompanied of reconstruction methods more sophisticated than DTI, see Section . In fact, some methods require a specially designed HARDI acquisition strategy [4]. Overall, it may be said that HARDI is not only important for solving the crossing fiber problem, but also for improving tractography, providing anisotropy metrics beyond FA and, therefore, for obtaining a reliable tractometry analysis as we will describe in the incoming sections.

## 1.4 Local Modeling

Limitations of DTI came when several fiber populations are present in a voxel. In this section we will discuss HARDI-based some methods presented in the literature that were developed for addressing the limitations of DTI.

The term fixel refers to a specific fibre bundle within a specific voxel. It was proposed by the MRtrix technical team [59]. It is consistent with the definition of pixel and voxel, which are terms commonly used in the field. The terms pixel and voxel are abbreviations of “picture element” and “volume element”; the smallest element within a 2D and 3D image, respectively. On the other hand, fixel refers to “fibre bundle element”: the smallest discrete component of a fibre bundle. Each fixel is completely determinated by the voxel in which it resides, the estimated mean orientation of the underlying fibres attributed to that bundle, a fibre density (or partial volume fraction), and other metrics. Voxels contain image data related to a specific spatial domain, but they can contain information from different types of tissues. Unlike voxels, the position and orientation of a fixel are not related to spatial domain, but they are directly tied to white matter anatomy, see Figure 1.6.

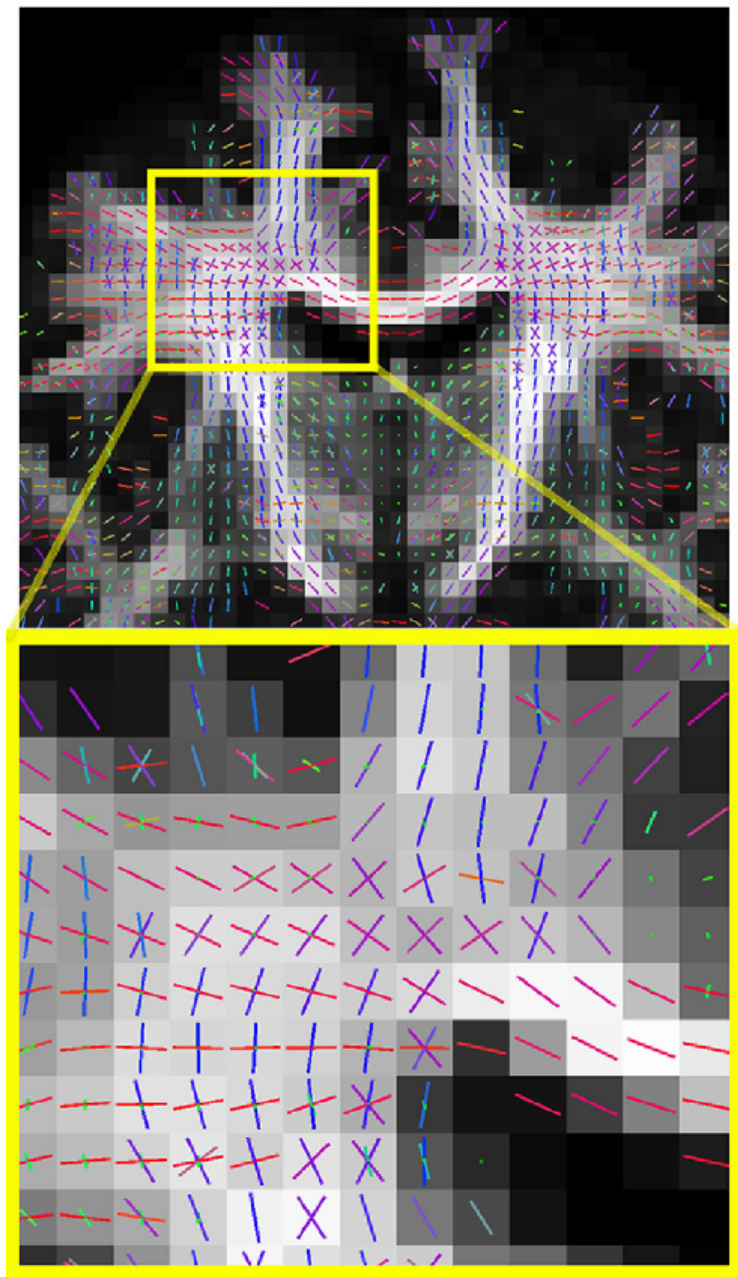


**Figure 1.6:** An example of an overlaid DWI in a coronal slice and a fixel grid. Both voxels and fixels have a position in the regular lattice structure of the image. But fixels position is tied to the white matter anatomy itself while the voxel position is related to spatial domain. Note that there could be more than 1 fixel per voxel. Typically, there is nor more than 3 fixels per voxel [61]. Each fixel orientation is aligned with the orientation of one of the underlying white matter fascicles. Image taken from [60].

Any diffusion model or representation that is capable of fitting multiple anisotropic elements to each image voxel is estimating fixels. It is important to say that fixel

term should not be confused with other interpretations like, for example, “fibre bundle” or “fascicle”.

### 1.4.1 Diffusion Spectrum Imaging

Diffusion Spectrum Imaging (DSI) [18] is a MRI technique that employs the diffusion propagator  $p$  to describe the diffusion process in each voxel. It uses Fourier relationship between a, sufficient dense, cartesian sample of the signal  $S$  in the q-space and the diffusion probability density function such that

$$p(\vec{r}, t) = \mathcal{F}^{-1}\{S(\vec{q}, t)\} = \int_{\mathbb{Q}^3} S(\vec{q}, t) \exp(i\vec{q} \cdot \vec{r}) d\vec{q},$$

where  $\mathcal{F}^{-1}$  is the 3D inverse Fourier transform. Then, the dODF  $\Psi$  can be reconstructed by radially projecting  $p(\vec{r}, t)$

$$\Psi(\hat{\mathbf{r}}) = \int_0^\infty p(r\hat{\mathbf{r}}, t) r^2 dr, \quad \hat{\mathbf{r}} \in \mathbb{S}^2. \quad (1.3)$$

DSI can detect the multiple fascicle orientation within a voxel. However, it requires strong gradients ( $0 \leq b \leq 20,000 \text{ s/mm}^2$ ) as well as long acquisition time to measure hundreds of directions and b-values. That's why is of real interest in clinical applications.

### 1.4.2 Q-Ball Imaging

The Q-Ball Imaging (QBI) is a method that employ the Funk-Radon transform (FRT) on HARDI derived data to obtain a diffusion ODF (dODF)

$$\Psi(\hat{\mathbf{u}}) = \int_{\Omega(\hat{\mathbf{u}})} S(\hat{\mathbf{q}}, t) d\hat{\mathbf{q}},$$

where  $\Omega(\hat{\mathbf{u}}) = \{\hat{\mathbf{q}} \in \mathbb{S}^2 \mid \hat{\mathbf{q}} \perp \hat{\mathbf{u}}\}$ ,  $\hat{\mathbf{q}} = \mathbf{q}/q$  and  $\mathbf{q} \in \mathbb{Q}^3$ . FRT uses the fact that the diffusion signal  $S(\hat{\mathbf{q}}, t)$  is maximal in the directions perpendicular to the underlying fascicles, see Figure 1.7. The dODF can properly represent the presence and orientation of multiple crossing fascicles. However, the resulted dODF is artificially smooth and inflated compared to the true diffusion ODF. Problematically, this same feature causes QBI to poorly distinguish fibers crossing at tight angles. Some modifications and generalizations to QBI have been published to try to achieve most of the QBI limitations [48, 49, 50].

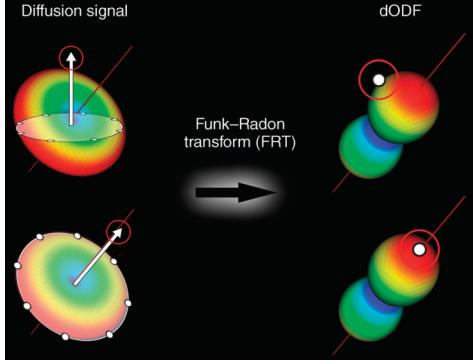


**Figure 1.7:** Illustration of the FRT that QBI uses to reconstruct the dODF using the diffusion MRI measured signal. Image taken from [51].

### 1.4.3 Spherical Deconvolution Methods

Spherical Deconvolution (SD) is one of the most popular techniques to recover the principal diffusion directions from the dMRI data [42]. SD considers the measured HARDI signal  $S$  as the convolution of the fiber response function (FRF), which is an axially symmetric kernel  $R$  that represents a single-fiber response, with the expected true fiber Orientation Distribution Function (fODF)  $F$ , see Figure 1.8. Hence,

$$S(\mathbf{q}) / S_0 = (F \otimes R)(\mathbf{q}) = \int_{\mathbb{S}^2} F(\mathbf{v}) R(\mathbf{q}, \mathbf{v}) d\mathbf{v}, \quad \mathbf{q} \in \mathbb{Q}^3, \quad (1.4)$$

where  $S_0$  is the non-diffusion weighted image. Therefore, the fODF  $F$  can be reconstructed by solving the following optimization problem

$$\underset{F}{\operatorname{argmin}} \frac{1}{2} \sum_{i=1}^n \|S(\mathbf{q}_i) - S_0 \int_{\mathbb{S}^2} F(\mathbf{v}) R(\mathbf{q}_i, \mathbf{v}) d\mathbf{v}\|^2, \quad (1.5)$$

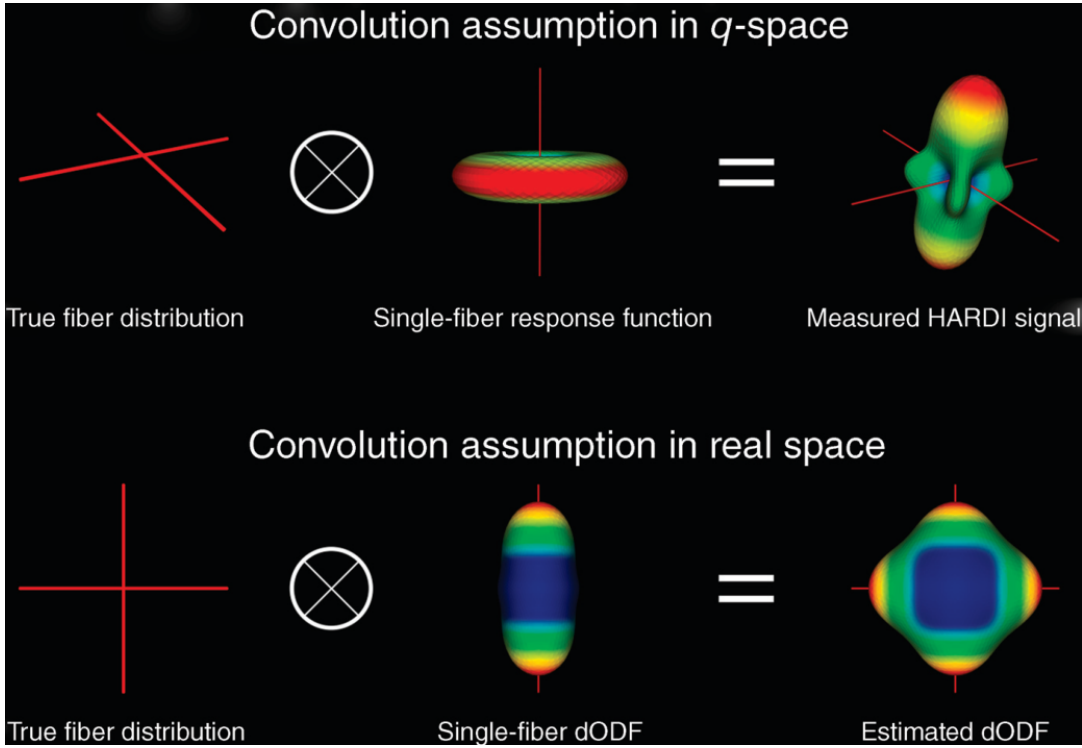


**Figure 1.8:** Convolution assumption in  $q$ -space between the fiber response function  $R$  and the fODF  $F$ . Image taken from [51].

The optimization problem given by Equation 1.5 is usually solved by using Spherical Harmonics (SH) representation (see Appendix A) of the measured signal  $S$ , the kernel  $R$  and the fODF  $F$ . For every harmonic order  $0 \leq l \leq l_{max}$ , let's denote  $\mathbf{S}^l, \mathbf{F}^l \in \mathbb{R}^{2l+1}$  the vector of length  $(2l + 1)$  representing the  $l$ -th order SH decomposition of  $S$  and  $F$ , respectively. Analogously, let  $\mathbf{R}^l \in \mathbb{R}^{(2l+1) \times (2l+1)}$  be the matrix representing the  $l$ -th order rotational harmonic decomposition of the response  $R$ . The spherical convolution operation in Equation 1.4 can thus be reduced to simple matrix operation

$$\mathbf{S}^l = \mathbf{R}^l \mathbf{F}^l. \quad (1.6)$$

Thus, the problem of Equation 1.5 is reduced to

$$\underset{\mathbf{F}^l}{\operatorname{argmin}} \frac{1}{2} \|\mathbf{R}^l \mathbf{F}^l - \mathbf{S}^l\|_2^2, \quad (1.7)$$

where  $\mathbf{F}^l$  is the unknown vector of coefficients of the fODF  $F$ , see Figure 1.9. However, this SD technique is ill-posed and affected by noise.

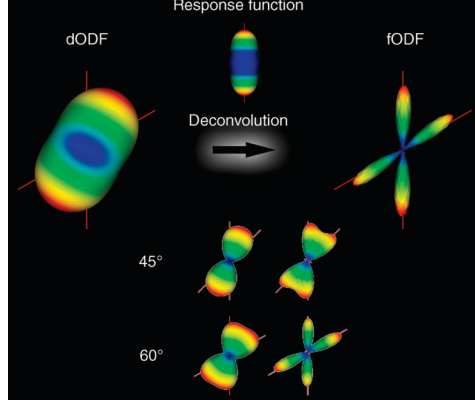


**Figure 1.9:** Spherical deconvolution intuition to improve angular resolution of ODF reconstruction. Assuming a particular response function, the deconvolution will remove the “blurry” part of the diffusion ODF to obtain a sharp fiber ODF that better captures the underlying fiber populations. Hence, a better angular resolution can be obtained, as illustrated in 45° and 60° crossing in the bottom of the figure. Image taken from [3].

Later in [43] was introduced a modification to SD called **Constrained Spherical Deconvolution** (CSD) that preserves the angular resolution while remaining robust to noise effects. In CSD a non-negativity constraint on the estimated fODF is included into Equation 1.7 such that

$$\underset{\mathbf{F}^l}{\operatorname{argmin}} \frac{1}{2} \|\mathbf{R}^l \mathbf{F}^l - \mathbf{S}^l\|_2^2 \quad \text{subject to } \mathbf{R}^l \mathbf{F}^l \geq \mathbf{0}. \quad (1.8)$$

This relies in the fact that negative fibre orientation densities are physically impossible. Besides, this constraint eliminates the need for low-pass filtering the obtained fODF.

An alternate solution to Equation 1.5 is to approximate the fODF using polynomial functions. In [40] it was shown that any homogeneous polynomial  $p$  of order  $d$  can be decomposed into linear combinations of the same order such that

$$p(\mathbf{x}) = \sum_{i=1}^r \lambda_i f_l^d, \quad \mathbf{x} \in \mathbb{R}^l,$$

where  $f_l = \sum_{i=1}^l a_i x_i$ ,  $r$  is the polynomial rank and  $l$  is the polynomial dimension. This decomposition is known as **Symmetric Tensor Decomposition** (STD) [41] because polynomials are directly related to symmetric tensors. With this in mind, the fODF  $F$  can be approximated using an equivalent lower-rank approximation such that

$$F(\mathbf{v}) \simeq \sum_{i=1}^{\tilde{r}} \gamma_i f_i^d = \sum_{i=1}^{\tilde{r}} (\boldsymbol{\alpha}_i \cdot \mathbf{v})^d, \quad \tilde{r} < r, \boldsymbol{\alpha}_i \in \mathbb{R}^3, \mathbf{v} \in \mathbb{S}^2. \quad (1.9)$$

The number of fascicles to be estimated is determined by the approximation rank  $\tilde{r}$ , and each fiber aligned in direction  $\boldsymbol{\alpha}_i$  is identified with a linear form  $(\boldsymbol{\alpha}_i \cdot \mathbf{v})^d$ . In the end, substituting Equation 1.9 into Equation 1.5 leads to the following non-linear optimization problem

$$\min_{\boldsymbol{\alpha}_j} \frac{1}{2} \sum_{i=1}^n \| S(\mathbf{q}, b) - S_0 \int_{\mathbb{S}^2} (\boldsymbol{\alpha}_i \cdot \mathbf{v})^d R(\mathbf{q}, \mathbf{v}) d\mathbf{v} \|^2. \quad (1.10)$$

This is solved for the coefficients of the linear-forms, which are 3 coefficients for each fascicle; all of them are estimated directly from the measured dMRI signal  $S$ . This method avoids the complexity of extracting the orientations from the ODF and can recover complex fascicles configuration using less parameters.

#### 1.4.4 Multi-Tensor Methods

Multi-tensor representation or Multi-tensor Model (MTM) is a natural extension of DTI, where orientated diffusion along the fascicles is represented with a mixture of Gaussian distributions at each voxel such that

$$E(\mathbf{g}_i, b) = \sum_{k=1}^N \alpha_k \exp(-b \mathbf{g}_i^T \mathbf{D}_k \mathbf{g}_i). \quad (1.11)$$

Initially, the expectation maximization algorithm was used to solve Equation 1.11. However, this algorithm is unable to handle physiological constraints on the eigenvalues. Later, in [5] a gradient descent scheme with multiple restarts was employed to solve, by considering the mentioned constraints, the Equation 1.11 for the eigenvectors of  $\mathbf{D}_k$  and volume fractions  $\alpha_k$ , while the eigenvalues of  $\mathbf{D}_k$  were specified a priori or restricted to a particular range. However, these and others [6, 7, 8] proposed methods to solve the MTM have been reported to be numerically challenging and unstable. Later, in [14] was provided the first analytical demonstration that when using a diffusion MRI acquisition with only one non-zero b-value, such as in conventional single-shell HARDI acquisition, a co-linearity in model parameters makes the precise model estimation impossible.

##### 1.4.4.1 Diffusion Bases Functions

Diffusion Bases Functions (DBF) is a dictionary-based method for the estimation of the intra-voxel configuration [13]. A set  $\{\Phi_j\}_{j=1}^J$  of  $J$  basis functions are generated using the radially symmetric diffusion tensor. Then, the diffusion signal  $S$  can be expressed in matrix form

$$S = \Phi\alpha, \quad (1.12)$$

where  $S = (S(\mathbf{g}_1, b), \dots, S(\mathbf{g}_n, b)) \in \mathbb{R}^n$  is the vector of diffusion signal samples,  $\alpha \in \mathbb{R}^J$  is the vector of contributions for each basis function and  $\Phi \in \mathbb{R}^{n \times J}$  is the dictionary containing all  $J$  basis functions of size  $n$ .

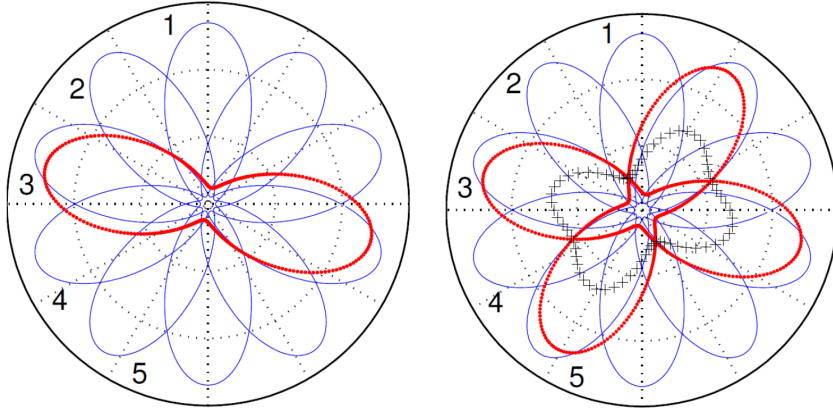


**Figure 1.10:** 2D schema of DBFs. The blue lines correspond to a dictinoary with  $J = 5$  basis functions. (a) Continuous-blue line shows the DBFs generated by an uniformly distributed tensor basis with  $J = 5$ . The doted-red line represents the normalized diffusion signal  $S(\mathbf{q})$  generated by an arbitrary diffusion tensor. In this case, the solution for  $\alpha$  is expected to be  $\alpha = (0, 0, 1, 0, 0)$ . (b) Schema for two fiber case, the dotted-red lines represent the signals for two arbitrary tensors, which their half-addition of both signals are shown in the cross-marked black line. For this case, the solution is expected to be  $\alpha = (0, 0, 0.5, 0, 0.5)$ . Image taken from [13].

Finally, Equation 1.12 is solved for  $\alpha$  using a basis pursuit technique, which compute the solution by means of non-negative least-squares of the form

$$\min_{\alpha} \|\alpha\|_1 = \sum_j \alpha_j \quad \text{subject to } S = \Phi\alpha, \quad \alpha_j \geq 0, \quad j = 1, \dots, J.$$

#### 1.4.4.2 Multi-Resolution Discrete-Search

Actually, there is a multi-tensor based method, which represents multiple fascicles with multi-tensors fitted using the **Multi Resolution Discrete Search** (MRDS) approach [10]. MRDS is capable of providing individual diffusion profiles as well as the orientation of the fasicles. MRDS is a general framework for estimating parameters in a multi-compartment representation. The normalized DWI signal attenuation  $E_i = S_i/S_0$  at each voxel of a multi-compartment model is represented as

$$E_i = \sum_{k=1}^N \alpha_k \Phi_i(\zeta_k) + \eta_i, \quad i = 1, 2, \dots, n, \quad (1.13)$$

where  $N$  is the number of compartments,  $n$  the number of DEOs,  $\{\alpha_k > 0\}_{k=1}^N$  denotes the compartment sizes (volume fractions) and  $\eta_i$  represents the signal noise. Besides,  $\Phi_i(\zeta_k)$  is the signal response of the compartment function for the DEO  $g_i$  defined by the parameters  $\zeta_k$ , which is a vector in the form  $\zeta_k = (\theta_k, \xi_k)$ , where  $\theta_k = (\theta_k^z, \theta_k^a)$  define the zenith (elevation) and azimuth angles of the PDD of the compartment. On the other hand,  $\xi_k$  is the vector of parameters associated with the tissue properties for the compartment  $k$ . Assuming Gaussian noise, the error function to be minimized is

$$\epsilon(N, \alpha, \theta, \xi, E) = \sum_{i=1}^n \left( \sum_{k=1}^N \alpha_k \Phi_i(\zeta_k) - E_i \right)^2 \quad (1.14)$$

Note that in the particular case of a **multi-tensor model** (MTM) representation we have  $\Phi_i(\zeta_k) = \exp(-b_i g_i^T D_k g_i)$ , where  $\xi_k = (\lambda_k^{\parallel}, \lambda_k^{\perp})$  represents the axial ( $\parallel$ ) and radial ( $\perp$ ) diffusivities. The PDD  $\theta_k$  defines the rotation matrix  $R(\theta_k)$  associated with  $D_k$  such that

$$D_k = D(\theta_k, \xi_k) = R(\theta_k) \begin{bmatrix} \lambda_k^{\parallel} & 0 & 0 \\ 0 & \lambda_k^{\perp} & 0 \\ 0 & 0 & \lambda_k^{\perp} \end{bmatrix} R^T(\theta_k). \quad (1.15)$$

Therefore, the proposed MRDS algorithm consists in the following steps:

1. Estimation of the orientations  $\{\theta_k\}_{k=1}^N$  and the compartment sizes  $\{\alpha_k\}_{k=1}^N$  for fixed diffusion parameters  $\{\xi_k\}_{k=1}^N$ .
2. Estimation of the diffusion parameters  $\{\xi_k\}_{k=1}^N$  for fixed  $\{\theta_k\}_{k=1}^N$  and  $\{\alpha_k\}_{k=1}^N$ .
3. Repeat previous steps until convergence.
4. The output of the previous steps consists of the best possible configurations for 1, 2 and 3 fascicle orientations and diffusivities. Finally, in this step a model selector determinates the optimal value for the number of bundles for the considered voxel.

MRDS has proved to be more robust to noise and crossing fascicles than other methods like DIAMOND and CSD [9].

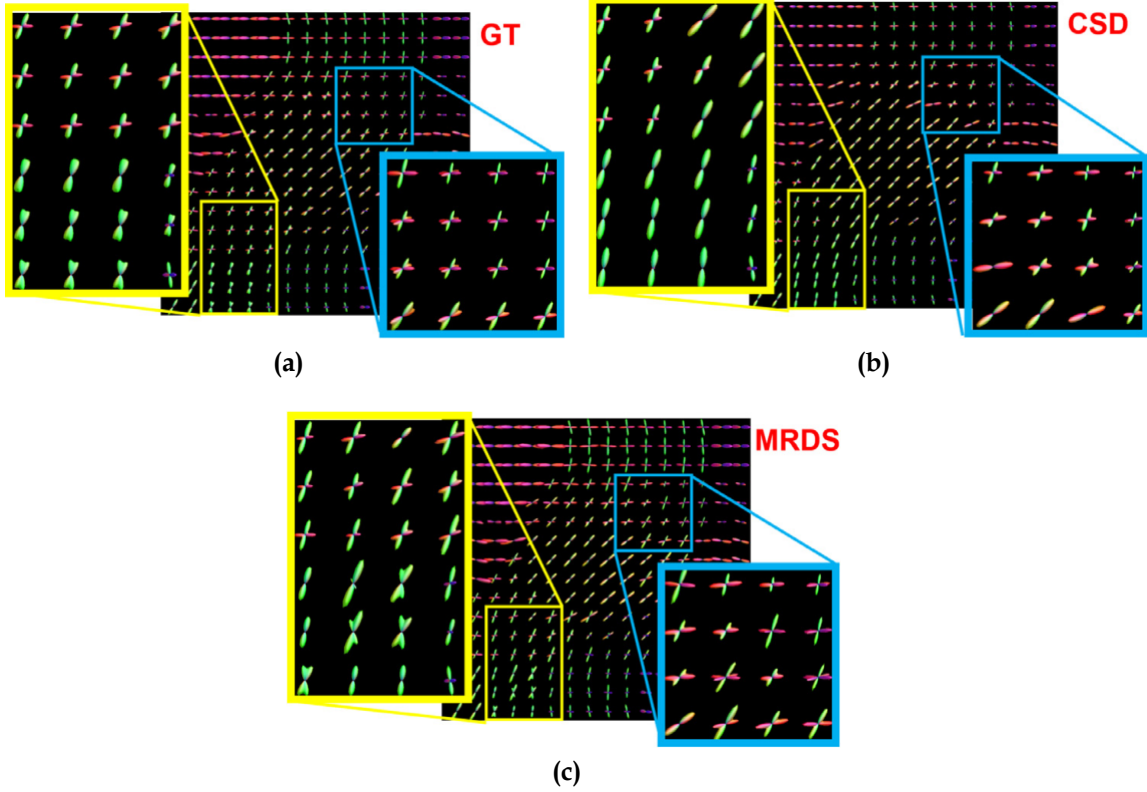


**Figure 1.11:** Quantitative comparison on simulated data. Reconstructions of the ODFs are shown for the Ground Truth (a), CSD (b) and MRDS (c).

#### 1.4.4.3 DIAMOND

DIAMOND stands for Characterizing the DIistribution of Anisotropic MicrO-structural eNvironments with Diffusion-weighted imaging (DIAMOND) [15]. This method consider that the measured signal can be described by a sum of signals arising from a large number of individual spin-packets within the voxel. Each spin-packet undergoes homogeneous 3D Gaussian diffusion represented by a diffusion tensor  $\mathbf{D}$ , whose contribution to the signal for a DEO  $\mathbf{g}_i$  is

$$S_0 \exp(-b_i \mathbf{g}_i^T \mathbf{D} \mathbf{g}_i) d\mathbf{D}.$$

A matrix-variate distribution  $P(\mathbf{D})$  determinates the fraction of spin-packets described by a same tensor  $\mathbf{D}$ . Thus, the DIAMOND representation is given by

$$S(\mathbf{g}_i, b_i) = S_0 \int_{\mathbb{D}} P(\mathbf{D}) \exp(-b_i \mathbf{g}_i^T \mathbf{D} \mathbf{g}_i) d\mathbf{D}, \quad (1.16)$$

where  $\mathbb{D}$  is the set of symmetric positive-definite  $3 \times 3$  matrices. When a voxel is composed of one single fascicle, Equation 1.16 matches with DTI.

On the whole, one of the main challenges in building accurate models is to find a balance between the complexity and the number of parameters of the model [17]. Models with few parameters have a low level of complexity and are easier to fit. However, these models tend to underfit the data because they do not have enough flexibility to capture variations in the diffusion signal. On the other hand, high complexity models are more robust and capable of capturing variations in the diffusion signal. But they have many parameters to tune and tend to overfit the data.

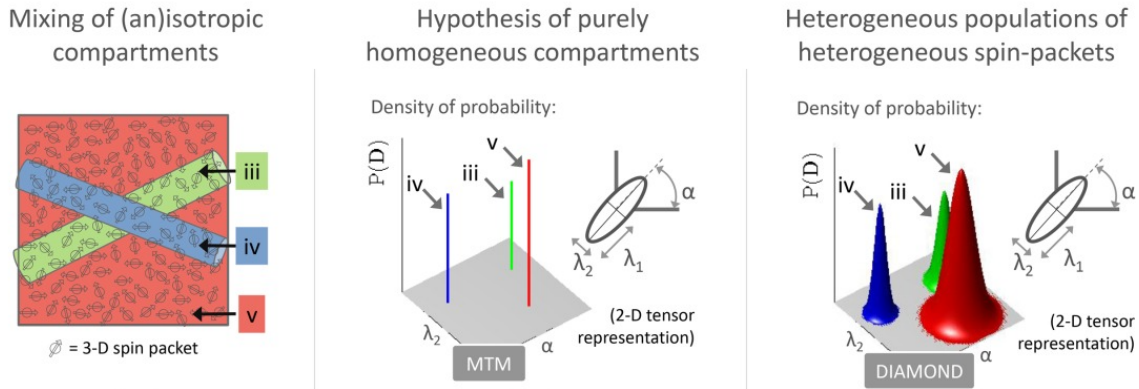


**Figure 1.12:** (left) Hypothetical multi-compartment model, in which an isotropic (red) and two anisotropic (blue and green) compartments are mixed. For illustration purpose we represent here a 2D multi-compartment model. (middle) Under the hypothesis of purely homogeneous compartments with no exchange, a multi-tensor model is typically used to describe the signal arising from the multi-compartments. The corresponding probability density of diffusivities is composed of a mixture of delta functions. (right) DIAMOND captures the multidimensional diffusivity and heterogeneity of each compartment using peak-shaped distributions of multidimensional diffusivities. The expectation of each matrix-variate distribution captures the compartment overall diffusivity while the distribution concentration captures its microstructural heterogeneity. Specifically, a distribution with a broad peak indicates a highly heterogeneous compartment. Imagen taken from [15].

## 1.5 Tractography

Diffusion tractography or white matter fiber tracking is a process, where three-dimensional axonal trajectories can be tracked using information from dMRI data [62]. Captured pathways - also known as **streamlines** or **tracks** - are represented as curves in a 3D space, i.e. a streamline is mathematically written as a set of  $M$  points  $\{\mathbf{p}_i \in \mathbb{R}^3\}_{i=1}^M$ , see Figure 1.14. The set  $\mathcal{T}$  containing all these streamlines is called **tractogram**. Tractograms provide a helpful and non-invasive form for

inferring the connectivity structure of the in-vivo white matter.

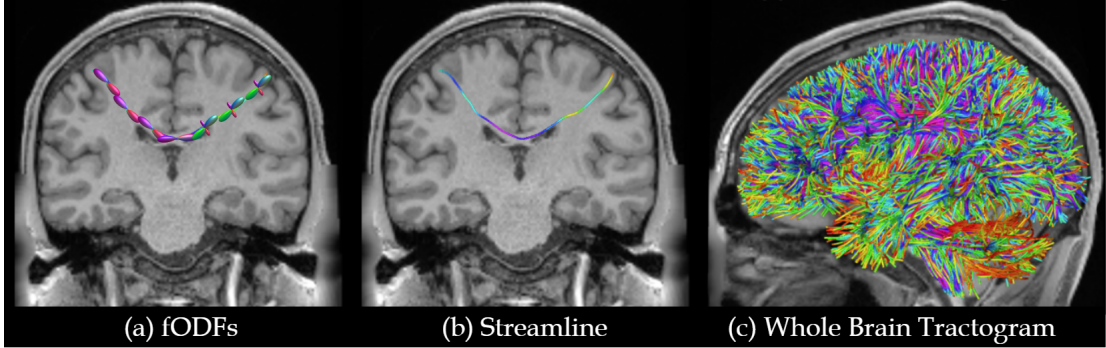


**Figure 1.13:** Graphic illustration of tractography. (a) Example of fODFs that can be followed to reconstruct (b) an individual streamline computed after performing tractography. (c) An example whole-brain tractogram that consists of streamlines covering the entire white matter. Image taken from [65].

Some tractography algorithms are based on the intuitive principle of propagation. They initialize every streamline in the white matter and propagate a line by following the local dominant diffusion orientation, see Figure 1.14. There are different strategies to initialize the streamlines. For example, streamlines can start in a random seed located in the white matter. An alternative approach for streamline seeding is to seed within the grey matter or at the grey matter-white matter interface, and track unidirectionally [104]. Other common procedure is to use a region-of-interest (ROI) as starting point for the streamlines [105]. After the initialization of every streamline, propagation algorithms have to extend the streamlines. Pioneer propagation algorithms were implemented by taking information from the diffusion tensor [63, 64] to propagate the streamlines. In particular, the PDD of the tensor is used as it is linked to the maximum diffusion direction, see Figure 1.14. Additionally, it is necessary to define when streamlines have to finish propagating. For this, a termination criterion is required. In some algorithms, streamlines propagation terminates when they reach a region with low anisotropy like gray matter, where there is no coherent direction to follow. Thus, a FA threshold is set to determine when streamlines are in an isotropic region. Typically, that threshold for tracking termination is set equal to 0.2 as FA in the gray matter is in the range [0.1, 0.2]. Nonetheless, there are more termination criterion that can be considered, for example, the angle change between pixels.

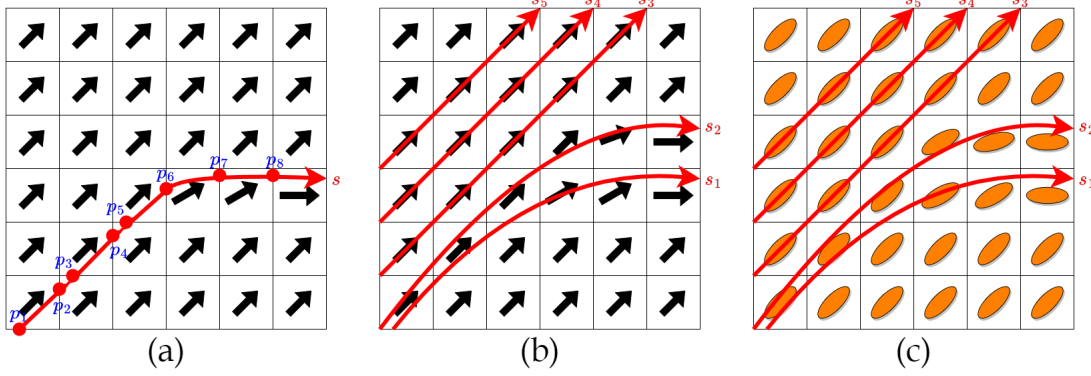


**Figure 1.14:** Illustration of the main diffusion directions (black arrows) forming a vector field. (a) A streamline  $s = \{p_i\}_{i=1}^8$  (red arrow) is shown following the vector field. It can be seen how the streamline is composed of points in the space (red points). (b) A tractogram  $\mathcal{T} = \{s_i\}_{i=1}^5$  consisting of 5 different streamlines obtained by pursuing the maximum diffusivity direction. (c) Illustration of how the diffusion tensor can be used to represent the dominant diffusion direction.

Tracking algorithms based on DTI have an important limitation handling voxels with multiple crossing fascicles, which leads to “pancake” shape rather than elongated tensors, see Figure 1.3. In these cases, the main diffusivity direction is not well defined. Thus, DTI tracking techniques produces streamlines that are not anatomically plausible (**false positives**). With this in mind, HARDI [51] data and new methods like spherical deconvolution [42, 43, 44, 66, 67, 68, 69, 70, 71, 72, 73, 74, 75, 76, 77], have allowed to detect crossing fascicles within a voxel for a more robust tractography [103]. Notwithstanding, HARDI fiber tracking techniques have not solved all the tractography hitches. Moreover, HARDI techniques also have some limitations. For example, it cannot differentiate between crossing, kissing, or branching fascicles configurations, and some acquisition times are still too long for clinic applications, among others.

Propagating algorithms constitute a whole family of **local** tracking techniques. The difference between them is how they use the local information to reconstruct the streamlines. Furthermore, several alternative tractography algorithms have been proposed, and they can be cataloged in different families. For instance, **global** tracking techniques simultaneously fit the entire tractogram to all image data by iteratively perturbing a set of candidate trajectories [87, 88, 89, 90], or progressively forming linked chains from a large set of randomly-initialized short streamline segments [80, 81, 82, 83, 84, 85, 86], see Figure 1.15. In addition, front evolution [71, 78, 79], geodesic [95, 96, 97, 98] and machine learning [91, 92, 93, 94] algorithms are current in development. Despite a large number of studies has been published, where different tractography algorithms are compared [99, 100, 101, 102], there is no a definitive algorithm to track the white matter. That’s one of the reasons trac-

tography, as field of study, is ample and currently active.

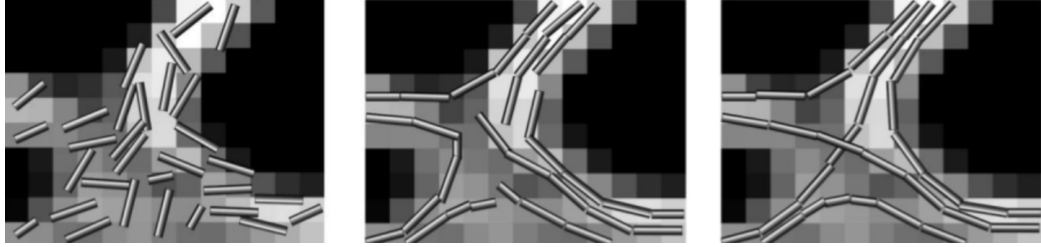


**Figure 1.15:** Example of the steps performed in the Gibbs tracking technique to simultaneously fit a whole tractogram to the dMRI data. Image taken from [106].

It is important to remark that streamlines do not represent real axonal tracts, but they represent the most plausible path of water diffusion. Besides, tractography is sensitive to the chosen tracking algorithm, i.e. quantitative analyses may be affected by the underlying algorithm or the parameters (seeds, stop criterion, etc.). Taking everything into account, caution must be taken when drawing conclusions on brain connectivity or brain functions.

## 1.6 Tractometry

When tractography reconstructions and metrics derived from diffusion quantification are combined, the term “tractometry” is used [120, 121]. In tractometry, diffusion metrics are typically averaged over the tracts of interest, see Figure 1.16. The analysis of these metrics along the tracts is called “tract profiles” [122, 123, 124].

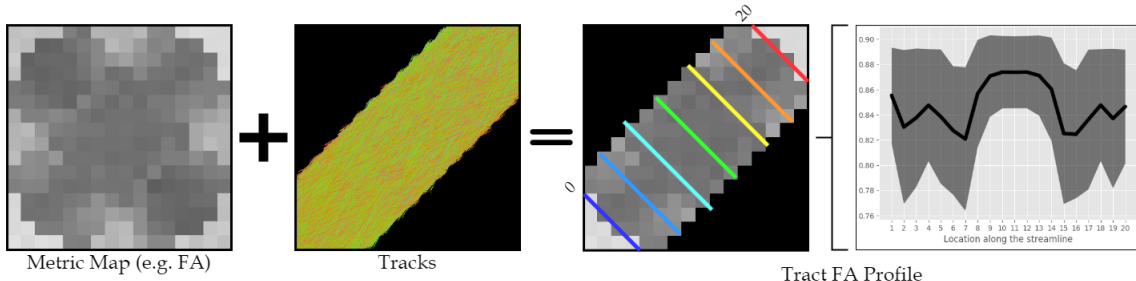


**Figure 1.16:** Illustration of how the dMRI metrics and the tracks are combined using tractometry to get the tract profile. (left) FA map. (middle) tracks along the bundle. (right) tract profile obtained from the tractometry. Rainbow colors mark the locations along the streamlines. Tract profiles can be plotted using the values along the streamlines (20 locations for this example).

In [120, 121] was compared the Quantitative Magnetization Transfer (QMT) imaging and the Myelin Water Fraction (MWF) to dMRI metrics; analysis were reported on a voxel by voxel basis or averages within regions of interest. In [126] an analysis of tract-averaged values was made about the relationship between the proton Bound Pool Fraction (BPF) and FA in a set of white matter tracts. Another framework called profilometry has been proposed in [119] to make a joint analysis of multiple metrics, including both dMRI metrics and metrics non derived from dMRI like the MWF. It was applied to both MS cohort and single MS patients. In particular, in [128] was proposed a pipeline called tractometry\_flow that independently process each dissected bundle of a whole brain tractogram, combining them with DTI-based metrics as well as HARDI-based metrics. First, the tractometry\_flow pipeline removes spurious streamlines using hierarchical QuickBundles [131]. Then, centroids are computed as a mean streamline of the bundle using the minimum-distance-flipped metric [132]. Centroids are subsampled in equidistant points, and All points of every streamline in the each bundle are assigned to the closest centroid point. After that, tractometry\_flow projects the metric values of an input metric map to these assignments, and computes an average metric value per subsampled point along the bundle. In order to mitigate the contribution of spurious streamlines to the averaged value in each voxel, all voxels are weighted by its relative geodesic distance to the closest centroid point. In the end, a tract profile is extracted for every combination of metrics and bundles, see Figure 3.1.

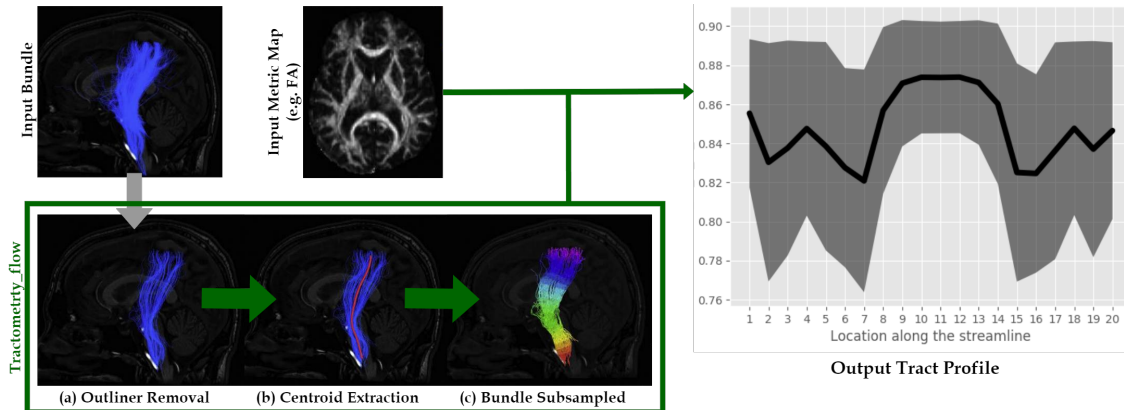


**Figure 1.17:** Important steps of the tractometry\_flow pipeline illustrated on the corticospinal tract (CST) using the FA metric. (a) Outliers are removed. (b) Centroids are extracted. (c) The bundle is subsampled. Image taken from [128].

In general, tractometry is a statistical analysis that compares different groups or assesses individual variability in brain connection structure.

## 1.7 Phantoms

Either in neuroscience research or clinical applications, validation is a requirement. Estimation of the fiber tracts and tissue profiles is extremely challenging. Besides, it is well-known that there is no in-vivo data with a real ground truth (GT) that could be used for validation. An extensively and successfully substitute for in-vivo GT is the use of synthetic phantoms. They constitute a controllable scenario that provides precise information of the underlying microstructural properties (e.g. local fiber orientation, geometrical configuration of fiber tracts, tissue properties, etc.). There are plenty of phantoms in the state-of-the-art that serve as validation tools for quantitatively and qualitatively evaluation of the performance of tractography [38] and microstructural estimation of diffusion MRI metrics [39]. Phantoms can be classified into two groups: physical and digital phantoms.

### 1.7.1 Physical Phantoms

It is possible to build hardware objects with arrangements of fibers crafted using synthetic, natural or glass fibers filled or soaked in a liquid [28, 29, 30, 31, 32, 33, 34, 35, 36, 37]. This emulates the water diffusion in restricted tissue. These phantoms can be imaged using a magnetic resonance scanner to get a diffusion-weighted signal because they are real world objects.



**(a)** Example of 90° and 45° physical phantoms resulting from a manual wiring of acrylic fibers (outer diameter of 17  $\mu\text{m}$ ) inside a container incorporating the negative mask of the target fiber bundles. Image taken from [28].



**(b)** Filling of a diffusion MRI tractography phantom under vacuum conditions and post-sonication to avoid the presence of air bubbles inside the fiber bundles. Image taken from [38].

**Figure 1.18:** Example of physical phantoms used for tractography validation.

### 1.7.2 Digital Phantoms

In contrast to physical phantoms, digital phantoms - also called numerical phantoms - are digital objects generated with a computer software. They consist of

multiple components: (1) A structure model defining the simulated fiber configuration, (2) a diffusion model describing the water diffusion in the structural model, which determinates the signal attenuation in the diffusion-weighted signal, and (3) an algorithm that simulates the signal using the previous two components.



**Figure 1.19:** Illustration of the Phantomas phantom used for 2nd HARDI Reconstruction Challenge5, organized at ISBI 2013. It consists of 27 fiber bundles, on a  $70 \times 70 \times 70$  grid, with 3 spherical CSF regions abstractly mimicking a human brain. Image taken from [38].

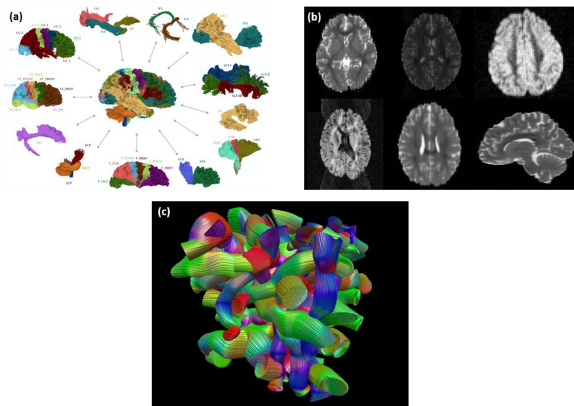


**Figure 1.20:** Illustration of the 71 tracts used for the 99 brains Fiberfox simulation (a), exemplary axial slices of one simulated subject of the 99 brains dataset with various artifacts (b), and an exemplary phantom with randomized bundle configuration generated using Fiberfox (c). Image taken from [38].

Both physical and digital phantoms have their own advantages and limitations according to the use-cases. The most important difference between them is that even with a well defined physical phantom, it is not possible to provide such a perfect ground truth because of, for example, mechanical limitations or the statistical nature of the diffusion process [38]. Hence, digital phantoms are the only way to obtain a dMRI data with a real ground truth. That's why we have decided to use a digital phantom for this work. We will discuss the selected phantom in the next chapter.

## 1.8 Multiple Sclerosis

Multiple Sclerosis (MS) [139, 138, 137, 136, 142, 145, 144, 143] is a common neurological disease that affects primarily young adults. Usually, persons between the ages of 15 and 50 (average of 30) are affected by MS. It is present 2-3 times more often in women rather than men [149]. However, the reasons are still unclear. MS begins with episodic attacks of neurological symptoms. Then some years later, it enters in a progressive phase [138, 139, 141]. MS may have different stages [150] after the first symptoms appear. For example, a **relapsing-remitting** stage, which consists of attacks and remissions of symptoms. Many patients will later make the transition to a **secondary-progressive** stage or they could begin with a **primary-progressive** stage with slow progression without attacks. Recently, there has been some patients that began as progressive, but later they have one or more acute relapses. These cases are called **progressive-relapsing** type of the MS disease. Although the cause of MS is unclear, it is well-known that MS is not a 1-factor disease, but multiple factors are involved. Some factors like genetics (e.g. HLA DRB1\*15:01) [147], environmental (e.g. low vitamin D levels) [146] and lifestyle (e.g. cigarette smoking) [148] contribute to the development of MS.

Inflammatory processes in the Central Nervous System (CNS) characterized by breakdown in the myelin that surrounds axon nerves. Breakdowns in the blood-brain barriers allows immunologically active cells in the blood to enter the brain and cause patchy damage to myelin. These scattered circumscribed lesions are called **plaques** [140] and cause the symptoms of MS slowing or disrupting conduction in the axons as myelin is necessary for the conduction in myelinated nerves. The plaques are characterized by inflammation, demyelination and scarring known as **gliosis**. Some axons can remyelinate again causing some remissions after an attack. Inflammation and gliosis are evident on Diffusion Magnetic Resonance Imaging (dMRI) scans [135], see Figure 1.21. The presence of characteristic changes on the dMRI images raised a massive number of studies and analyses, which have shown the capabilities of dMRI to effectively detect, differentiate and individually quantify the normal appearing white matter in MS and, more importantly, axon injury/loss, demyelination and neuroinflammation. Considering all this, dMRI is a unique tool to quantify and assess MS and other neurological diseases in a non-invasive way.

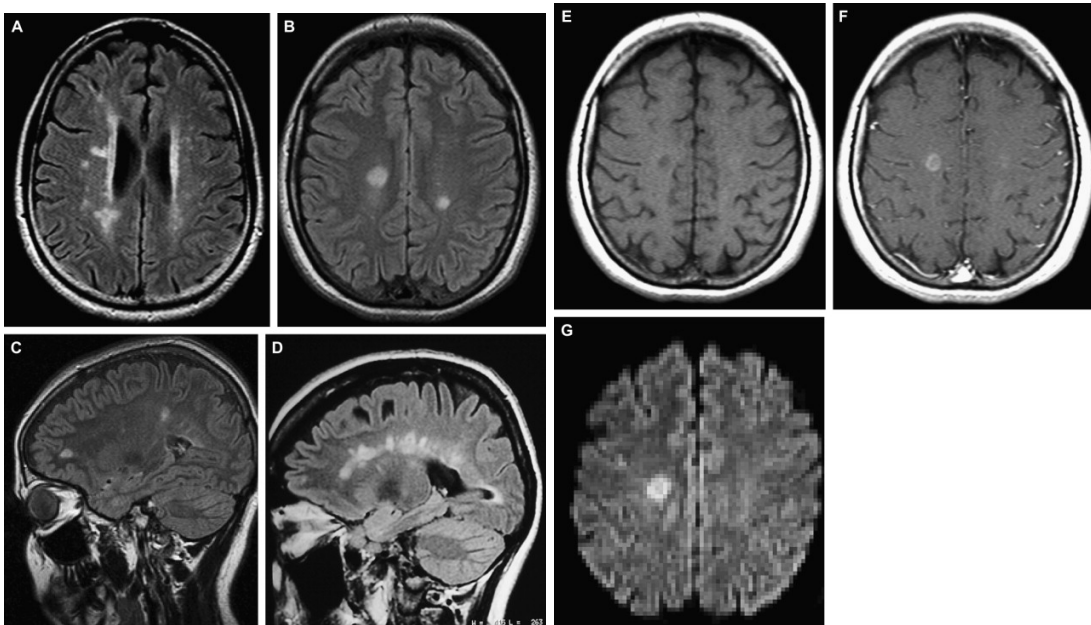


**Figure 1.21:** Different imaging features in MS. (A, B) Axial fluid-attenuated inversion recovery (FLAIR) shows typical appearance of deep WM plaques like multiple hyperintense lesions in subcortical and cerebral deep WM, mostly ovoid in shape. (C, D) Sagittal FLAIR shows demyelinating plaques along the margin of lateral ventricles and the corpus callosum, with the typical radial arrangement, called Dawson fingers. Axial T1-weighted images before (E) and after (F) gadolinium administration show a single plaque in the right frontal lobe, which shows enhancement after contrast injection, consistent acute inflammatory demyelination. (G) Diffusion-weighted imaging reveals a high signal lesion, which may be related to the acute phase of the disease. Images taken from <https://radiologykey.com/diffusion-magnetic-resonance-imaging-in-multiple-sclerosis>.

## 1.9 Motivation

Extensive research has been carried out that applied DTI metrics to quantify myelin and characterize demyelination in MS [154, 155, 156, 157]. All these studies and reviews found that there are significant increases in RD and decreases in AD, which drive to substantial decreases in FA and increases in MD. Although RD is suggested as the closest biomarker of demyelination [133, 134], none of them have proven to be a specific imaging biomarker of myelin [158, 159, 160, 161]. In particular, all of them tend to lack specificity to characterize the underlying microstructure in crossing fibers. Classical DTI measures are very sensitive to white matter anomalies [162, 163, 16]. Now, it is very well-known that several different microstructure scenarios may lead to such changes in DTI metrics, see Figure 1.22. For example, the following scenarios could lead to the same FA of 0.4 :

- Crossing fiber voxel.
- Single fiber population demyelinating (going from FA of 0.7 to 0.4).
- Voxel that has partial volume with a CSF.
- Isotropic free water from neuroinflammation contaminating the voxel leading to a drop of a high FA voxel to a low FA of 0.4.

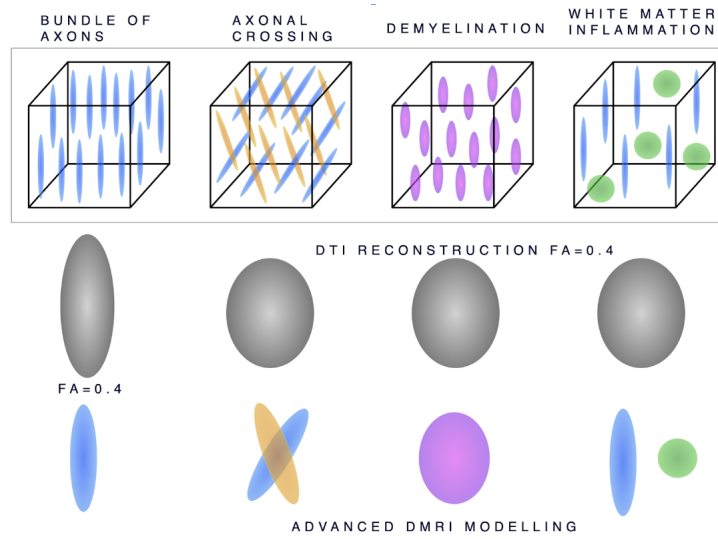


**Figure 1.22:** Limitations of DTI and potential of advanced diffusion MRI modeling for improved brain connectivity mapping and track-specific white matter tissue assessment.

It is thus clear that it is necessary pixel-specific measures for the analysis of demyelination, and we need them to be robust to crossing fibers.

# Chapter 2

## Problem Statement

In general, a tractometry analysis brings together the outputs of tractography and advanced metrics from local diffusion models to get a measurement of the physical properties of brain tracts. Thus, tractometry is an important utensil to study the brain and neurodegenerative diseases. However, the current tractometry frameworks are based on metrics derived from single tensor or fixel-based metrics derived from methods other than dMRI. Besides, there are several challenges facing researchers who use tractometry such that:

- Need of cutting edge multi-shell acquisition schemes of dMRI.
- There are many ways to model or represent dMRI data. This includes different sophisticated local diffusion models at the level of individual voxels, and different parameters configurations of the same model.
- Tracking techniques to reconstruct the WM fascicles, which involves a large number of parameters.
- Robust multi-parameter approaches to classify whole brain tractograms into major WM fascicles. These fascicles are hard to define and recover robustly because they have variable spatial extent.
- Adjustment of all involved parameters to apply tractometry beyond phantoms, i.e. in real life applications like MS.

Multi-shell dMRI is now widely used. Nonetheless, the most appropriate representation and modeling of multiple fascicles traversing the same voxel remains unclear. Simple models like DSI and QBI do not make assumptions on the dMRI data and are sensitive to fiber crossing, but they focus on describing the general shape of the diffusion profile in each voxel instead of representing each fixel independently, and therefore they do not enable characterization of each individual fixel. On the other hand, spherical deconvolution methods provide fixel-based metrics and orientations, but they are not capable of proving metrics like fixel-RD,

which is ideal for MS applications as it aims to characterize the demyelination. In addition, advanced local diffusion models like MRDS and DIAMOND that allow to estimate fixel-based dMRI metrics are still slow and inefficient.

Tractometry analysis informed with fixel-based dMRI metrics needs to be translated to MS and other neurodegenerative diseases, and this is still a very important open problem. That's why it is important to study a tractometry pipeline informed with fixel-based dMRI metrics like fixel-RD, which aims to achieve the crossing fiber limitations of dMRI metrics derived from single tensor.

## 2.1 Objective

Our main objective is to setup a robust (to noise and crossing fibers) pipeline for the automatic extraction and statistical analysis of track-specific white matter measures, which will be useful in MS to characterize demyelination. Estimated fixel-based orientations and metrics will be used as indirect proxies to axon loss, demyelination and neuroinflammation. In particular, we envision that the fixel-based RD (fixel-RD) could help to account for demyelination [119].

In order to achieve our main objective, we will face several challenges. The first one is to select a method to estimate the fixel-based dMRI metrics. Both MRDS and DIAMOND can estimate fixel-based dMRI profiles. But we decided to use the MRDS method instead of DIAMOND to estimate the fixel-based dMRI metrics. MRDS is a simpler model than DIAMOND when representing the dMRI data. However, MRDS needs less parameters compared with DIAMOND. Thus, we have the hypothesis that MRDS is a viable trade-off between complexity and number of parameters for clinic data. Besides, MRDS has been shown to be more robust to noise than DIAMOND when estimating the orientations of the fixels [9]. On the other hand, CSD is not an option in this case as it is unable to estimate fixel-RD metrics. On the whole, there are 3 main problems that have to be addressed:

1. Fast, accurate and robust (against noise and fiber crossing) estimation of fixel-based dMRI metrics from the dMRI data using the multi-tensor based method MRDS. This, by itself, implies several challenges:
  - (a) Improve the model selector in MRDS to better estimate the number of tensors per voxel. MRDS tends to overfit the number of tensors per voxel.
  - (b) Parallelization of MRDS using modern GPU parallel programming techniques to ensure fast fitting of the MRDS method to the dMRI data. Currently, MRDS faces long fitting times. For some real human brain data sets it takes 2 entire days for fitting a single brain, using modern CPU with tens of cores.

- (c) Validate the new model selector and the parallelization implementation using synthetic phantoms.
- 2. Multimetric analysis of white matter tracts in different fiber bundles. It's required to adapt the tractometry\_flow pipeline to integrate the fixel-based MRDS metrics into the statistical analysis.
- 3. Build and validate a new tractometry pipeline with MRDS and tractometry\_flow by adding the previous improvements and including other steps based on methods in the state-of-the-art that we will describe in the next chapter.
- 4. Perform a MS study by applying this new pipeline. Although this new pipeline for automating tract-profiling in the white matter could improve brain connectivity mapping through crossing fiber regions and pathologies in the human brain, we will focus to demonstrate the application of our pipeline to relapsing remitting MS with a unique acquisition paradigm of 5 timepoints over 6 months with MS-based dMRI and myelin-based MRI.

Lastly, together the optimizations for MRDS in points 1 and 2 will result in a journal publication. Besides, the pipeline resulting pipeline in point 3 will generate another journal publication.

# Chapter 3

## Methods

### 3.1 Pipeline

Our proposed pipeline is composed of 4 main parts:

1. Preprocessing of the dMRI and T1 data, and reconstruction of the initial tractogram by using tractography. This step is based in the Tractoflow pipeline [113] with an additional step for correcting the Rician bias [111].
2. Major white matter bundles extraction from the whole-brain tractogram using RecoBundlesX [115, 116, 117, 118].
3. Fixel-based metrics estimation for each voxel using a GPU-optimized MRDS method applied to the MTM [10].
4. Tract profiles extraction for every combination of metrics and bundles using Tractometry\_flow adapted to the MRDS metrics [128, 129, 130].

Each of these steps is explained with more details in the incoming sections, see Figure 3.4.

#### 3.1.1 Preprocessing and Tractography

Tractoflow [113] is a pipeline based on two engines: Nextflow and Singularity that allows to analyze a whole dMRI data set in only one simple script. Tractoflow pipeline consist of 23 different steps: 14 steps for the diffusion weighted image processing and 8 steps for the T1 weighted image processing, see Figure 3.1.

- Bet Prelim DWI: a preliminary brain mask is extracted using the Brain Extraction Tool (BET) command [108].
- Denoising: this step removes the noise induced by the dMRI acquisition. It uses the `dwidenoise` tool available in MRtrix [58] that is based in the MP-PCA method [109].

- Eddy/Topup: this step corrects the brain deformation induced by the magnetic field susceptibility artifacts. After that, Eddy corrects eddy-currents, motion artefacts and performs slice-wise outlier detection and correction. The preliminary brain mask is used to accelerate this process by only processing voxels in the mask.
- Brain Extraction: the extraction is performed on the  $b = 0$  image. Then, brain mask is applied to the whole dMRI image. This second brain extraction gives a distortion-free brain mask.
- N4 Bias Correction: the center of the brain image is less intense than its outer boundary. The N4 Bias Correction normalizes the image intensities to reduce this intensity bias. N4 correction is performed on the  $b = 0$  image with the ANTs command **N4BiasFieldCorrection** [110]. Later, the bias field is applied to the whole dMRI image. It is important that this step comes after the Eddy/Topup to avoid modifying the intensity values that are important for the deformation bias and eddy-current corrections.
- Gudbjartsson Correction: low signal intensities ( $SNR < 2$ ) are biased due to the noise. The underlying noise can be estimated from the dMRI image in the denoising step, and a simple correction scheme is applied to reduce the Rician bias based on the Gudbjartsson correction scheme [111]

$$\tilde{S}(\mathbf{g}_i, b_i) = \sqrt{|S(\mathbf{g}_i, b_i)^2 - \sigma^2|}, \quad (3.1)$$

where  $\sigma$  is the variance of the noise obtained from the denoising step. The correction scheme is applied using the **mrcalc** command from MRtrix [58].

- Crop: the bounding box of the dMRI image is reduced using DIPY [57] to accelerate the following steps.
- Normalize: intensities in the dMRI image are normalized using the **dwinormalise** command included in MRtrix [58]. Normalization is such that the intensity mean value in the water matter is  $\sim 1000$ .
- Resample: the dMRI image is resampled to  $1\text{mm}$  isotropic spatial resolution to match the spatial resolution of the T1 image.
- Local Modeling for Tractography: shells corresponding to b-values  $b = 0, 1000, 2000 \text{ mm}^2/\text{s}$  are extracted to compute the fODF image. The fiber response function used is the average of the subjects. The, the fODF is computed using CSD with  $l_{max} = 8$ .

- Tractography: a fODF-based tractography algorithm is used with a probabilistic anatomically-constrained particle filter tracking and relaxation stopping criterion [107]. It uses the fODF image from the previous step, a white-matter mask as seeding mask with 10 seeds per voxel. Other parameters such as the step size, maximum angle, and usual streamline-based tracking parameters were left as default.

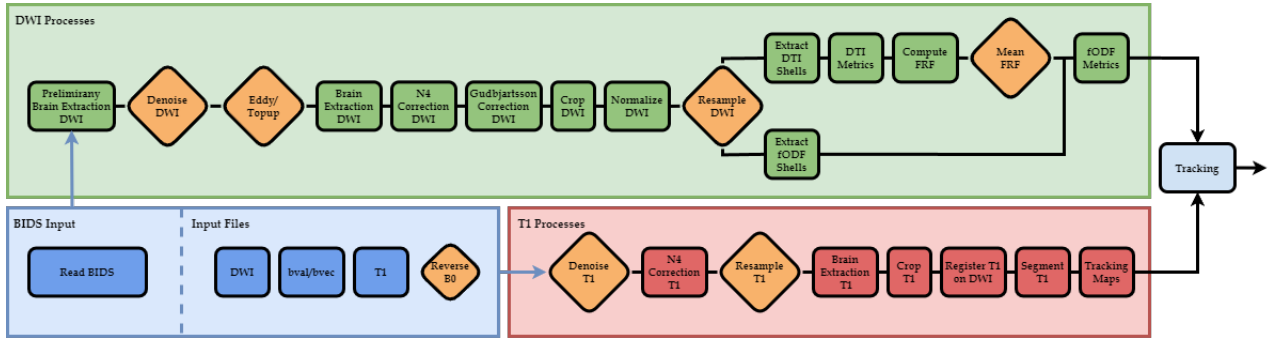


**Figure 3.1:** Processes of the TractoFlow pipeline with the additional Rician bias correction process. The input files (blue square) required to run the pipeline. They can be either in BIDS format or separated files. The DWI processes (green square) that take the DWI, the b-values/b-vectors files and the reversed phase encoded  $b = 0$  image. The T1 processes (red square) that take the T1 weighted image in input. The fiber tracking process (light blue) and all processes or images that are optional (orange diamond).

### 3.1.2 Bundle Extraction

Once Tractoflow reconstructs a complete tractogram, the next step is to perform bundle recognition, where the entire tractogram is decomposed into separate bundles. Tractography streamlines are classified as either belonging to a particular bundle or discarded. For this bundle segmentation, we use the ReconBundlesX flow ([https://github.com/scilus/rbx\\_flow](https://github.com/scilus/rbx_flow)). ReconBundlesX is a tool to separate a wholebrain tractogram into different bundles divided into separate files [115, 116, 117, 118], see Figure . It is multi-atlas and multi-parameter, and more robust to the single atlas and single parameter version of RecoBundles published in DIPY [57] as it has been shown in [115].

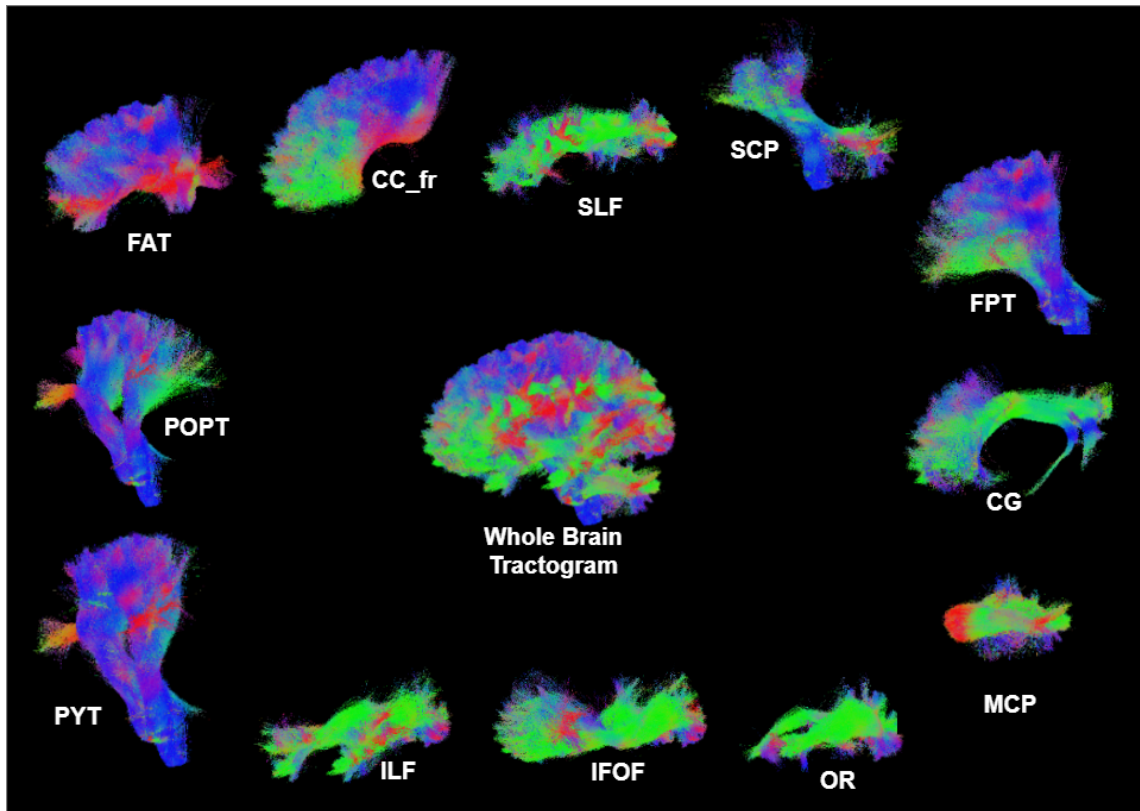


**Figure 3.2:** Illustration of a whole brain tractogram obtained with tractography and separated into the principal bundles with ReconBundlesX. Some of the obtained bundles are shown. For example, the frontal aslant tract (FAT), frontopontine (FPT), corpus callosum frontal (CC\_fr), pyramidal tract (PYT), inferior fronto-occipital fascicle (IFOF), superior longitudinal fasciculus (SLF), superior cerebellar peduncle (SCP), cingulum (CG), middle cerebellar peduncle (MCP), optic radiation (OR), inferior longitudinal fasciculus (ILF) and parieto-occipital pontine (POPT).

### 3.1.3 Local Modeling

In order to recover the local diffusion profiles for tractometry, we have decided to use the MRDS method applied to the MTM for estimating fixel-based dMRI metrics such that: fixel-AD, fixel-RD, and its derivatives fixel-FA and fixel-MD. MRDS estimate a different diffusivity for all fixels in a voxel. MRDS can be informed with a FRF as starting point for a better convergence when estimating the diffusivities. We use a in-house implementation of DTI for estimating the initial diffusivities, considering voxels with a high probability of having a single fixel. But the FRF computed with tractoflow could be used as well.

We have seen in previous chapters that there is a variety of local diffusion models and methods that can be used to represent the dMRI data. Note that we have al-

ready used the CSD method as local model in the tractoflow pipeline. However, that local model is used only for reconstructing the local directions for tractography. MRDS can be used for tractography as it was shown in [53, 54]. However, the model selection in the MRDS method, which is performed using the Bayesian Information Criteria (BIC), tends to overfit the number of orientations per voxel, see Figure 3.3. This leads to a higher number of false positive streamlines compared with CSD [53]. That's why we decided to use CSD for the tractography step of the pipeline.

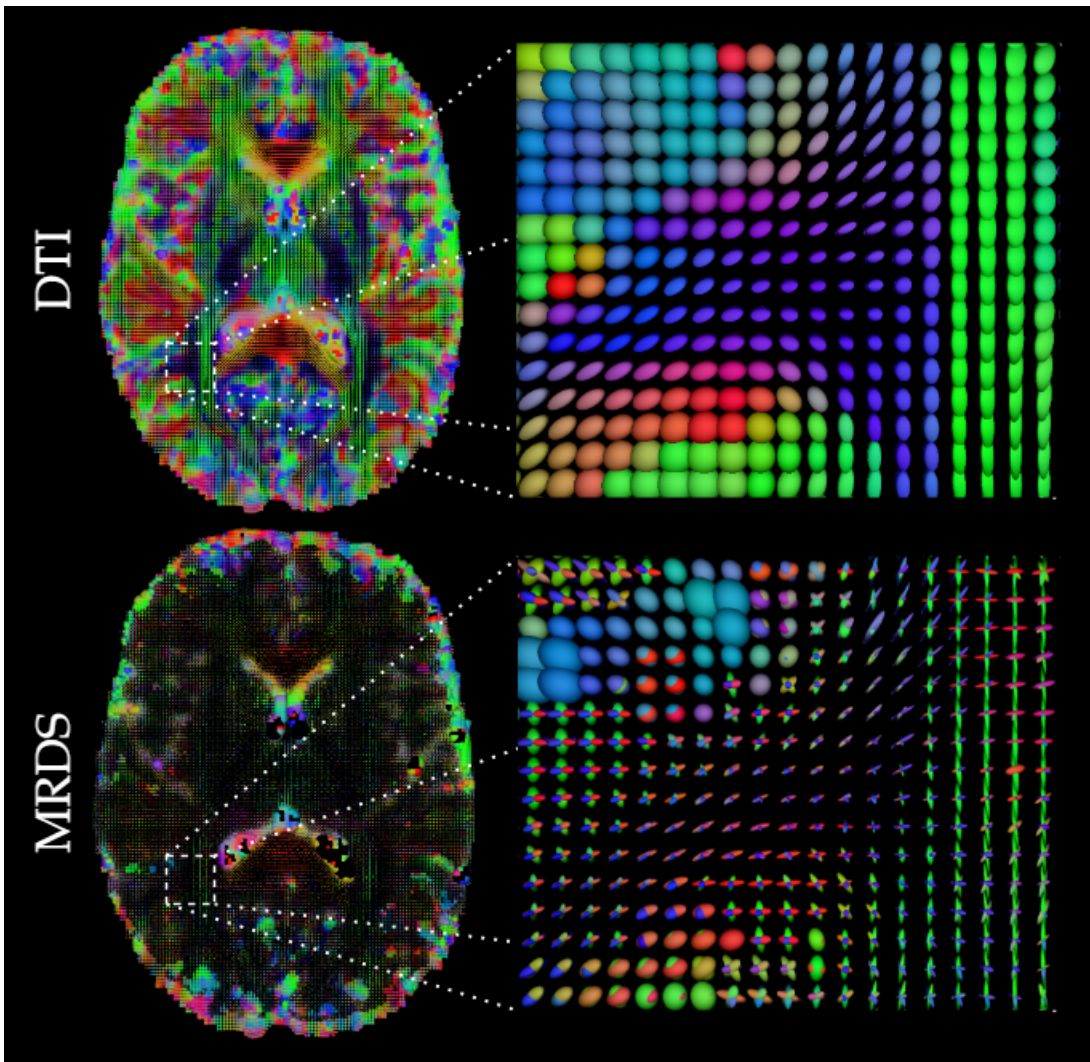


**Figure 3.3:** Axial view of a tensor image and a multi-tensor image fitted with DTI and MRDS, respectively. Comparison between the DTI and MRDS methods illustrate the capability of MRDS to recover different fiber crossing regions. This also illustrate how, in some voxels, MRDS is overfitting the number of tensors.

### 3.1.4 Tractometry

We have decided to integrate the next-flow tractometry\_flow pipeline [128, 129, 130] in our pipeline to extract tract profiles by combining streamline bundles and diffusion MRI metrics. It has shown to be a fast, automatic and reproducible pipeline for tract profiling [128]. Adapting this pipeline to integrate the fixel-based metrics estimated with MRDS could allow us to recover a fixel-specific tract RD profile as well as other dMRI metrics like AD, FA and MD.

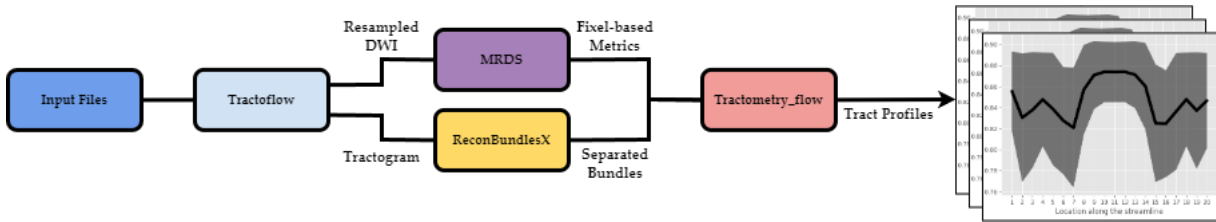


**Figure 3.4:** Processes of the proposed pipeline. Input DWI, bval/bvec and T1 files (blue square). The tractoflow preprocessing and tractography step (light blue square). The Resampled DWI from tractoflow is used as input for the local modeling step (violet square) with MRDS. On the other hand, the RecoBundlesX step (yellow square) takes the output tractogram from tractoflow and splits it into separated bundles. Finally, the fixel-based metrics from MRDS and the separated bundles from ReconBundlesX are combined using tractometry\_flow to compute the tract profile for every metric and bundle combination (pink square).

## 3.2 Data

### 3.2.1 Synthetic Dataset

In order to validate the performance of the proposed method in complex scenarios, we opted for the digital phantom from the ISBI 2012 - HARDI Reconstruction Workshop [25, 26]. This phantom has an structure field with specific arrangements of synthetic fibers that mimic challenging crossing configurations. The structure of the phantom consists of a  $16 \times 16 \times 5$  voxels and 3 fiber bundles with a 3D configuration of tracts, see Figure 3.5. The phantom has been used before to evaluate and compare a large selection of reconstruction algorithms for recovering the local intra-voxel fiber structure from diffusion MRI acquisitions [25].

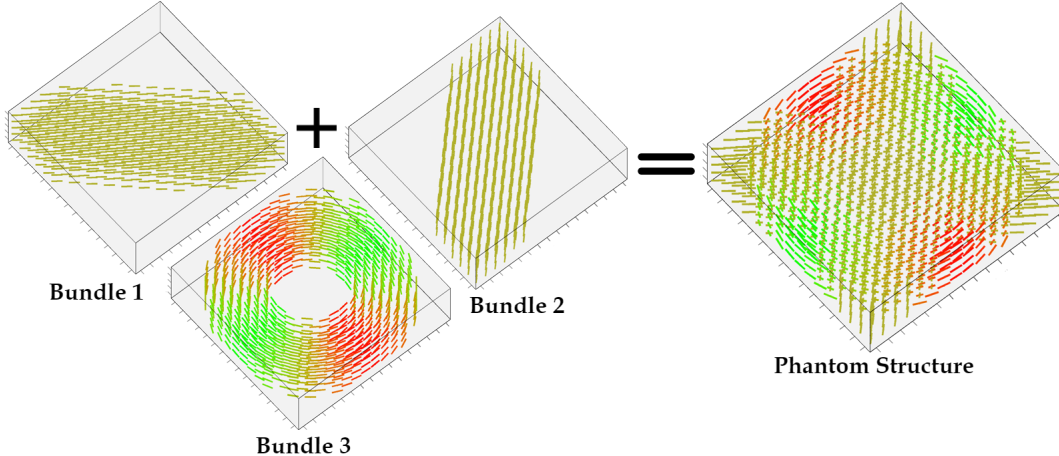


**Figure 3.5:** The structured field of the digital phantom showing the 3 fiber bundles configuration. The directions of the fiber populations are colored depending on their orientation using the color code  $(x, y, z) \rightarrow (r, g, b)$ .

The simulation of the diffusion-weighted signal intensity was numerically simulated in every voxel by adopting the classical Gaussian mixture representation described in Equation 1.11:

$$S(\mathbf{q}) = S_0 \sum_{k=1}^N \alpha_k \exp(-b\mathbf{g}_i^T \mathbf{D}_k \mathbf{g}_i),$$

where  $\mathbf{q} \in \mathbb{Q}^3$  is the vector in q-space corresponding to the DEO  $\mathbf{g}_i \in \mathbb{S}^2$ , b-value  $b$  and diffusion time  $t$  with  $\mathbf{q} = q\mathbf{g}_i = \|\mathbf{q}\| \mathbf{g}_i$  and  $b = 4\pi^2 q^2 t$ . For the DEOs  $\{\mathbf{g}_i\}_{i=1}^n$  and the b-values  $b$  the Penthera3T adquisition protocol [27] was used, which has 3 different shells  $b = 300, 1000, 2000 \text{ mm}^2/\text{s}$  with 8, 32 and 60 directions, respectively, and 7  $b = 0$  for a total of  $n = 107$  directions. Each bundle is determinated by the tensor  $\mathbf{D}_k$ , which is given by Equation 1.15. Assuming axial symmetry, eigenvalues  $\lambda_{k,1}, \lambda_{k,2}$  and  $\lambda_{k,3}$  of  $\mathbf{D}_k$  are the diffusivities along the parallel axis of the main diffusion  $\lambda_k^{\parallel} = \lambda_1$  and the perpendicular axis  $\lambda_k^{\perp} = (\lambda_2 + \lambda_3)/2$ . In the original phantom proposed in the challenge, diffusivities where generated from ranges typically observed in the human brain:  $\lambda_{k,1} \in [1, 2] \times 10^{-3} \text{ mm}^2/\text{s}$  and  $\lambda_{k,2} = \lambda_{k,3} \in [0.1, 0.6] \times 10^{-3} \text{ mm}^2/\text{s}$ . However, we injected lambda values directly estimated from the myelo\_inferno dataset.

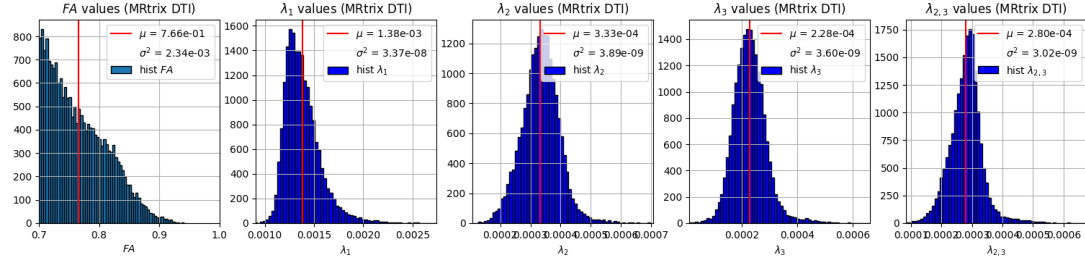


**Figure 3.6:** Histogram of lambda values estimated by fitting the DTI implementation included in MRtrix [58] to the myelo\_inferno dataset. Here  $\lambda^{\parallel} = \lambda_1$  and  $\lambda^{\perp} = \lambda_{2,3} = (\lambda_2 + \lambda_3) / 2$ .

The diffusion properties are constant along the trajectories. The signal  $S$  has been perturbed as in the original phantom by adding Rician noise such that

$$\tilde{S}(\mathbf{q}) = \sqrt{(S(\mathbf{q}) + \eta_1)^2 + \eta_2^2}, \quad (3.2)$$

with  $\eta_1, \eta_2 \sim \mathcal{N}(0, \sigma^2)$  and  $\sigma = S_0/SNR$ . We set the **signal-to-noise ratio (SNR)** to  $SNR = 12$  to simulate challenging levels of noise. In [26] a MATLAB script for simulating the signal was proportioned. However, we made a faster and more flexible re-implementation of this script in Python. Instead of using an iterative approach, we used vectorized operations to speed the simulation. This improvement in performance allowed to include a new feature to add dispersion to the signal. Besides, we modified how the phantom receives the input parameters.

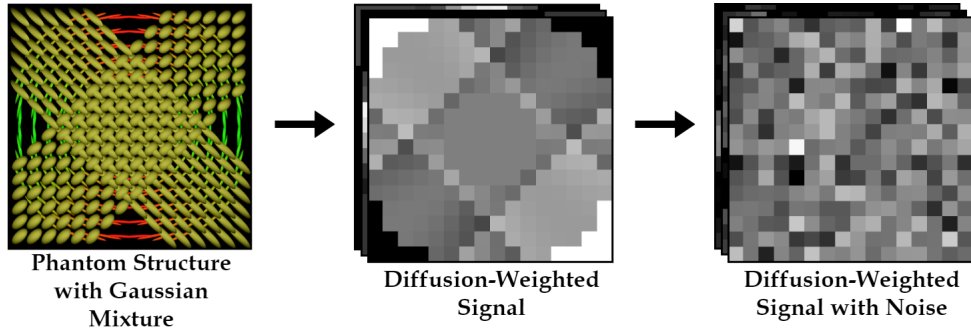


**Figure 3.7:** From phantom structure and Gaussian mixture to diffusion-Weighted signal with noise.

For example, lambda values are loaded from an input Nifti image instead of being hard coded in the script. This enables the possibility to simulate damage in the tracts by altering lambda values with a mask in a specific spot, see Figure 3.8. For the porpuse of this work, we generated two different datasets to simulate two different experimental conditions: healthy and demyelinated fiber tracts.

1. Control phantom subjects: without any damage and with lambda values similar to the control subjects of the myelo\_inferno dataset. These subjects will be “healthy” subjects.
2. MS phantom subjects: with localized “damage” simulating demyelination, i.e. spots in the bundle with increased RD values, and hence lower overall FA and MD values. This is of special interest considering the localized nature of MS lesions.

Both datasets have 26 subjects to match the number of subjects in the myelo\_inferno dataset.

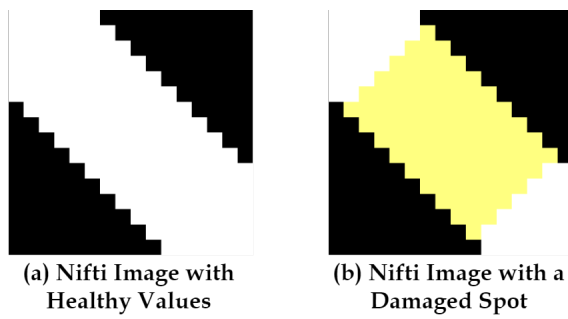


**Figure 3.8:** (a) Nifti image with control values (white) for the diffusivities of the Bundle 1. Values are constant along the bundle. (b) Nifti image for Bundle 1 with damage (yellow) values.

### 3.2.2 Myelo Inferno Dataset

The acquisitions were done by the Sherbrooke onnectivity Imaging Lab (SCIL). The data set includes anatomical, multi-shell diffusion and inhomogeneous magnetization transfer MRI images (3T MRI Philips Healthcare system) collected from 20 healthy adults (mean age 35 years old, standard-deviation 4.7 years old, 4 men and 16 women). Subjects are 75% women and 25% men because, as we said in Chapter 1, MS is  $\sim 3$  times more common on women than men. Subjects were scanned five times over 6 months with a 4-week interval ( $+/- 1$  week) for a total of 120 DWIs. The DWI (112x112 matrix, TR 5615ms, TE 95ms, SENSE factor of 2) were acquired on a 3 Tesla MRI (Philips, Ingenia) with a single-shot echo-planar imaging sequence having 3 different shells,  $b = 300, 1000, 2000 \text{ mm}^2/\text{s}$  with respectively 8, 32 and 60 directions distributed, 7  $b = 0$  for a total of 107 samples and a  $2\text{mm}$  isotropic spatial resolution. A reversed phase encoded  $b = 0$  image is available with the same spatial resolution as the DWI. The T1-weighted MPRAGE image (TR 7.9ms, TE 3.5ms) has a  $1\text{mm}$  isotropic spatial resolution. Each inhomogeneous MT (ihMT) MRI for myelin index reconstruction was acquired using a 3D segmented-EPI gradient-echo sequence with different MT preparation

pulses (TR/TE =  $3.6/112ms$ , 2mm isotropic resolution). IhMT uses a magnetization preparation (10 Hann pulses of  $0.9ms$  duration with  $1.5ms$  interval at a frequency offset of  $+/- 7000Hz$ ) to increase specificity to myelin.

# Chapter 4

## Results

### 4.1 Previous Results

In this section we will brief description of the previous results already published in abstracts. For a more detailed explanation, we included each abstract in the Appendix chapter. These results have been the starting point of this work.

#### 4.1.1 Robust Estimation of Fixed-FA on Fiber Crossing

In this abstract, we proposed a multi-shell pipeline based on MRDS to estimate the fixel-FA [52]. It was shown that this method is accurate and robust to noise in synthetic phantoms, and in the centrum semiovale of the human brain with clinical multi-shell data sets. This method does not involve tractography, but instead it uses the local model to recover the different bundles clustering tensors with a similarity function. The pipeline is similar to the one described in Figure 4.10 of previous chapter, see Figure 4.1.

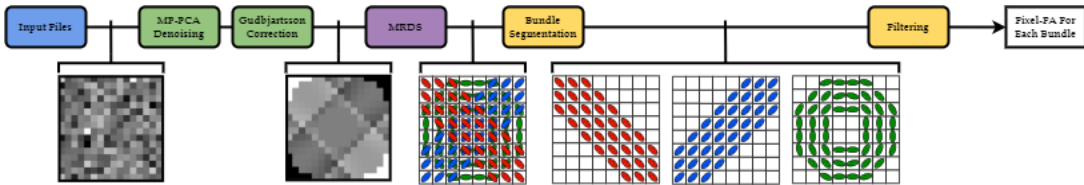


Figure 4.1: Proposed pipeline to estimate fixel-FA for each bundle.

The bundle segmentation step uses the dissimilarity measure described in [152], which defines a distance function between two tensor  $\mathbf{D}$  and  $\mathbf{T}$  such that

$$d(\mathbf{D}, \mathbf{T}) = \frac{\|p(\mathbf{D}) - p(\mathbf{T})\|}{d_0^2} + \frac{\angle(\mathbf{D}, \mathbf{T})}{\theta_0} + \frac{|fa(\mathbf{D}) - fa(\mathbf{T})|}{f_0} + \frac{|md(\mathbf{D}) - md(\mathbf{T})|}{m_0}, \quad (4.1)$$

where defined  $d_0$ ,  $\theta_0$ ,  $f_0$  and  $m_0$  are constants,  $p(\mathbf{D})$  is the voxel position of the tensor  $\mathbf{D}$ ,  $\angle(\mathbf{D}, \mathbf{T})$  is the angle between the PDDs of the tensors  $\mathbf{D}$  and  $\mathbf{T}$ , and  $fa(\mathbf{D})$  and  $md(\mathbf{D})$  are the FA and MD values of the tensor  $\mathbf{D}$ , respectively. Then, a similarity function is defined as following:

$$s(\mathbf{D}, \mathbf{T}) = \exp(-d(\mathbf{D}, \mathbf{T})). \quad (4.2)$$

The segmentation of the bundles is performed using a flood-fill based algorithm. Given an random initial tensor, the algorithm starts the bundle in the voxel containing that tensor. Then, it looks for all the tensors in the neighboring voxels. If a neighbor voxel contains a tensor  $\mathbf{T}$  such that  $s(\mathbf{D}, \mathbf{T}) > c$ , for some fixed threshold  $c$ , the algorithm extends the bundle to that voxel. After that, the process is recursively repeated for the new voxels in the bundle, see Figure ???. Finally, a filtering step is used to enhance the overall FA values of each bundle by using the information obtained in the segmentation stage. Given the separated bundles, the FA values of every tensor is averaged with the FA value of its tensor neighbors within the same bundle. This filtering step is helpful to remove the dispersion when estimating the FA value for each tensor by keeping the local spatial properties. This pipeline was tested on the digital phantom introduced in the previous chapter. We set the FA values different for each bundle. For bundle 1,  $FA \sim 0.8$  with a damaged spot where  $FA \sim 0.6$  simulating a localized damaged in the bundle. For bundle 2,  $FA \sim 0.85$  simulating a healthy bundle and, for bundle 3,  $FA \sim 0.6$  simulating a completely damaged bundle. Finally, Rician noise with  $SNR = 12$  was added using Equation 3.2. For the in-vivo data set, we used one of the control subjects of the myelo\_inferno data set and the centrum semiovale as ROI.

The obtained segmentation is visually correct, see Figure 4.2. Moreover, it can be observed in Figure 4.3 that the pipeline allows for an accurate estimation of the fixel-FA profile in both synthetic and in-vivo dMRI data. From Figure 4.3 it is easy to identify which bundle is healthy, partially damaged or globally damaged. The pipeline is robust to fiber crossing and high level of noise. However, this pipeline requires to manually tune a large number of parameters ( $d_0$ ,  $\theta_0$ ,  $f_0$ ,  $m_0$  and  $c$ ). Altogether, this pipeline showed that MRDS has potential to be combined with more sophisticated methods for fiber tracking like tractography. Thereby making it well suited to the goal of automatically estimating fiber tract profiles by using tractometry.

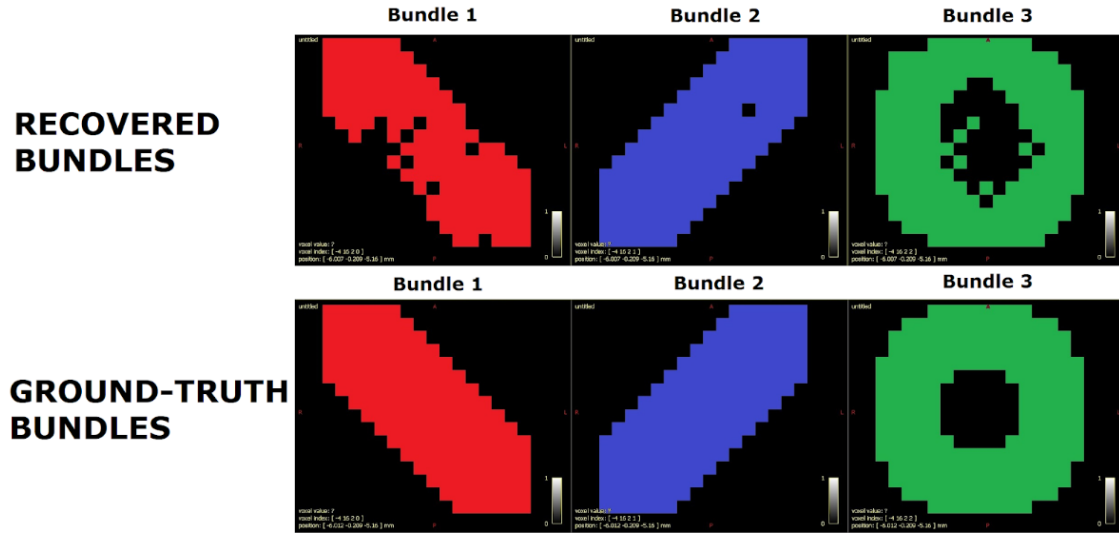


**Figure 4.2:** (up) Segmentation obtained after the segmentation stage of the pipeline. Each recovered fiber bundle is colored with a different color to identify each bundle. The color of each fiber bundle is consistent with the colors shown in all the other figures. (down) Ground-truth fiber bundles.

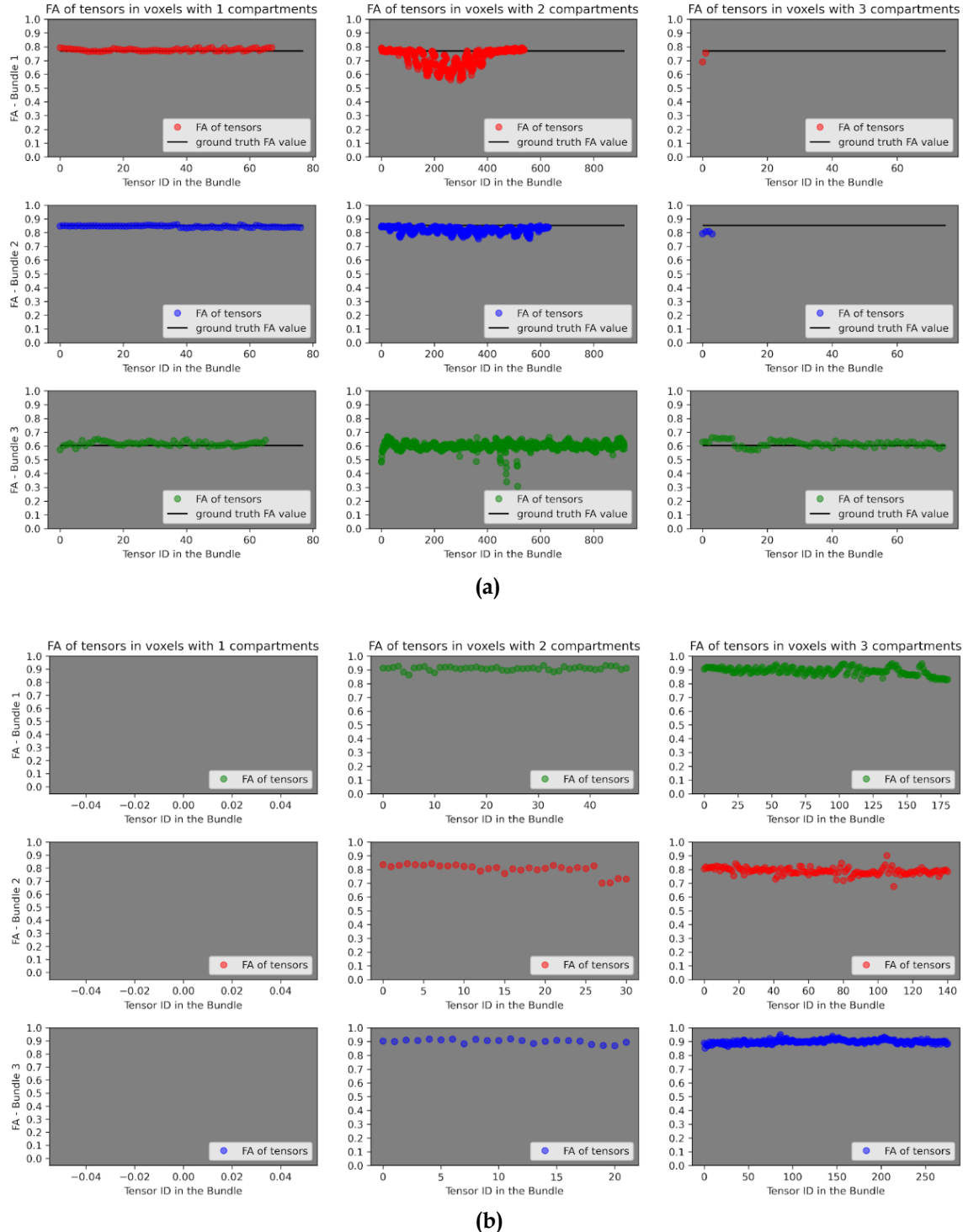


**Figure 4.3:** FA values along each bundle results (a) for synthetic data and (b) for the centrum semiovale in the in-vivo data. Each row represents the FA values for a different bundle. Each column represents, respectively, FA values in voxels with 1, 2 and 3 tensors (i.e., FA values in each bundle are shown separated depending on the number of tensors per voxel). For comparison, the ground-truth FA value for each bundle was added as a black horizontal line.

### 4.1.2 Tractography from Gaussian Multi-Facicle ODFs

In this abstract, we proposed a pipeline based on MRDS to compute the structural connectome from dMRI data. The effectiveness of the pipeline was shown in the DiSCo challenge digital phantom data set [54].

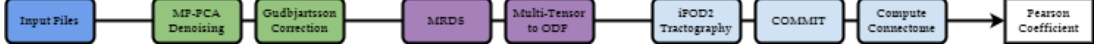


**Figure 4.4:** Proposed pipeline for the DiSCo challenge.

We showed that ODFs extracted from a multi-tensor field can be used for tractography. A multi-tensor image can be converted to an ODF image using the following formula [153]:

$$ODF(n) = \sum_i^N \alpha_i \frac{(n^T \mathbf{D}_i^{-1} n)^{-3/2}}{4\pi \sqrt{\det(\mathbf{D}_i)}}, \quad (4.3)$$

where  $\mathbf{D}_i$  and  $\alpha_i$  are the diffusion tensor and its compartment size associated to the  $i$ -th fixel. This tractography pipeline provides competitive prediction of the connectivity on state-of-the-art synthetically generated phantoms [54].

This abstract evidenced that the multi-tensor fields fitted by MRDS can adapted to be included in a standard tractography technique. That's why it marked an important previous results for our current work because it could replace, for our pipeline, the CSD as local modeling in Tractoflow. However, the current state of the model selector in MRDS prevents to use MRDS as it causes plenty of false positive streamlines. But it opened the question to improve the model selector in MRDS.

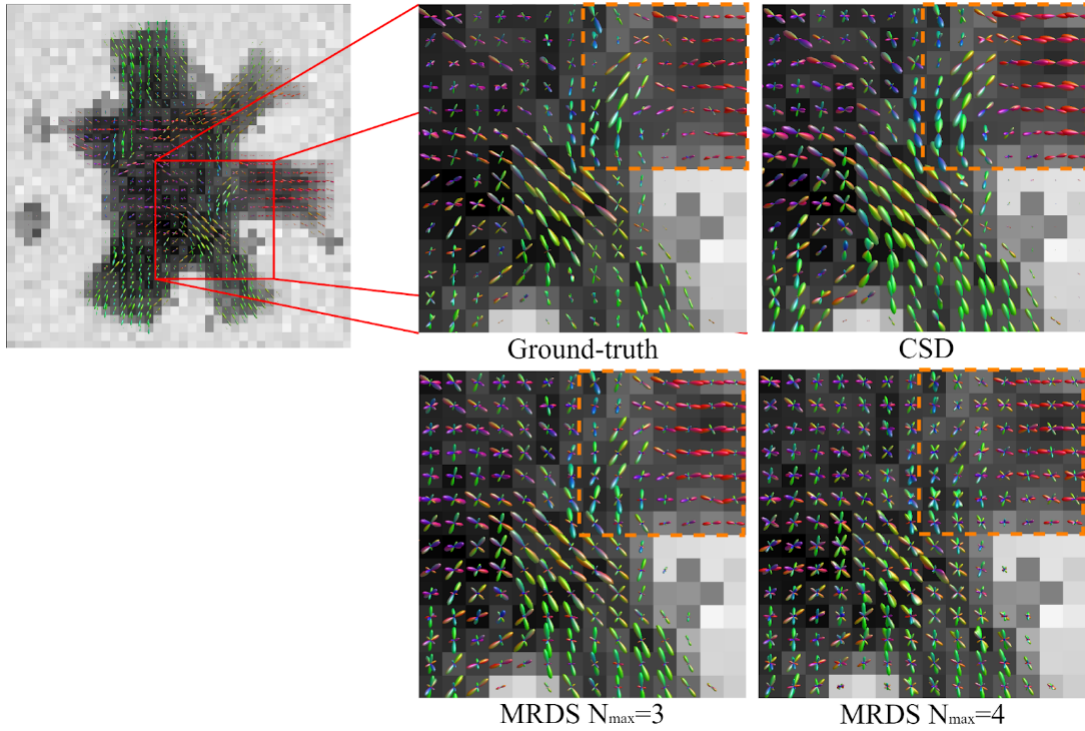


**Figure 4.5:** Visualization of the GT and reconstructed dODFs of the training dataset of the DiSCo challenge.  $N_{max}$  represents the maximum number of fixels in each voxel, which is determined by the selector model BIC [11]. Both CSD and MRDS are able to recover most of the orientations. However, MRDS can recover orientations presented in the GT that are not recovered by CSD as it is highlighted with a dashed orange square.

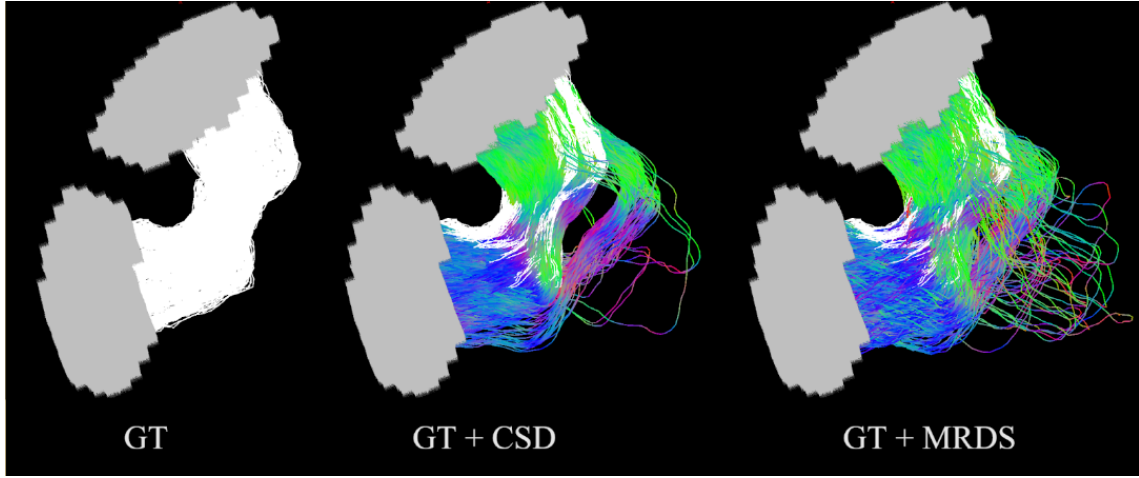


**Figure 4.6:** Visual comparison of the streamlines connecting 2 ROIs (grey colored). The leftmost tractogram represents the GT strands trajectories (white colored). The one in the middle is the overlapped GT and CSD tractograms. The rightmost represents the overlapped GT and MRDS tractograms. This experiment shows the higher account of false positive connections in the MRDS tractogram as well as the better overlapping with the GT.

#### 4.1.3 Real-Time Rendering of Massive Multi-Tensor Fields Using Modern OpenGL

In this abstract, we proposed an open-source and novel DTI and MTM data visualizer [55] based on modern OpenGL C++ to give users a more modernized and relevant view of multi-tensor fields. Our approach is interactive, fast when rendering massive multi-tensor fields and tries to achieve many of the constraints of the current available tensor image visualizers in the state-of-the-art.

The visualizer is implemented as a new set of GPU shaders for the **dmri-explorer** [56], a real-time glyphs viewer described in [56]. Shaders use the tensor matrix to deform and color sphere glyphs on the GPU to get diffusion tensor glyphs for DTI. It supports MTM glyphs as layers of standard DTI glyphs, see Figures 4.8 and 4.9. Tensors can be colored using either the Principal Diffusion Direction (PDD) of the tensor as well as the FA, MD, AD and RD values using popular color maps, see Figure 4.7. Since the viewer is an extension of the dmri-explorer, it inherits all the features allowing fast real-time slicing of the multi-tensor field as well as the capability to scale, zoom in and out. Rendering performance calculated with frame per second (FPS) using an Intel Core i7 7700HQ and Nvidia GTX 1070 is ~1,300 FPS (1,204 tensors and 772,968 vertices) on the synthetic phantom, while with the Penthera dataset performance is ~ 55 FPS (45,375 tensors and 29,130,750 vertices).

Although there are plenty of DTI visualization software available, most of them do not have or have a limited support for MTM data. Overall, our viewer has shown to give high framerate when rendering massive MTM fields fitted to real human brain datasets. High performance is consistent even using aged portable hardware. Our visualizer keeps the previous features presented in the original dmri-explorer, and combines them with some new ones like PDD or FA coloring for the multi-tensor glyphs. This is relevant for our current work because tensors encode complex diffusion information precisely. Therefore, the interpretation of a tensor or multi-tensor fields is challenging. Visualization of DTI and MTM data provides an intuitive understanding of this type of data, which results beneficial for any study involving DTI or MTM data. Visualization is essential for quality assessment of tensor or multi-tensor fit on new datasets, and for studying the behavior of a reconstruction methodology in development.

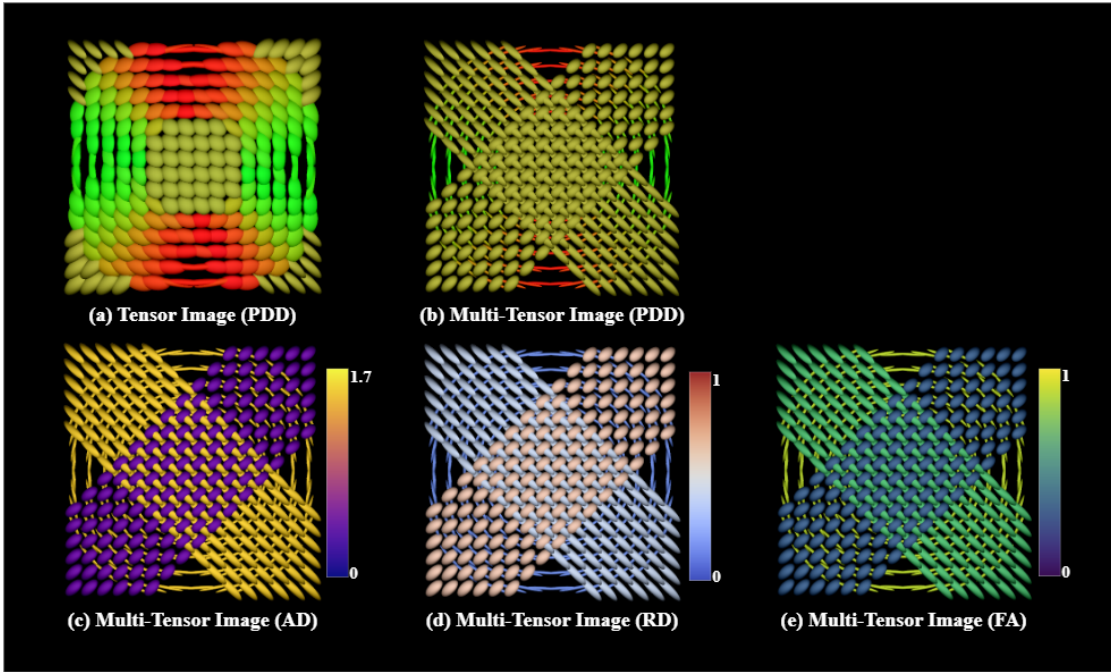


**Figure 4.7:** Multi-tensor field fitted to the synthetic phantom [25, 26] is showed in different coloring modes. (a) Single tensor glyphs colored using the PDD of the tensor similar to the MRtrix viewer. (b) Same as (a) but using multi-tensor glyphs. (c,d,e) Multi-tensor glyphs colored using the AD, RD, and FA values of the tensor with the Viridis, Plasma and Cool Smooth Warm color maps, respectively.

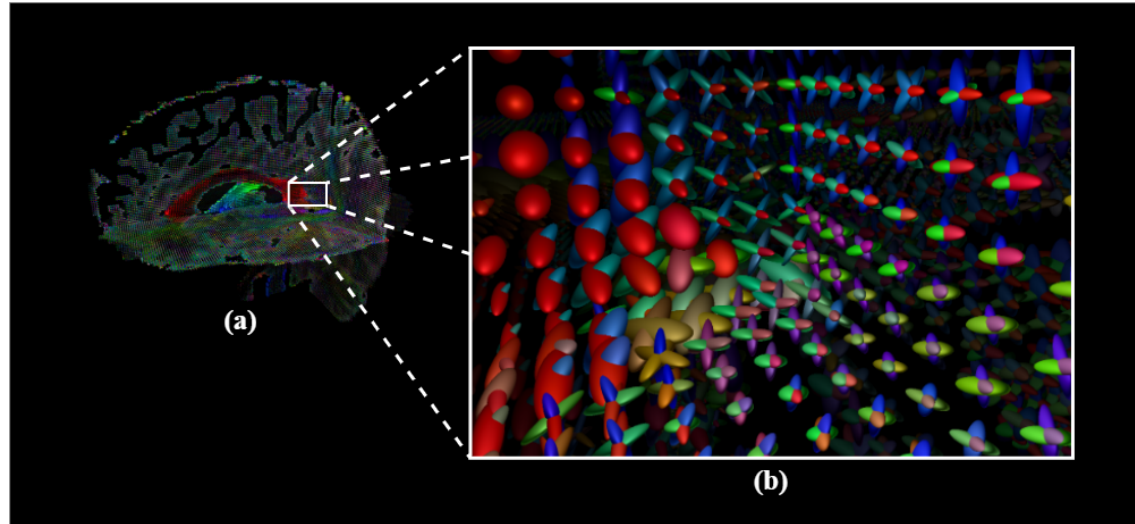


**Figure 4.8:** The multi-tensor field fitted to a control healthy subject of the myelo\_inferno dataset. (a) 3D render of the multi-tensor field colored by the PDD. (b) The viewer is interactive, so it allows rotating, translating, zooming in and out.

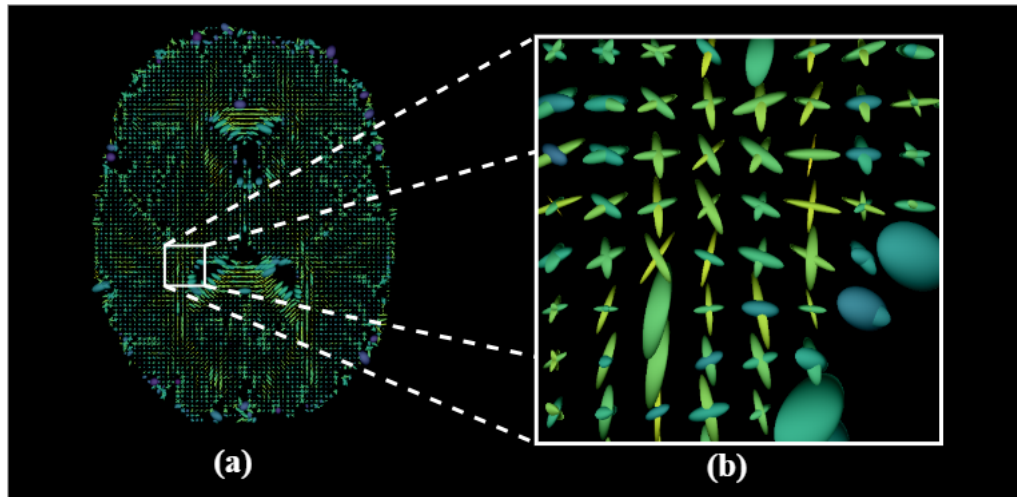


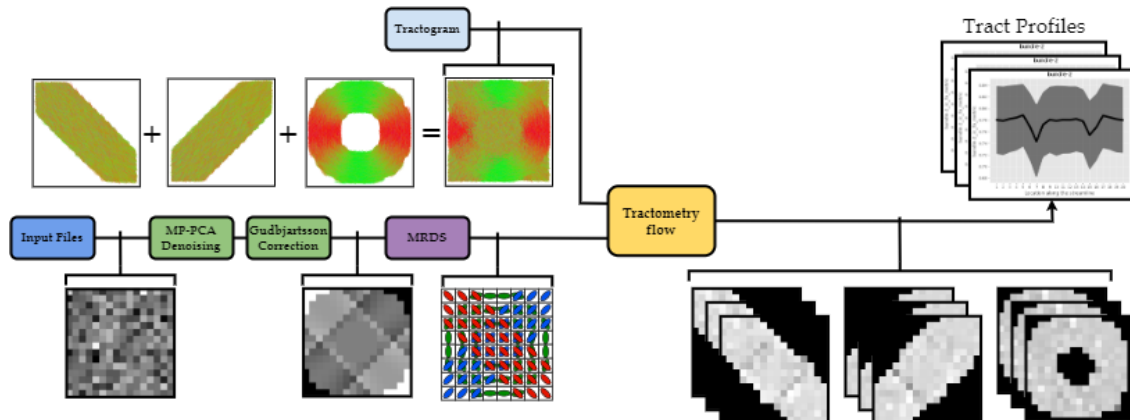
**Figure 4.9:** In addition to 3D slide rendering, it is shown how the viewer is able to render slides in 2D mode for Sagittal, Axial and Coronal views. (a) Axial view of the 3D render illustrated in Fig. 2. (b) Zoom-in of the slide to easily explore details.

## 4.2 Preliminary Results

### 4.2.1 Tractometry Pipeline Experiments

#### 4.2.1.1 Experiments on Synthetic Phantoms

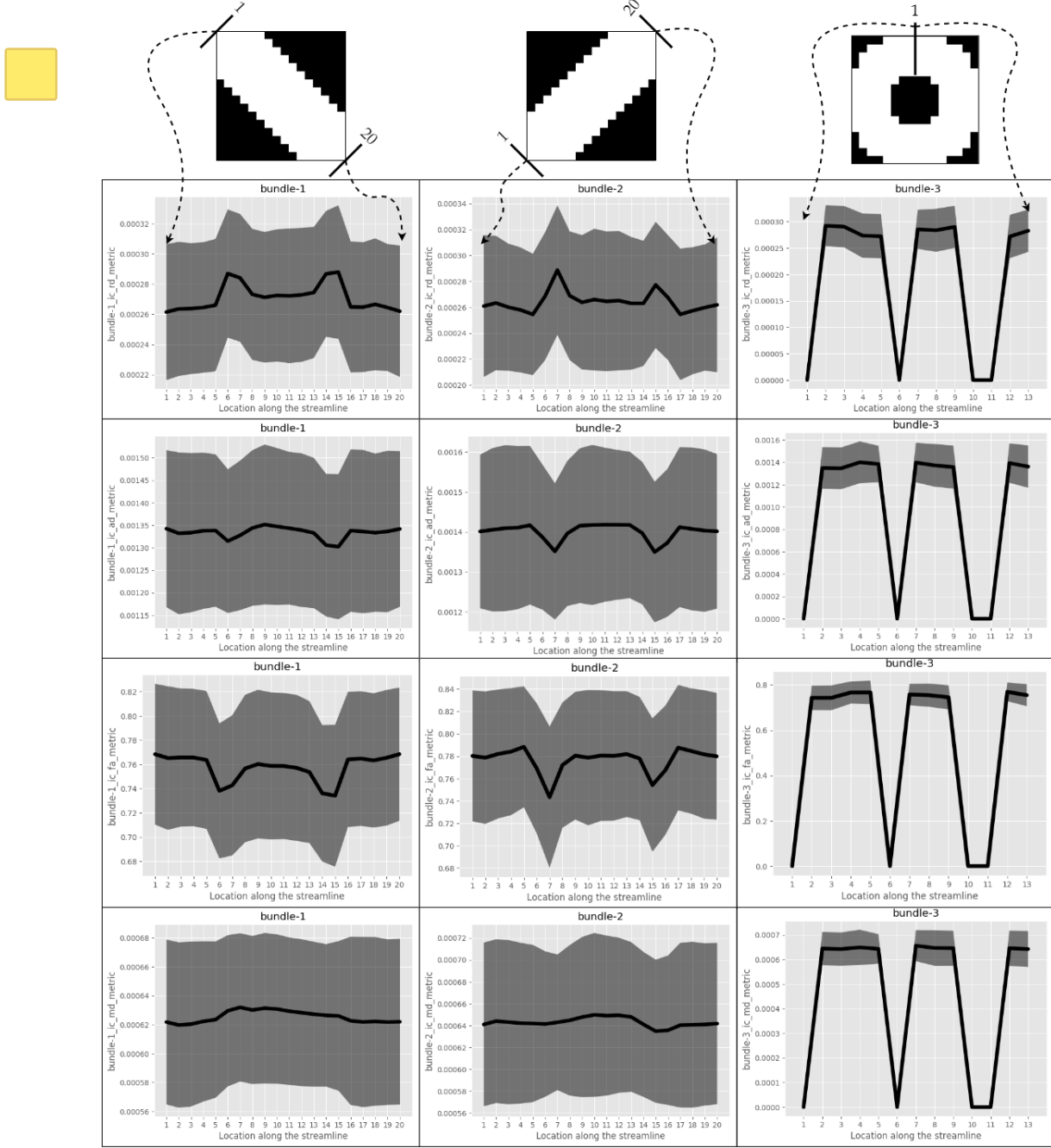
This section shows the results of the pipeline in Figure 4.10, which was proposed to process the phantom and validate our tractometry pipeline. Note that in Figure 4.10 we excluded a tractography process. In this way, we focus on results arising from the capability of MRDS to estimate the fixel-based dMRI metrics. In other words, we will study the results of the tractometry pipeline assuming that we have a GT tractogram without false positives. Thus, we remove any bias induced by false positives to see the best possible scenario for the pipeline in terms of the fixel-based metrics estimation.



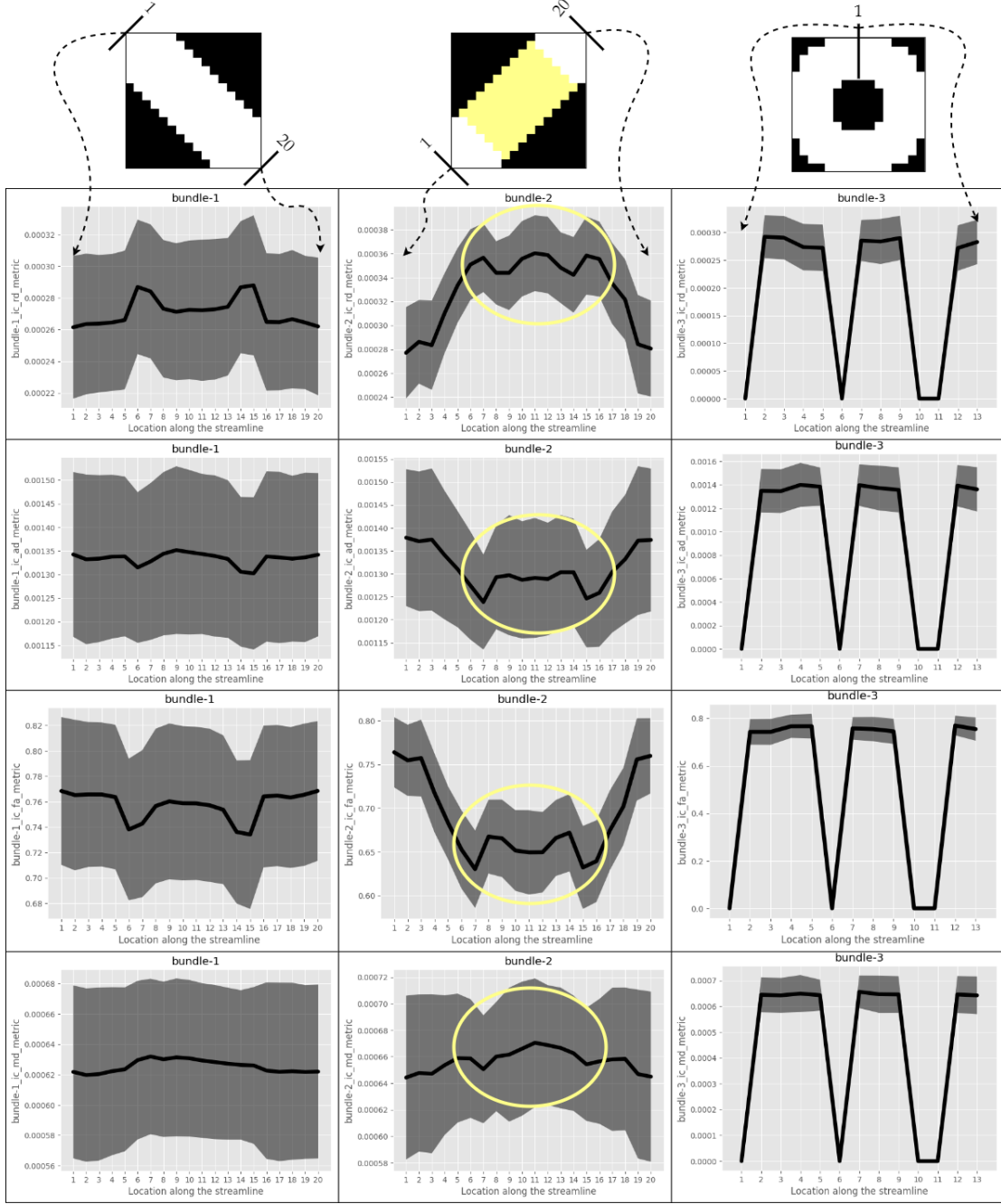
**Figure 4.10:** Pipeline adapted from 4.1 to process the phantom and validate the pipeline in Figure 3.4.

Figure 4.11 shows the tract profiles for the 26 healthy control phantoms over the 3 bundles. Estimated metrics correspond to the GT metrics of the phantom as we showed in Figure 3.6. One has to keep in mind that level of noise used in the injected DWI is  $SNR = 12$ . Hence, our results suggest that our pipeline is robust to significant level of noise variations. After having validated our pipeline on the control data set, we applied the pipeline to the damaged phantom data set on the 3 synthetic fascicles, where phantoms have a damaged spot around the crossing of the bundle 1 and 2 as shown in Figure 4.8. Examination of Figure 4.12 demonstrates that the pipeline effectively identifies decreases in AD and FA, and increases in RD and MD. Those changes in RD values correspond to the location of the simulated demyelination of the bundle 2. In terms of per bundle statistics, we also note from Figure 4.11 and 4.12 that results for healthy bundles show similar results. This gives indications that MRDS is robust against the fiber crossing. Both Figure 4.11 and 4.12 have several aggressive valleys in the tract profiles, which is

consequence of the unrealistic shape of the bundle 3. As we explained in the last chapter, tratometry\_flow computes the centroid of all the input bundles. However, the circular shape of the bundle results, for locations along the streamline, in a null centroid. This should not be a problem in in-vivo data as there are not tracts with circular shape in the human brain. In summary, the results are promising on synthetic data, with the pipeline identifying anomalies in concordance with the damage in the bundles while being accurate and robust to noise.



**Figure 4.11:** Tract profiles obtained from the control phantom applying the tractometry pipeline of Figure 4.10, which combines the GT bundles with the pixel-based metrics estimated by MRDS. Each row represents the tract profiles of each pixel-based metric (pixel-RD, pixel-AD, pixel-FA and pixel-MD). Each column represents the tract profiles for a different bundle. Note that the location 1 and location 13 of the bundle 3 are the same as the bundle is a circle.



**Figure 4.12:** Tract profiles obtained with the tractometry pipeline of Figure 4.10, which combines the GT bundles with the pixel-based metrics estimated by MRDS. Each row represents the tract profiles of each pixel-based metric (pixel-RD, pixel-AD, pixel-FA and pixel-MD). Each column represents the tract profiles for a different bundle. The simulated damaged in bundle 2 is highlighted in yellow. Note that the location 1 and location 13 of the bundle 3 are the same as the bundle is a circle.

#### 4.2.1.2 Experiments on Control In-Vivo Subjects

We tested our proposed pipeline from Figure 3.4 with 24 of the 26 control healthy subjects of the myelo\_inferno dataset. Two of the subjects were discarded due to problems during the acquisition. For the sake of keeping a sort results report, we compared the variation of fixel-specific and usual RD and FA metrics along the tracts CC\_Fr, FAT, FPTT, IFOF and PYT. These tracts were chosen to test the effectiveness of the pipeline to deal with a variety of different tracts, including short and long tracts, with contrasting curvatures and covering diverse zones of the brain.

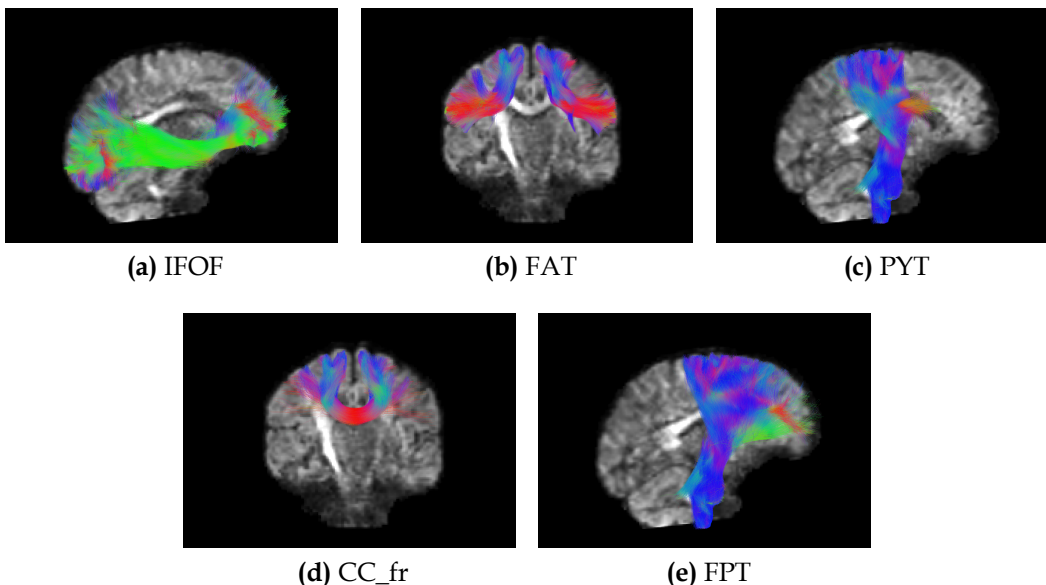


**Figure 4.13:** Comparison of the different tracts selected to test the pipeline. The DWI was added as anatomical reference for the tracts. All tracts are composed of two left and right sub-tracts; except for the CC\_fr, which is composed of CC\_fr\_1 and CC\_fr\_2. In (a,c,d,e) the sub-tracts are not visible to keep a good view of the general tract, in (b) it is possible to see the two parts of the tract.

For this preliminary experiments, the first and third columns of Figure 4.14 and 4.15 illustrate the tract fixel-RD and fixel-FA profiles along the tracts, while the second and fourth columns show the tract profiles for RD and FA. Each row of Figure 4.14 and 4.15 represent the tract profiles for a different tract. When comparing the tract RD profiles from Figure 4.14 with the corresponding tract profiles obtained using fixel-RD, we can observe that they have very similar shapes (except for the PYT\_L and IFOF\_R tracts). However, the standard tract RD profiles tends to have higher RD values compared to their fixel-specific counterpart, which could be a consequence of the fact that DTI gives plate tensors in voxels with fiber crossings. Analogous to Figure 4.14, in Figure 4.15 it can be appreciated that voxel-wise tract

FA profiles are similar in shape to tract fixel-FA profiles. But in the case of the fixel-specific tract profiles the FA values correspond with typical values in healthy WM. This is because standard tract FA profiles are biased by fiber crossing, where FA values decrease. This is an indicative that the pipeline is robust to fiber crossing while being consistent to previous reported FA values of healthy control WM. One may think that if both tract profiles for FA and fixel-FA are similar in shape, this implies that fixel-FA is still suffering from the fiber crossing because it has the same peaks and valleys. However, as it was mentioned in [125], FA increments and decrements along the tracts are not only consequence of fiber crossing, but also from other factor like intermixing with neighboring gray matter or regions of thicker WM where there is less partial voluming. This suggests that fixel-FA remains sensitive as FA, but with the capability to be specific to damages.

### **4.2.1.3 Expected Results**

In general, it can be said that given the strong anatomical priors injected in the segmentation of WM fascicles, test-retest is critical to asses the specificity and reproducibility of the extracted tracts [128]. Further exploration of the test-retest data set, i.e. testing the pipeline in the different subjects including all timepoints, is needed to investigate the repeatability of the tract profiles. Finally, the pipeline should produce consistent results across subjects in the test-retest procedure because the pipeline is based mostly in tractoflow and tractometry\_flow, which have shown to be reliable in clinical assessment.

A follow-up study investigating the application of the pipeline to relapsing remitting MS could prove our hypothesis that this pipeline is useful in MS. For this, we will apply the pipeline to the relapsing remitting MS subjects of the myelo\_inferno dataset. With the preliminary results in mind, we expect that the tract profiles in MS to detect WM changes consistent with location of the demyelination in the brain. Most of all, we envision that this crossing fiber robustness will allow the fixel-RD to provide a better damage detection compared with traditional RD. This would address the current problem in dMRI tractometry of RD being inconsistent and having insufficient evidence to be favorable as a sensitive and specific biomarker for demyelination.

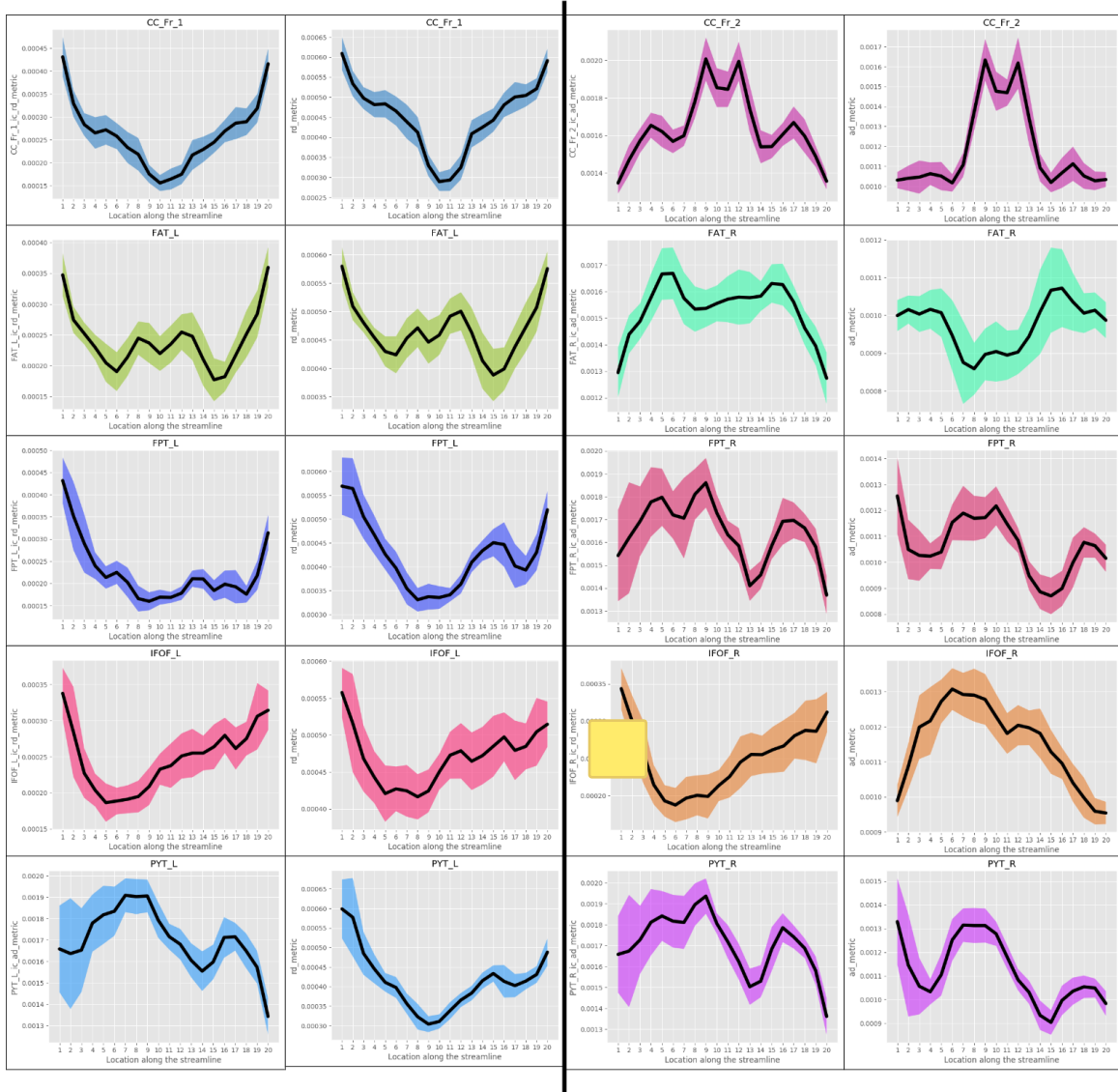


**Figure 4.14:** Tract RD profiles for 24 subjects of the myelo\_inferno dataset in 5 tracts. In the first two columns, images show the tract fixel-RD profile obtained from the estimated fixel-RD of MRDS, while in the third and fourth columns images show the RD metric obtained with typical the RD metric of DTI.



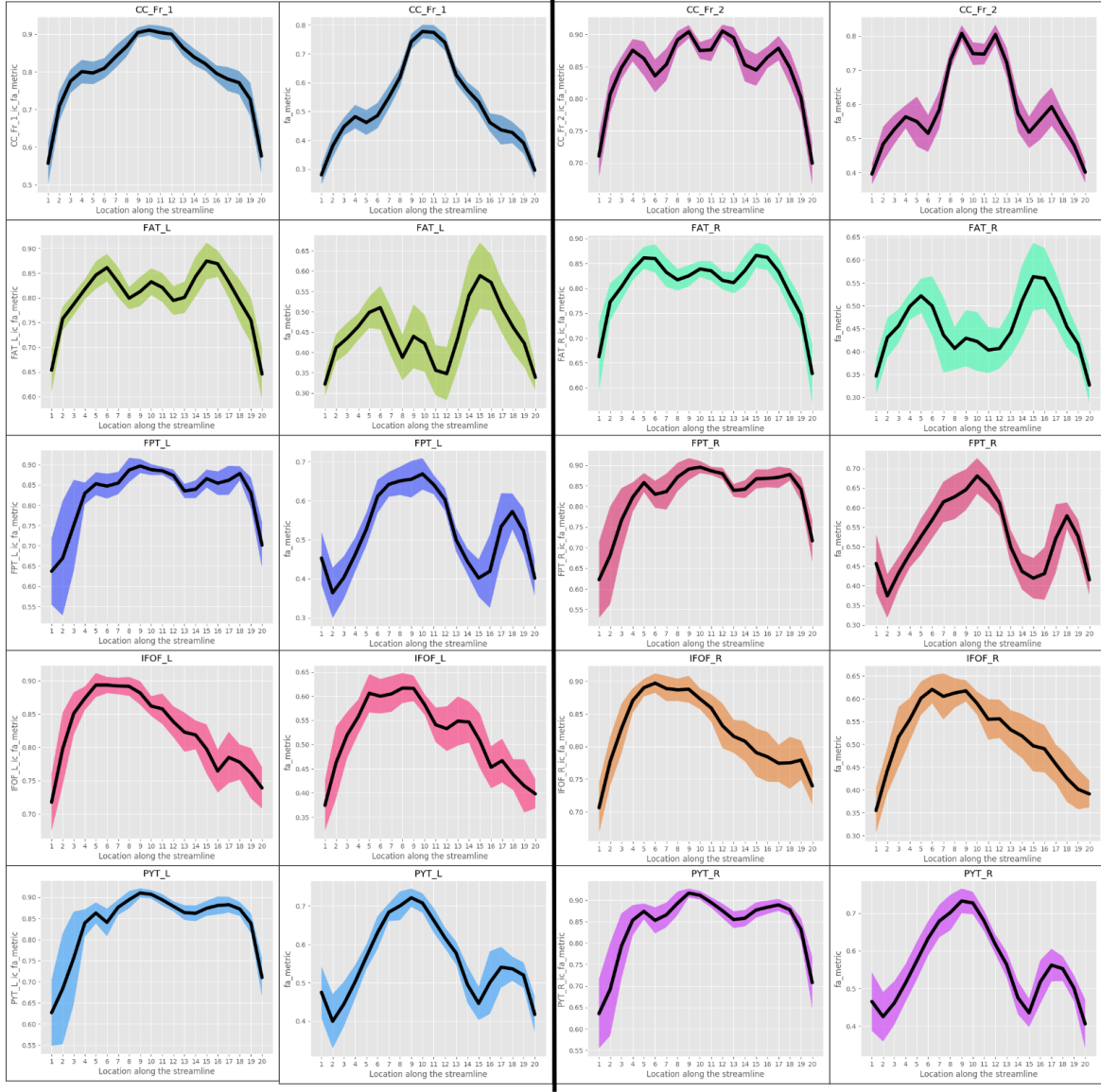


**Figure 4.15:** Tract FA profiles for 24 subjects of the myelo\_inferno dataset in 5 tracts. In the first two columns, images show the tract fixel-FA profile obtained from the estimated fixel-FA of MRDS, while in the third and fourth columns images show the tract FA profile obtained with typical the FA metric of DTI.

## 4.2.2 Improvements of MRDS

### 4.2.2.1 Parallelization of MRDS

We are planning to accelerate the fitting of the MRDS method to the dMRI data by using modern parallel computing techniques. The Algorithm 4.1 shows a preliminary approach to abroad this problem.

---

**Algorithm 4.1** Algorithm in parallel fit the MRDS model.

---

**Require:** Normalized DWI  $E$  and initial diffusion parameters  $\xi_0$

**Ensure:** for every voxel  $N_{opt}$ ,  $\{\theta_k\}_{k=1}^{N_{opt}}$ ,  $\{\alpha_k\}_{k=1}^{N_{opt}}$  and  $\{\xi_k\}_{k=1}^{N_{opt}}$

```

1: for in parallel for every voxel  $v = (x, y, z)$  do
2:   while not convergence do
3:     for N=1,2,3 do
4:        $\xi_k = \xi_0 \quad \forall k$ 
5:       Estimate  $\{\theta_k\}_{k=1}^N$  and  $\{\alpha_k\}_{k=1}^N$  for fixed  $\{\xi_k\}_{k=1}^N$ 
6:       Estimate  $\{\xi_k\}_{k=1}^N$  for fixed  $\{\theta_k\}_{k=1}^N$  and  $\{\alpha_k\}_{k=1}^N$ 
7:     end for
8:   end while
9:    $N_{opt} = modsel(\{\theta_k\}_{k=1}^N, \{\alpha_k\}_{k=1}^N, \{\xi_k\}_{k=1}^N)$ 
10: end for

```

---

Algorithm 4.1 is a direct translation of the OpenMP algorithm given in [10]. Of course, this is a first approach for the parallelization of MRDS in the GPU. We will use the Nvidia CUDA toolkit [12] that provides a modern programming language, which allows developers to use the Nvidia CUDA Cores in the Nvidia GPUs for parallel computing. Every voxel computation in Algorithm 4.1 will be assigned to a single CUDA thread as every CUDA thread is executed in parallel in the GPU, see Figure . We still have to implement it on GPU language and test the performance. We have the hypothesis that this naive approach could improve the performance of the fitting process. However, there are several other aspects of the algorithm that have to be considered during the implementation. For example, in order to efficiently use the CUDA threads, all threads in the GPU should perform the same instruction at the same time. Nonetheless, as every CUDA thread will manage a single voxel, it will happen that some voxels will converge before others, decreasing the performance because some threads will have to wait for others to finish. Thus, Algorithm 4.1 is still a naive approach, and we will have to address this and others bottlenecks.

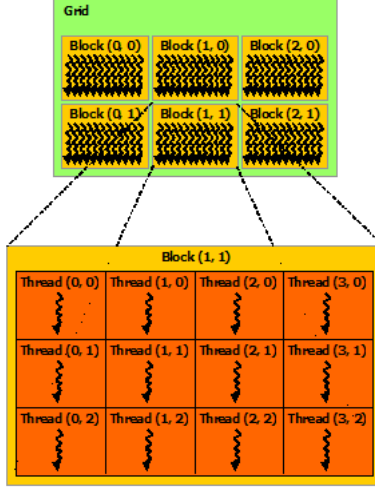


**Figure 4.16:** Illustration of how the threads are structured in a Nvidia GPU. CUDA threads are grouped in CUDA blocks that are executed in parallel. A CUDA block finishes its computation when all threads belonging to that same CUDA block finish every instruction.

#### 4.2.2.2 Model Selector of MRDS

Another aspect that can be improved in MRDS is the model selector. For this, it is possible to inform the model selector of MRDS with the Number of Fiber Orientation (NuFO) map computed in the local modeling step of tractoflow, which is an index of local water matter complexity that is estimated from the number of local maxima of the fODF profile in each voxel [114].

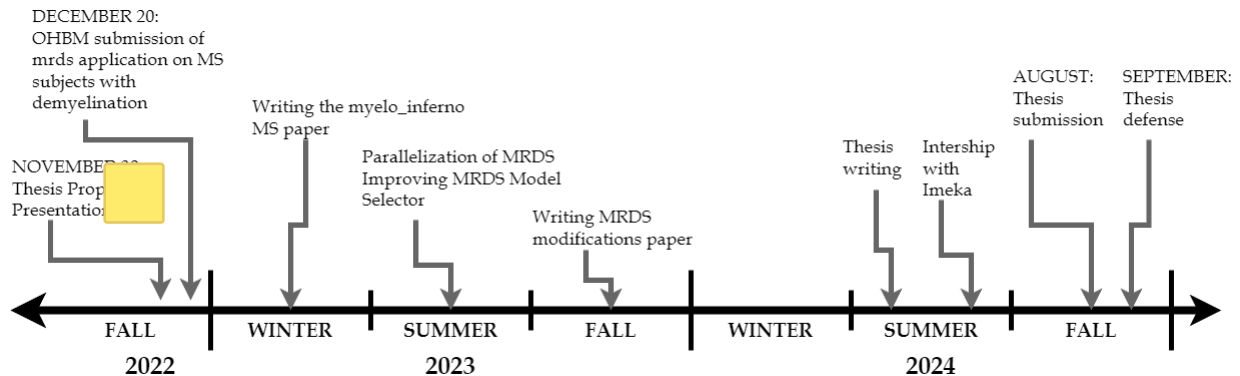
#### 4.2.2.3 Expected Results

We predict that the naive implementation of the parallelization of MRDS will achieve a speed-up of at least 1 order of magnitude. On the other hand, we expect that the use of NuFO maps will reduce the data overfitting by MRDS. Anyway, in the future more ideas will be explored in this part.

# Chapter 5

## Research Activities

### 5.1 Expected Schedule



### 5.2 Conference Abstracts & Journal Publications

- Robust Estimation of Fascicle-based Fractional Anisotropy on Fiber Crossings [52].
- Tractography from Gaussian multi-compartmental ODFs [53].
- Structural connectivity estimates are accurate: the outcome of diffusion-simulated connectivity (DiSCo) challenge [54].
- Real-Time Rendering of Massive Multi-Tensor Fields Using Modern OpenGL [55].
- MRDS optimization
- results of the study using MRDS and tractometry\_flow on the myelo\_inferno.

## 5.3 Collaborations

- Imeka** Intership with Imeka Solutions Inc.; a company specialized in brain imaging specifically white matter, neuroinflammation, free-water and more. We will develop mechanisms and modify others already in place to integrate the MRDS-based pipeline into the Imeka's software infrastructure. This could enable the ability to test the pipeline on large public and clinical Imeka databases with more than 5,000 MRI exams (Duration: 3-6 months).
- NYU** Possible collaboration with the NYU MRI Biophysics Group, which is one of the most relevant laboratories in the field. It will focus on multimetric analysis of white matter tracts in the multi-compartment standard model.
- UMC** Possible collaboration with Chen-Pei Lin applying the proposed pipeline to HARDI multi-shell post mortem Parkinson brain data.

# Chapter 6

## Conclusions

While multiple research and tools currently exist to perform dMRI tractometry. Non of the these articles have presented the ability to perform analysis based on fixel-specific dMRI metrics. In this work we have presented a novel dMRI tractometry pipeline that can combine tractography with fixel-based dMRI derived from an improved, robust and accurate multi-tensor fitting to account for tract profiles. Furthermore, it shows promising results on the synthetic phantoms and in-vivo clinical grade data, where we saw the pipeline being sensitive and, more importantly, specific to changes in the WM. Besides, the results in healthy control in-vivo data shows that even without the improvements of MRDS, the pipeline is robust and accurate to fiber crossing. Of course, it is still required to be tested on relapsing remitting MS data. However, the preliminary experiments point to a promising result when testing the pipeline in MS data, which would be a fundamental contribution to the dMRI community. It is important for the community to have a fast, accurate, robust and easy-to-use pipeline for tractometry analysis that can be specific and not only sensitive to WM anomalies.

Our previous abstract publications made a solid starting point for this work. Considering the preliminary results and the given schedule for the next years, make this project viable and finishable on time.

# Appendix A

## Appendix

### A.1 Spherical Harmonics

Spherical harmonics are special functions defined on  $\mathbb{S}^2$ . They are used to represent any well-behaved spherical functions as they are a complete orthonormal base. They are defined for an order  $l \geq 0$  and degree  $-l \leq m \leq l$  as:

$$Y_l^m(\theta, \phi) = \sqrt{\frac{(2l+1)}{4\pi} \frac{(l-m)!}{(l+m)!}} P_l^m(\cos\theta) e^{im\phi}, \quad (\theta, \phi) \in \mathbb{S}^2, \quad (\text{A.1})$$

where  $P_l^m$  are the Legendre polynomials. Thus, any well-behaved spherical function signal  $S$  on  $\mathbb{S}^2$  can be represented as its spherical harmonic expansion:

$$S(\theta, \phi) = \sum_{l=0}^{\infty} \sum_{m=-l}^l c_l^m Y_l^m(\theta, \phi), \quad (\theta, \phi) \in \mathbb{S}^2.$$

Usually, the spherical harmonic expansion is truncated at some  $l_{max}$  because it is impossible to represent an infinite number of terms in the computer. Therefore,

$$S(\theta, \phi) \simeq \sum_{l=0}^{l_{max}} \sum_{m=-l}^l c_l^m Y_l^m(\theta, \phi), \quad (\theta, \phi) \in \mathbb{S}^2. \quad (\text{A.2})$$

Due to the nature of the diffusion MRI signals, the data involved are real and symmetric. These two important properties allow to use real basis with no imaginary components, and ignore all odd order terms in the harmonic expansion. Thus, the spherical basis functions  $Y_l^m(\theta, \phi)$  can be simplified as

$$Y_l^m(\theta, \phi) = \begin{cases} 0 & l \text{ odd}, \\ \sqrt{\frac{(2l+1)}{2\pi} \frac{(l+m)!}{(l-m)!}} P_l^{-m}(\cos\theta) \sin(-m\phi) & m < 0, \\ \sqrt{\frac{(2l+1)}{2\pi} \frac{(l-m)!}{(l+m)!}} P_l^m(\cos\theta) \cos(m\phi) & m \geq 0. \end{cases}$$

In this case, the spherical coefficients  $c_l^m$  and their corresponding basis functions  $Y_l^m(\theta, \phi)$  can be conform to a new indexing  $j_{l,m}$  such that  $j_{l,m} = \frac{1}{2}l(l+1) + m$  [?], and for notation convenience we will take  $j := 1 + j_{l,m}$ , see Table A.1.

$j$	1	2	3	4	5	6	7	...
$j_{l,m}$	0	1	2	3	4	5	6	...
$l, m$	$l=0$ $m=0$	$l=2$ $m=-2$	$l=2$ $m=-1$	$l=2$ $m=0$	$l=2$ $m=1$	$l=2$ $m=2$	$l=4$ $m=-4$	...

**Table A.1:** New indexing of the spherical harmonics coefficients and basis functions.

If  $l$  takes only even values and  $m \in [-l, l]$ , then  $j$  lies on  $[1, R]$  where  $R = \frac{1}{2}(l_{max} + 1)(l_{max} + 2)$ . Thus, the signal can be expressed as [?]:

$$S(\theta, \phi) = \sum_{j=0}^R c_j Y_j(\theta, \phi), \quad (\theta, \phi) \in \mathbb{S}^2. \quad (\text{A.3})$$

Let's suppose we have a set of  $n$  gradient directions  $\{\mathbf{g}_i = (\theta_i, \phi_i) \in \mathbb{S}^2\}_{i=1}^n$  uniformly distributed on  $\mathbb{S}^2$ . Along each of these gradient directions  $\mathbf{g}_i$  a 3D diffusion MRI signal  $S(\theta, \phi)$  of size  $X \times Y \times Z$  is measured. Hence, at each imaging voxel, we have a discrete sampling  $\{S(\theta_1, \phi_1), \dots, S(\theta_n, \phi_n)\}$  of  $S(\theta, \phi)$  along  $n$  points on the unit sphere. Now, substituting the samples into the equation A.3 we have

$$\begin{aligned} S(\theta_1, \phi_1) &= \sum_{j=0}^R c_j Y_j(\theta_1, \phi_1) \\ &\dots \\ S(\theta_n, \phi_n) &= \sum_{j=0}^R c_j Y_j(\theta_n, \phi_n), \end{aligned}$$

The previous linear system can be written in matrix form as  $\mathbf{S} = \mathbf{Y}\mathbf{c}$ , where

$$\mathbf{S} = \begin{pmatrix} S(\theta_1, \phi_1) \\ \vdots \\ S(\theta_n, \phi_n) \end{pmatrix} \in \mathbb{R}^n, \quad \mathbf{c} = \begin{pmatrix} c_1 \\ \vdots \\ c_R \end{pmatrix} \in \mathbb{R}^R, \quad \mathbf{Y} = \begin{pmatrix} Y_1(\theta_1, \phi_1) & \cdots & Y_R(\theta_1, \phi_1) \\ \vdots & \ddots & \vdots \\ Y_1(\theta_n, \phi_n) & \cdots & Y_R(\theta_n, \phi_n) \end{pmatrix} \in \mathbb{R}^{n \times R}.$$

Therefore, in order to fit the signal, the spherical harmonic coefficients can be obtained with the standard least-squares solution  $\mathbf{c} = (\mathbf{Y}^T \mathbf{Y})^{-1} \mathbf{S}$  [3].

## A.2 Proof that Multi-Shell HARDI Acquisitions are Required to Fit Multi-Tensor Models

In [?] was proved that the tensors and volume fractions of a multi-tensor model cannot be uniquely determined when using single-shell HARDI acquisitions. Considering the multi-tensor model as

$$S_i(\mathbb{D}, f) = S_0 \sum_{j=1}^K f_j S_{i,j}, \quad (\text{A.4})$$

where  $S_0$  is the  $T_2$ -weighted image,  $\mathbb{D} = (\mathbb{D}_1, \dots, \mathbb{D}_K)$  the tensors representing the total number of  $K$  fascicles,  $S_{i,j}$  is the diffusion signal arising from a single fascicle using the single tensor model of Equation A.4, i.e.  $S_{i,j} = e^{-b_i \mathbf{g}_i^T \mathbb{D}_j \mathbf{g}_i}$ , and  $f$  are the volume fractions of each component such that  $f_j \in [0, 1]$  and  $\sum_j f_j = 1$ .

Let's consider a model with two fascicles represented by the two diffusion tensors  $\mathbb{D} = (\mathbb{D}_1, \mathbb{D}_2)$ , the fractions  $f = (f_1, 1 - f_1)$  and  $N$  signal measurements  $\{y_i = S(\mathbf{g}_i, b)\}_{i=1}^N$  acquired along the  $N$  diffusion gradients  $\{\mathbf{g}_i\}_{i=1}^N$  with a unique non-zero b-value  $b$ .  $\mathbb{D}$  and  $f$  are generally estimated by a least-square approach

$$(\mathbb{D}, f) = \underset{\mathbb{D}, f}{\operatorname{argmin}} \sum_{i=1}^N (S_i(\mathbb{D}, f) - y_i)^2. \quad (\text{A.5})$$

Then, for any  $\alpha, \beta > 0$  the Equation A.4 can be written as:

$$\begin{aligned} S_i(\mathbb{D}, f) &= S_0 (f_1 S_{i,1} + (1 - f_1) S_{i,2}) = S_0 \left( \frac{\alpha}{\alpha} f_1 S_{i,1} + \frac{\beta}{\beta} (1 - f_1) S_{i,2} \right) = S_0 \left( \frac{\alpha}{\alpha} f_1 e^{-b \mathbf{g}_i^T \mathbb{D}_1 \mathbf{g}_i} + \frac{\beta}{\beta} (1 - f_1) e^{-b \mathbf{g}_i^T \mathbb{D}_2 \mathbf{g}_i} \right) \\ &= S_0 \left( \alpha f_1 e^{-b \mathbf{g}_i^T \mathbb{D}_1 \mathbf{g}_i - \ln(\alpha)} + \beta (1 - f_1) e^{-b \mathbf{g}_i^T \mathbb{D}_2 \mathbf{g}_i - \ln(\beta)} \right). \end{aligned}$$

Because  $\mathbf{g}_i^T \mathbf{g}_i = 1$ , we have  $\ln(\alpha) = \mathbf{g}_i^T (\ln(\alpha) \mathbb{I}_3) \mathbf{g}_i$  where  $\mathbb{I}_3$  is the  $3 \times 3$  identity matrix. Therefore, substituting previous equality and Equation A.6 in Equation A.5 it becomes

$$\begin{aligned} (\mathbb{D}, f) &= \underset{\mathbb{D}, f}{\operatorname{argmin}} \sum_{i=1}^N \left( S_0 \left( \alpha f_1 e^{-b \mathbf{g}_i^T \mathbb{D}_1 \mathbf{g}_i - \ln(\alpha)} + \beta (1 - f_1) e^{-b \mathbf{g}_i^T \mathbb{D}_2 \mathbf{g}_i - \ln(\beta)} \right) - y_i \right)^2 \\ &= \underset{\mathbb{D}, f}{\operatorname{argmin}} \sum_{i=1}^N \left( S_0 \left( \alpha f_1 e^{-b \mathbf{g}_i^T (\mathbb{D}_1 + \frac{\ln(\alpha)}{b} \mathbb{I}_3) \mathbf{g}_i} + \beta (1 - f_1) e^{-b \mathbf{g}_i^T (\mathbb{D}_2 + \frac{\ln(\beta)}{b} \mathbb{I}_3) \mathbf{g}_i} \right) - y_i \right)^2 \end{aligned} \quad (\text{A.7})$$

Now, let's take  $\alpha \in (0, 1]$  and  $\beta = (1 - \alpha f_1) / (1 - f_1)$ , it is possible to show that  $\beta > 0$ , and that taking  $f' = (f'_1, f'_2) = (\alpha f_1, \beta (1 - f_1))$ , it leads  $f'_1 + f'_2 = 1$  and  $0 < f'_1, f'_2 \leq 1$ . Additionally, if  $\mathbb{D}' = (\mathbb{D}'_1, \mathbb{D}'_2) = \left( \mathbb{D}_1 + \frac{\ln(\alpha)}{b} \mathbb{I}_3, \mathbb{D}_2 + \frac{\ln(\beta)}{b} \mathbb{I}_3 \right)$ , it follows from Equation A.7 that

$$\begin{aligned}
(\mathbb{D}, f) &= \underset{\mathbb{D}', f'}{\operatorname{argmin}} \sum_{i=1}^N \left( S_0 \left( f'_1 e^{-b \mathbf{g}_i^T \mathbb{D}'_1 \mathbf{g}_i} + f'_2 e^{-b \mathbf{g}_i^T \mathbb{D}'_2 \mathbf{g}_i} \right) - y_i \right)^2 \\
&= \underset{\mathbb{D}', f'}{\operatorname{argmin}} \sum_{i=1}^N \left( S_i \left( \mathbb{D}', f' \right) - y_i \right)^2.
\end{aligned}$$

It indicates that  $(\mathbb{D}', f')$  is also solution of Equation A.5. In fact, there is an infinite number of different solutions  $(\mathbb{D}', f')$  by varying the value of  $\alpha$ . Intuitively, this means that when using a single non-zero b-value, it is not possible to find a unique solution to Equation A.5. That's why multi-tensor approaches have frequently been reported to be numerically challenging and unstable when using single-shell diffusion MRI. However, it is not the case with multi-shell data with multiple non-zero b-values  $\{b_i\}_{i=1}^N$  because  $\mathbb{D}'_i = \left( \mathbb{D}_1 + \frac{\ln(\alpha)}{b_i} \mathbb{I}_3, \mathbb{D}_2 + \frac{\ln(\beta)}{b_i} \mathbb{I}_3 \right)$  is now function of  $b_i$ .



## Bibliography

- [1]
- [2]
- [3]
- [4]
- [5] Tuch DS, Reese TG, Wiegell MR, Makris N, Belliveau JW, Wedeen VJ. High angular resolution diffusion imaging reveals intravoxel white matter fiber heterogeneity. *Magn Reson Med.* 2002 Oct;48(4):577-82. doi: 10.1002/mrm.10268. PMID: 12353272.
- [6] Hosey T, Williams G, Ansorge R (2005) Inference of multiple fiber orientations in high angular resolution diffusion imaging. *Magn Reson Med* 54: 1480–1489.
- [7] Kreher BW, Schneider JF, Mader I, Martin E, Hennig J, et al. (2005) Multi-tensor approach for analysis and tracking of complex fiber configurations. *Magn Reson Med* 54: 1216–1225.
- [8] Melie-Garcia L, C-Rodriguez EJ, Aleman-Gomez Y, Lin CP, Iturria-Medina Y, et al. (2008) A Bayesian framework to identify principal intravoxel diffusion profiles based on diffusion-weighted MR imaging. *Neuroimage* 42: 750–770.
- [9]
- [10]
- [11]
- [12] NVIDIA, Vingelmann, P. & Fitzek, F.H.P., 2020. CUDA, release: 10.2. 89, Available at: <https://developer.nvidia.com/cuda-toolkit>.

- [13] Ramirez-Manzanares, M. Rivera, B. C. Vemuri, P. Carney, and T. Mareci. Diffusion basis functions decomposition for estimating white matter intravoxel fiber geometry. *IEEE Transactions on Medical Imaging*, 26(8):1091–1102, 2007.
- [14]
- [15]
- [16] Reymbaut A, Caron AV, Gilbert G, Szczepankiewicz F, Nilsson M, Warfield SK, Descoteaux M, Scherrer B. Magic DIAMOND: Multi-fascicle diffusion compartment imaging with tensor distribution modeling and tensor-valued diffusion encoding. *Med Image Anal*. 2021 May;70:101988. doi: 10.1016/j.media.2021.101988. Epub 2021 Feb 4. PMID: 33611054.
- [17] Rokem A, Yeatman JD, Pestilli F, Kay KN, Mezer A, van der Walt S, Wandell BA. Evaluating the accuracy of diffusion MRI models in white matter. *PLoS One*. 2015 Apr 16;10(4):e0123272. doi: 10.1371/journal.pone.0123272. Erratum in: *PLoS One*. 2015;10(9):e0139150. PMID: 25879933; PMCID: PMC4400066.
- [18]
- [19] Basser PJ, Mattiello J, Turner R, Le Bihan D. Diffusion tensor echo-planar imaging of human brain. InProceedings of the SMRM 1993 Aug (Vol. 584).
- [20] Basser PJ, Mattiello J, Le Bihan D. Estimation of the effective self-diffusion tensor from the NMR spin echo. *J Magn Reson* 1994; 103: 247–254.
- [21] Basser PJ, Mattiello J, Le Bihan D. MR diffusion tensor spectroscopy and imaging. *Biophys J* 1994; 66: 259–267.
- [22]
- [23]
- [24]
- [25]
- [26] [http://hardi.epfl.ch/static/events/2012\\_ISBI/download.html](http://hardi.epfl.ch/static/events/2012_ISBI/download.html)
- [27] <https://zenodo.org/record/2602049#.Y1UzCHaZNPY>
- [28] C. Poupon, B. Rieul, I. Kezele, M. Perrin, F. Poupon, J.F. Mangin New diffusion phantoms dedicated to the study and validation of high-angular-resolution diffusion imaging (HARDI) models *Magn. Reson. Med.*, 60 (2008), pp. 1276-1283, 10.1002/mrm.21789.

- [29] J. D. Tournier, C. H. Yeh, F. Calamante, K. H. Cho, A. Connelly, and C. P. Lin, "Resolving crossing fibres using constrained spherical deconvolution: Validation using diffusion-weighted imaging phantom data," *NeuroImage*, vol. 42, pp. 617–625, 2008.
- [30] F. B. Laun, L. R. Schad, J. Klein, and B. Stieltjes, "How background noise shifts eigenvectors and increases eigenvalues in DTI," in *MAGMA*, 2009, vol. 22, pp. 151–158.
- [31] F. B. Laun, S. Huff, and B. Stieltjes, "On the effects of dephasing due to local gradients in diffusion tensor imaging experiments: Relevance for diffusion tensor imaging fiber phantoms," *Magn. Reson. Imag.*, vol. 27, pp. 541–548, 2009.
- [32] P. Pullens, A. Roebroeck, and R. Goebel, "Ground truth hardware phantoms for validation of diffusion-weighted MRI applications," *J. Magn. Reson. Imag.*, vol. 32, pp. 482–488, 2010.
- [33] K. H. Fritzsche, F. B. Laun, H. P. Meinzer, and B. Stieltjes, "Opportunities and pitfalls in the quantification of fiber integrity: What can we gain from Q-ball imaging?," *NeuroImage*, vol. 51, pp. 242–251, 2010.
- [34] A. Moussavi-Biugui, B. Stieltjes, K. Fritzsche, W. Semmler, and F. B. Laun, "Novel spherical phantoms for Q-ball imaging under in vivo conditions," *Magn. Reson. Med.*, vol. 65, pp. 190–194, 2011.
- [35] F. L. Zhou, P. L. Hubbard, S. J. Eichhorn, and G. J. Parker, "Coaxially electrospun axon-mimicking fibers for diffusion magnetic resonance imaging," *ACS Appl. Mater. Interfaces*, vol. 4, pp. 6311–6316, 2012.
- [36] T. A. Kuder, B. Stieltjes, P. Bachert, W. Semmler, and F. B. Laun, "Advanced fit of the diffusion kurtosis tensor by directional weighting and regularization," *Magn. Reson. Med.*, vol. 67, pp. 1401–1411, 2012.
- [37] M. Bach, K. H. Fritzsche, B. Stieltjes, and F. B. Laun, "Investigation of resolution effects using a specialized diffusion tensor phantom," *Magn. Reson. Med.*, 2013.
- [38] Ivana Drobnjak, Peter Neher, Cyril Poupon, Tabinda Sarwar, Physical and digital phantoms for validating tractography and assessing artifacts, *NeuroImage*, Volume 245, 2021, 118704, ISSN 1053-8119, <https://doi.org/10.1016/j.neuroimage.2021.118704>.
- [39] Els Fieremans, Hong-Hsi Lee, Physical and numerical phantoms for the validation of brain microstructural MRI: A cookbook, *NeuroImage*, Volume 182, 2018, Pages 39-61, ISSN 1053-8119, <https://doi.org/10.1016/j.neuroimage.2018.06.046>.

- [40] Brachat J, Comon P, Mourrain B, Tsigaridas EP. Symmetric tensor decomposition. *Linear Algebra and Applications*. 2010; 433(11–12):1851–1872.
- [41]
- [42]
- [43]
- [44]
- [45]
- [46]
- [47]
- [48]
- [49]
- [50]
- [51]
- [52]
- [53]
- [54]
- [55]
- [56]
- [57] Garyfallidis E, Brett M, Amirbekian B, Rokem A, van der Walt S, Descoteaux M, Nimmo-Smith I; Dipy Contributors. Dipy, a library for the analysis of diffusion MRI data. *Front Neuroinform*. 2014 Feb 21;8:8. doi: 10.3389/fninf.2014.00008. PMID: 24600385; PMCID: PMC3931231.
- [58] Tournier, J.-D.; Smith, R. E.; Raffelt, D.; Tabbara, R.; Dhollander, T.; Pietsch, M.; Christiaens, D.; Jeurissen, B.; Yeh, C.-H. & Connelly, A. MRtrix3: A fast, flexible and open software framework for medical image processing and visualisation. *NeuroImage*, 2019, 202, 116137.
- [59] [https://mrtrix.readthedocs.io/en/latest/concepts/fixels\\_dixels.html](https://mrtrix.readthedocs.io/en/latest/concepts/fixels_dixels.html)

- [60] Dhollander T, Clemente A, Singh M, Boonstra F, Civier O, Duque JD, Egorova N, Enticott P, Fuelscher I, Gajamange S, Genc S, Gottlieb E, Hyde C, Imms P, Kelly C, Kirkovski M, Kolbe S, Liang X, Malhotra A, Mito R, Poudel G, Silk TJ, Vaughan DN, Zanin J, Raffelt D, Caeyenberghs K. Fixel-based Analysis of Diffusion MRI: Methods, Applications, Challenges and Opportunities. *Neuroimage*. 2021 Nov 1;241:118417. doi: 10.1016/j.neuroimage.2021.118417. Epub 2021 Jul 21. PMID: 34298083.
- [61] Jeurissen B, Leemans A, Tournier JD, Jones DK, Sijbers J. Investigating the prevalence of complex fiber configurations in white matter tissue with diffusion magnetic resonance imaging. *Hum Brain Mapp*. 2013 Nov;34(11):2747-66. doi: 10.1002/hbm.22099. Epub 2012 May 19. PMID: 22611035; PMCID: PMC6870534.
- [62] V. J. Wedeen, T. L. Davis, R. M. Weisskoff, R. B. H. Tootell, B. R. Rosen, and J. W. Belliveau. "White Matter Connectivity Explored by MRI". In: Proceedings of The Organization for Human Brain Mapping (OHBM) Annual Meeting. The Organization for Human Brain Mapping. Paris, France, 1995: 69.
- [63] Mori S, Crain BJ, Chacko VP, van Zijl PC. Three-dimensional tracking of axonal projections in the brain by magnetic resonance imaging. *Ann Neurol*. 1999 Feb;45(2):265-9. doi: 10.1002/1531-8249(199902)45:2<265::aid-ana21>3.0.co;2-3. PMID: 9989633.
- [64] Mori, S. and van Zijl, P.C.M. (2002), Fiber tracking: principles and strategies - a technical review. *NMR Biomed.*, 15: 468-480. <https://doi.org/10.1002/nbm.781>.
- [65] Zhang, F., Daducci, A., He, Y., Schiavi, S., Seguin, C., Smith, R., ... & O'Donnell, L. J. (2022). Quantitative mapping of the brain's structural connectivity using diffusion MRI tractography: A review. *Neuroimage*, 118870.
- [66] Tournier, J.D., Calamante, F., Connelly, A., 2010. Improved probabilistic streamlines tractography by 2nd order integration over fibre orientation distributions, in: *Proceedings of the International Society for Magnetic Resonance in Medicine*, p. 1670.
- [67] Descoteaux, M., Deriche, R., Knosche, T.R., Anwander, A., 2008. Deterministic and probabilistic tractography based on complex fibre orientation distributions. *IEEE transactions on medical imaging* 28, 269–286.
- [68] Behrens, T.E., Berg, H.J., Jbabdi, S., Rushworth, M.F., Woolrich, M.W., 2007. Probabilistic diffusion tractography with multiple fibre orientations: What can we gain? *Neuroimage* 34, 144–155.

- [69] Friman, O., Farneback, G., Westin, C.F., 2006. A bayesian approach for stochastic white matter tractography. *IEEE transactions on medical imaging* 25, 965–978.
- [70] Lazar, M., Alexander, A.L., 2005. Bootstrap white matter tractography (boot-trac). *NeuroImage* 24, 524–532.
- [71] Tournier, J.D., Calamante, F., Gadian, D.G., Connelly, A., 2003. Diffusion-weighted magnetic resonance imaging fibre tracking using a front evolution algorithm. *NeuroImage* 20, 276–288.
- [72] Jackowski, M., Kao, C.Y., Qiu, M., Constable, R.T., Staib, L.H., 2005. White matter tractography by anisotropic wavefront evolution and diffusion tensor imaging. *Medical image analysis* 9, 427–440.
- [73] Fernandez-Miranda, J.C., Pathak, S., Engh, J., Jarbo, K., Verstynen, T., Yeh, F.C., Wang, Y., Mintz, A., Boada, F., Schneider, W., et al., 2012. High-definition fiber tractography of the human brain: neuroanatomical validation and neurosurgical applications. *Neurosurgery* 71, 430–453.
- [74] Malcolm, J.G., Shenton, M.E., Rathi, Y., 2010. Filtered multitensor tractography. *IEEE transactions on medical imaging* 29, 1664–1675.
- [75] Reddy, C.P., Rathi, Y., 2016. Joint multi-fiber noddi parameter estimation and tractography using the unscented information filter. *Frontiers in neuroscience* 10, 166.
- [76] Wasserthal, J., Neher, P.F., Hirjak, D., Maier-Hein, K.H., 2019. Combined tract segmentation and orientation mapping for bundle-specific tractography. *Medical image analysis* 58, 101559.
- [77] Feng, Y., He, J., 2020. Asymmetric fiber trajectory distribution estimation using streamline differential equation. *Medical image analysis* 63, 101686.
- [78] Pichon, E., Westin, C.F., Tannenbaum, A.R., 2005. A Hamilton-JacobiBellman approach to high angular resolution diffusion tractography. *Medical image computing and computer-assisted intervention* 8, 180– 187.
- [79] Sepasian, N., ten Thije Boonkkamp, J., Ter Haar Romeny, B., Vilanova Bartroli, A., 2012. Multivalued geodesic ray-tracing for computing brain connections using diffusion tensor imaging. *SIAM Journal on Imaging Sciences* 5, 483–504.
- [80] Mangin, J.F., Poupon, C., Cointepas, Y., Riviere, D., Papadopoulos-Orfanos, D., Clark, C.A., Regis, J., Le Bihan, D., 2002. A framework based on spin glass models for the inference of anatomical connectivity from diffusion-weighted MR data - a technical review. *NMR in Biomedicine* 15, 481–492.

- [81] Kreher, B.W., Mader, I., Kiselev, V.G., 2008. Gibbs tracking: A novel approach for the reconstruction of neuronal pathways. *Magnetic Resonance in Medicine* 60, 953–963.
- [82] Fillard, P., Poupon, C., Mangin, J.F., 2009. A Novel Global Tractography Algorithm Based on an Adaptive Spin Glass Model, in: *Medical Image Computing and Computer-Assisted Intervention*, Springer. pp. 927–934.
- [83] Reisert, M., Mader, I., Anastasopoulos, C., Weigel, M., Schnell, S., Kiselev, V., 2011. Global fiber reconstruction becomes practical. *NeuroImage* 54, 955–962.
- [84] Mangin, J.F., Fillard, P., Cointepas, Y., Le Bihan, D., Frouin, V., Poupon, C., 2013. Toward global tractography. *Mapping the Connectome* 80, 290–296.
- [85] Christiaens, D., Reisert, M., Dhollander, T., Sunaert, S., Suetens, P., Maes, F., 2015. Global tractography of multi-shell diffusion-weighted imaging data using a multi-tissue model. *NeuroImage* 123, 89–101.
- [86] Teillac, A., Beaujouin, J., Poupon, F., Mangin, J.F., Poupon, C., 2017. A novel anatomically-constrained global tractography approach to monitor sharp turns in gyri, in: *International Conference on Medical Image Computing and Computer-assisted Intervention*, Springer. pp. 532–539.
- [87] Wu, X., Xie, M., Zhou, J., Anderson, A.W., Gore, J.C., Ding, Z., 2012b. Globally optimized fiber tracking and hierarchical clustering – a unified framework. *Magnetic Resonance Imaging* 30, 485–495.
- [88] Battocchio, M., Schiavi, S., Descoteaux, M., Daducci, A., 2020. Improving tractography accuracy using dynamic filtering, in: *CDMRI*, p. accepted to appear.
- [89] Lemkadem, A., Skioldebrand, D., Dal Palu, A., Thiran, J.P., Daducci, A., 2014. Global tractography with embedded anatomical priors for quantitative connectivity analysis. *Frontiers in Neurology* 5, 232.
- [90] Close, T.G., Tournier, J.D., Johnston, L.A., Calamante, F., Mareels, I., Connelly, A., 2015. Fourier Tract Sampling (FouTS): A framework for improved inference of white matter tracts from diffusion MRI by explicitly modelling tract volume. *NeuroImage* 120, 412–427.
- [91] Poulin, P., Jorgens, D., Jodoin, P.M., Descoteaux, M., 2019. Tractography and machine learning: Current state and open challenges. *Magnetic resonance imaging* 64, 37–48.
- [92] Neher, P.F., Cottereau, M.A., Houde, J.C., Descoteaux, M., Maier-Hein, L.K.H., 2017. Fiber tractography using machine learning. *Neuroimage* 158, 417–429.

- [93] Wegmayr, V., Giulieri, G., Holdener, S., Buhmann, J., 2018. Data-driven fiber tractography with neural networks, in: 2018 IEEE 15th international symposium on biomedical imaging (ISBI 2018), IEEE. pp. 1030– 1033.
- [94] Sarwar, T., Seguin, C., Ramamohanarao, K., Zalesky, A., 2020. Towards deep learning for connectome mapping: A block decomposition framework. *NeuroImage* 212, 116654.
- [95] O'Donnell, L., Haker, S., Westin, C.F., 2002. New approaches to estimation of white matter connectivity in diffusion tensor MRI: Elliptic pdes and geodesics in a tensor-warped space, in: International Conference on Medical Image Computing and Computer-Assisted Intervention, Springer. pp. 459–466.
- [96] Jbabdi, S., Woolrich, M., Andersson, J., Behrens, T., 2007. A Bayesian framework for global tractography. *NeuroImage* 37, 116–129.
- [97] Jbabdi, S., Bellec, P., Toro, R., Daunizeau, J., Pelegrini-Issac, M., Benali, H., 2008. Accurate anisotropic fast marching for diffusion-based geodesic tractography. *Journal of Biomedical Imaging* 2008, 1–12.
- [98] Wu, X., Xu, Q., Xu, L., Zhou, J., Anderson, A.W., Ding, Z., 2009. Genetic white matter fiber tractography with global optimization. *Journal of Neuroscience Methods* 184, 375–379.
- [99] Neher, P.F., Descoteaux, M., Houde, J.C., Stieltjes, B., Maier-Hein, K.H., 2015. Strengths and weaknesses of state of the art fiber tractography pipelines—a comprehensive in-vivo and phantom evaluation study using tractometer. *Medical image analysis* 26, 287–305.
- [100] Jeurissen, B., Descoteaux, M., Mori, S., Leemans, A., 2019. Diffusion MRI fiber tractography of the brain. *NMR in Biomedicine* 32, e3785.
- [101] Rheault, F., Poulin, P., Caron, A.V., St-Onge, E., Descoteaux, M., 2020b. Common misconceptions, hidden biases and modern challenges of dMRI tractography. *Journal of Neural Engineering* 17, 11001. doi:10.1088/1741-2552/ab6aad.
- [102] Smith, R.E., Connelly, A., Calamante, F., 2020c. Diffusion MRI fiber tractography, in: Advances in Magnetic Resonance Technology and Applications. Elsevier. volume 1, pp. 533–569.
- [103] Farquharson S, Tournier JD, Calamante F, Fabinyi G, Schneider-Kolsky M, Jackson GD, Connelly A. White matter fiber tractography: why we need to move beyond DTI. *J Neurosurg.* 2013 Jun;118(6):1367-77. doi: 10.3171/2013.2.JNS121294. Epub 2013 Mar 29. PMID: 23540269.

- [104] Li L, Rilling JK, Preuss TM, Glasser MF, Hu X. The effects of connection reconstruction method on the interregional connectivity of brain networks via diffusion tractography. *Hum Brain Mapp.* 2012 Aug;33(8):1894-913. doi: 10.1002/hbm.21332. Epub 2011 Sep 16. PMID: 21928316; PMCID: PMC6414228.
- [105] Weiss C, Tursunova I, Neuschmelting V, Lockau H, Nettekoven C, Oros-Peusquens AM, Stoffels G, Rehme AK, Faymonville AM, Shah NJ, Langen KJ, Goldbrunner R, Grefkes C. Improved nTMS- and DTI-derived CST tractography through anatomical ROI seeding on anterior pontine level compared to internal capsule. *Neuroimage Clin.* 2015 Jan 20;7:424-37. doi: 10.1016/j.nicl.2015.01.006. PMID: 25685709; PMCID: PMC4314616.
- [106] Kreher, B., Mader, I., Kiselev, V., 2008. Gibbs tracking: A novel approach for the reconstruction of neuronal pathways. *Magn Reson Med* 60, 953-63.
- [107] Girard G, Whittingstall K, Deriche R, Descoteaux M. Towards quantitative connectivity analysis: reducing tractography biases. *Neuroimage.* 2014 Sep;98:266-78. doi: 10.1016/j.neuroimage.2014.04.074. Epub 2014 May 9. PMID: 24816531.
- [108] Smith SM. Fast robust automated brain extraction. *Hum Brain Mapp.* 2002 Nov;17(3):143-55. doi: 10.1002/hbm.10062. PMID: 12391568; PMCID: PMC6871816.
- [109] Veraart J, Novikov DS, Christiaens D, Ades-Aron B, Sijbers J, Fieremans E. Denoising of diffusion MRI using random matrix theory. *Neuroimage.* 2016 Nov 15;142:394-406. doi: 10.1016/j.neuroimage.2016.08.016. Epub 2016 Aug 11. PMID: 27523449; PMCID: PMC5159209.
- [110] Tustison NJ, Avants BB, Cook PA, Zheng Y, Egan A, Yushkevich PA, Gee JC. N4ITK: improved N3 bias correction. *IEEE Trans Med Imaging.* 2010 Jun;29(6):1310-20. doi: 10.1109/TMI.2010.2046908. Epub 2010 Apr 8. PMID: 20378467; PMCID: PMC3071855.
- [111] Gudbjartsson H, Patz S. The Rician distribution of noisy MRI data. *Magn Reson Med.* 1995 Dec;34(6):910-4. doi: 10.1002/mrm.1910340618. Erratum in: *Magn Reson Med* 1996 Aug;36(2):332. PMID: 8598820; PMCID: PMC2254141.
- [112] A. Daducci, E. J. Canales-Rodríguez, H. Zhang, T. B. Dyrby, D. C. Alexander, and J.-P. Thiran. "Accelerated Microstructure Imaging via Convex Optimization (AMICO) from diffusion MRI data". *NeuroImage.* 105:32-44. 2015.

- [113] Theaud, G., Houde, J.-C., Boré, A., Rheault, F., Morency, F., Descoteaux, M., TractoFlow: A robust, efficient and reproducible diffusion MRI pipeline leveraging Nextflow & Singularity, *NeuroImage*, <https://doi.org/10.1016/j.neuroimage.2020.116889>.
- [114] Dell'Acqua, F., Simmons, A., Williams, S.C. and Catani, M. (2013), Can spherical deconvolution provide more information than fiber orientations? Hindrance modulated orientational anisotropy, a true-tract specific index to characterize white matter diffusion. *Hum. Brain Mapp.*, 34: 2464-2483. <https://doi.org/10.1002/hbm.22080>.
- [115] Rheault, Francois. Analyse et reconstruction de faisceaux de la matière blanche. page 137-170, (2020), <https://savoirs.usherbrooke.ca/handle/11143/17255>
- [116] Garyfallidis, Eleftherios, et al. Recognition of white matter bundles using local and global streamline-based registration and clustering. *NeuroImage* 170 (2018) <https://doi.org/10.1016/j.neuroimage.2017.07.015>
- [117] Kurtzer GM, Sochat V, Bauer MW Singularity: Scientific containers for mobility of compute. *PLoS ONE* 12(5): e0177459 (2017) <https://doi.org/10.1371/journal.pone.0177459>
- [118] P. Di Tommaso, et al. Nextflow enables reproducible computational workflows. *Nature Biotechnology* 35, 316-319 (2017) <https://doi.org/10.1038/nbt.3820>
- [119] Dayan M, Monohan E, Pandya S, Kuceyeski A, Nguyen TD, Raj A, Gauthier SA. Profilometry: A new statistical framework for the characterization of white matter pathways, with application to multiple sclerosis. *Hum Brain Mapp.* 2016 Mar;37(3):989-1004. doi: 10.1002/hbm.23082. Epub 2015 Dec 15. PMID: 26667008; PMCID: PMC6867537.
- [120] Bells S, Cercignani M, Deoni S, Assaf Y, Pasternak O, Evans C, Leemans A, Jones D (2011). Tractometry-comprehensive multi-modal quantitative assessment of white matter along specific tracts, in: 17th Annual General Meeting of the British Chapter of the ISMRM.
- [121] De Santis S, Drakesmith M, Bells S, Assaf Y, Jones D (2014): Why diffusion tensor mri does well only some of the time: Variance and covariance of white matter tissue microstructure attributes in the living human brain. *NeuroImage* 89:35-44.
- [122] Jones D, Travis A, Eden G, Pierpaoli C, Basser P (2005): Pasta: Pointwise assessment of streamline tractography attributes. *Magn Reson Med* 53:1462-1467.

- [123] Corouge I, Fletcher P, Joshi S, Gouttard S, Gerig G (2006): Fiber tract-oriented statistics for quantitative diffusion tensor mri analysis. *Medical Image Analysis* 10:786–798.
- [124] Maddah M, Grimson W, Warfield S, Wells W (2008): A unified framework for clustering and quantitative analysis of white matter fiber tracts. *Med Image Analysis* 12:191–202.
- [125] Yeatman JD, Dougherty RF, Myall NJ, Wandell BA, Feldman HM. Tract profiles of white matter properties: automating fiber-tract quantification. *PLoS One*. 2012;7(11):e49790. doi: 10.1371/journal.pone.0049790. Epub 2012 Nov 14. PMID: 23166771; PMCID: PMC3498174.
- [126] Stikov N, Perry L, Mezer A, Rykhlevskaia E, Wandell B, Pauly J, Dougherty R (2011): Bound pool fractions complement diffusion measures to describe white matter micro and macrostructure. *NeuroImage* 54:1112–1121.
- [127] Kruper J, Yeatman JD, Richie-Halford A, Bloom D, Grotheer M, Cafarria S, Kiar G, Karipidis II, Roy E, Chandio BQ, Garyfallidis E, Rokem A. Evaluating the Reliability of Human Brain White Matter Tractometry. *Apert Neuro*. 2021;1(1):10.52294/e6198273-b8e3-4b63-babb-6e6b0da10669. doi: 10.52294/e6198273-b8e3-4b63-babb-6e6b0da10669. Epub 2021 Nov 17. PMID: 35079748; PMCID: PMC8785971.
- [128] Cousineau, M., P-M. Jodoin, E. Garyfallidis, M-A. Cote, F.C. Morency, V. Rozanski, M. Grand'Maison, B.J. Bedell, and M. Descoteaux. "A test-retest study on Parkinson's PPMI dataset yields statistically significant white matter fascicles." *NeuroImage: Clinical* 16, 222-233 (2017) doi:10.1016/j.nicl.2017.07.020.
- [129] Kurtzer GM, Sochat V, Bauer MW Singularity: Scientific containers for mobility of compute. *PLoS ONE* 12(5): e0177459 (2017) <https://doi.org/10.1371/journal.pone.0177459>.
- [130] P. Di Tommaso, et al. Nextflow enables reproducible computational workflows. *Nature Biotechnology* 35, 316–319 (2017) <https://doi.org/10.1038/nbt.3820>.
- [131] Garyfallidis E., Côté M.-A., Rheault F., Sidhu J., Hau J., Petit L., Fortin D., Cunanne S., Descoteaux M. Recognition of white matter bundles using local and global streamline-based registration and clustering. *NeuroImage*. 2017.
- [132] Garyfallidis E., Brett M., Correia M.M., Williams G.B., Nimmo-Smith I. Quickbundles, a method for tractography simplification. *Front. Neurosci*. 2012;6:175.

- [133] Song SK, Sun SW, Ramsbottom MJ, Chang C, Russell J, Cross AH. Dysmyelination revealed through MRI as increased radial (but unchanged axial) diffusion of water. *Neuroimage*. 2002 Nov;17(3):1429-36. doi: 10.1006/nimg.2002.1267. PMID: 12414282.
- [134] Song SK, Yoshino J, Le TQ, Lin SJ, Sun SW, Cross AH, Armstrong RC. Demyelination increases radial diffusivity in corpus callosum of mouse brain. *Neuroimage*. 2005 May 15;26(1):132-40. doi: 10.1016/j.neuroimage.2005.01.028. PMID: 15862213.
- [135] Diffusion MRI in multiple sclerosis M. Rovaris, A. Gass, R. Bammer, S. J. Hickman, O. Ciccarelli, D. H. Miller, M. Filippi *Neurology* Nov 2005, 65 (10) 1526-1532; DOI: 10.1212/01.wnl.0000184471.83948.e0.
- [136] Putnam TJ, The centenary of multiple sclerosis. *Arch Neurol Psych*. 1938;40(4):806-813.
- [137] Dunglison R, A dictionary of medical sciences. Philadelphia: Henry C. Lea. 1869.
- [138] Carswell R, Pathological anatomy: Illustrations of the Elementary Forms of the Disease. London: Longman, Orme, Brown, Green and Longman. 1838.
- [139] Cruveilhier J, Anatomie pathologique du corps humain. Paris: JB Baillière. 1829-1842.
- [140] Charcot JM, Histologie de la sclérose en plaques. Paris: Gaz Hôp Civils Milit. 1868;41:554-558.
- [141] Church A, Peterson F, Nervous and mental diseases. London: Rebman Publishing Company Ltd. 1899:50-94.
- [142] McAlpine D, Compston ND, Lumsden CE. Multiple sclerosis. Edinburgh: E&S Livingston. 1955.
- [143] Noseworthy JH, Lucchinetti C, Rodriguez M, Weinshenker BG. Multiple sclerosis. *NEJM*. 2000;343:938-952.
- [144] Paty DW, Ebers GC, Multiple sclerosis. Philadelphie: FA Davis. 1998.
- [145] Compston A, McAlpine's multiple sclerosis. London: Churchill Livingstone. 1998.
- [146] Hayes CE, Cantorna MT, DeLuca HF. Vitamin D and multiple sclerosis. *Proc Soc Exp Biol Med*. 1997 Oct;216(1):21-7. doi: 10.3181/00379727-216-44153a. PMID: 9316607.

- [147] Gogolin KJ, Kolaga VJ, Baker L, Lisak RP, Zmijewski CM, Spielman RS. Subtypes of HLA-DQ and -DR defined by DQB1 and DRB1 RFLPs: allele frequencies in the general population and in insulin-dependent diabetes (IDDM) and multiple sclerosis patients. *Ann Hum Genet.* 1989 Oct;53(4):327-38. doi: 10.1111/j.1469-1809.1989.tb01802.x. PMID: 2576190.
- [148] Simpson CA, Newell DJ, Schapira K. Smoking and multiple sclerosis. *Neurology.* 1966 Oct;16(10):1041-3 passim. doi: 10.1212/wnl.16.10.1041. PMID: 5950585.
- [149] Harbo HF, Gold R, Tintoré M. Sex and gender issues in multiple sclerosis. *Ther Adv Neurol Disord.* 2013 Jul;6(4):237-48. doi: 10.1177/1756285613488434. PMID: 23858327; PMCID: PMC3707353.
- [150] Hauser SL, Goodwin DS. Multiple sclerosis and other demyelinating diseases. In: Fauci AS, Braunwald E, Kasper DL, Hauser SL, editors. *Harrison's Principles of Internal Medicine.* 17th ed. II. New York: McGraw-Hill Medical; 2008. pp. 2611-2621.
- [151] Leemans, Alexander. (2010). Visualization of Diffusion MRI Data. 10.1093/med/9780195369779.003.0021.
- [152]
- [153]
- [154] Cross AH, Song SK. "A new imaging modality to non-invasively assess multiple sclerosis pathology". *J Neuroimmunol.* 2017 Mar 15;304:81-85. doi: 10.1016/j.jneuroim.2016.10.002. Epub 2016 Oct 8. PMID: 27773433; PMCID: PMC5316501.
- [155] Xu J, Sun SW, Naismith RT, Snyder AZ, Cross AH, Song SK. Assessing optic nerve pathology with diffusion MRI: from mouse to human. *NMR Biomed.* 2008 Nov;21(9):928-40. doi: 10.1002/nbm.1307. PMID: 18756587; PMCID: PMC2603138.
- [156] Martin AR, Aleksanderek I, Cohen-Adad J, Tarmohamed Z, Tetreault L, Smith N, Cadotte DW, Crawley A, Ginsberg H, Mikulis DJ, Fehlings MG. Translating state-of-the-art spinal cord MRI techniques to clinical use: A systematic review of clinical studies utilizing DTI, MT, MWF, MRS, and fMRI. *Neuroimage Clin.* 2015 Dec 4;10:192-238. doi: 10.1016/j.nicl.2015.11.019. PMID: 26862478; PMCID: PMC4708075.
- [157] Wang Y, Sun P, Wang Q, Trinkaus K, Schmidt RE, Naismith RT, Cross AH, Song SK. Differentiation and quantification of inflammation, demyelination

- and axon injury or loss in multiple sclerosis. *Brain*. 2015 May;138(Pt 5):1223-38. doi: 10.1093/brain/awv046. Epub 2015 Feb 26. PMID: 25724201; PMCID: PMC4407189.
- [158] Beaulieu C. The basis of anisotropic water diffusion in the nervous system - a technical review. *NMR Biomed*. 2002 Nov-Dec;15(7-8):435-55. doi: 10.1002/nbm.782. PMID: 12489094.
- [159] Paus T. Growth of white matter in the adolescent brain: myelin or axon? *Brain Cogn*. 2010 Feb;72(1):26-35. doi: 10.1016/j.bandc.2009.06.002. Epub 2009 Oct 23. PMID: 19595493.
- [160] Wang Y, Wang Q, Haldar JP, Yeh FC, Xie M, Sun P, Tu TW, Trinkaus K, Klein RS, Cross AH, Song SK. Quantification of increased cellularity during inflammatory demyelination. *Brain*. 2011 Dec;134(Pt 12):3590-601. doi: 10.1093/brain/awr307. PMID: 22171354; PMCID: PMC3235568.
- [161] Yablonskiy DA, Sukstanskii AL. Theoretical models of the diffusion weighted MR signal. *NMR Biomed*. 2010 Aug;23(7):661-81. doi: 10.1002/nbm.1520. PMID: 20886562; PMCID: PMC6429954.
- [162] Pierpaoli C, Barnett A, Pajevic S, Chen R, Penix LR, Virta A, Basser P. Water diffusion changes in Wallerian degeneration and their dependence on white matter architecture. *Neuroimage*. 2001 Jun;13(6 Pt 1):1174-85. doi: 10.1006/nimg.2001.0765. PMID: 11352623.
- [163] Acosta-Cabronero J, Williams GB, Pengas G, Nestor PJ. Absolute diffusivities define the landscape of white matter degeneration in Alzheimer's disease. *Brain*. 2010 Feb;133(Pt 2):529-39. doi: 10.1093/brain/awp257. Epub 2009 Nov 13. PMID: 19914928.